

Controlled Synthesis of Nanostructured Two-dimensional Tin Disulfide and its Applications in Catalysis and Optoelectronics

by

Binod Giri

A dissertation submitted to the faculty of

Worcester Polytechnic Institute

In partial fulfillment of the requirements for the Degree of

DOCTOR OF PHILOSOPHY IN MECHANICAL ENGINEERING

May 2020

APPROVED:

Professor Pratap M. Rao, Advisor
Associate Professor, Mechanical Engineering, WPI

Professor Danielle L. Cote, Committee Member
Assistant Professor, Materials Science and Engineering, WPI

Professor Adam C. Powell, IV, Committee Member
Associate Professor, Materials Science and Engineering, WPI

Professor Lyubov V. Titova, Committee Member
Associate Professor, Physics, WPI

Professor Ronald L. Grimm, Committee Member
Assistant Professor, Chemistry & Biochemistry, WPI

Professor Jamal Yagoobi, Graduate Committee Representative
Department Head, Mechanical Engineering

ABSTRACT

Tin disulfide (SnS_2) is a two-dimensional (2D) material with excellent properties and high prospects for low-cost solutions to catalytic and optoelectronic applications. In this work, vertical nanoflakes of SnS_2 have been synthesized using custom-designed close space sublimation (CSS) system and investigated for applications in photoelectrochemical (PEC) water oxidation and metal-semiconductor-metal (MSM) photodetector. For the PEC application, vertical SnS_2 nanoflakes grown directly on transparent conductive substrates have been used as photoanodes, which produce record photocurrents of 4.5 mA cm^{-2} for oxidation of a sulfite hole scavenger and 2.6 mA cm^{-2} for water oxidation without any hole scavenger, both at $1.23 \text{ V}_{\text{RHE}}$ in neutral electrolyte under simulated AM1.5G sunlight, and stable photocurrents for iodide oxidation in acidic electrolyte. This remarkable performance has been attributed to three main reasons: (1) high intrinsic carrier mobility of $330 \text{ cm}^2 \text{ V}^{-1} \text{ s}^{-1}$ and long photoexcited carrier lifetime of 1.3 ns in the nanoflakes, (2) the nanoflake height that balances the competing requirements of light absorption and charge transport, and (3) the unique stepped morphology of these nanoflakes that improves photocurrent by exposing multiple edge sites in every nanoflake. In another application, these SnS_2 nanoflakes have been used to enhance the performance of lead sulfide quantum dot (PbS QDs) photodetectors by providing a high-mobility channel for photoexcited charges from PbS QDs, which results in 2 orders of magnitude enhancement in responsivity. The physical models and experimental findings presented in this dissertation can help engineer more cost-effective solutions for PEC water splitting and optoelectronics based on 2D metal dichalcogenides.

ACKNOWLEDGEMENTS

It has been both a pleasure and an honor to have had the opportunity to complete my PhD from Worcester Polytechnic Institute. This dissertation would not have been possible without the generous support I have received from faculty and staff as well as my friends and family throughout the last five years.

First and foremost, I would like to thank my dissertation advisor, Prof. Pratap M. Rao for his continuous encouragement and mentorship throughout my PhD. He guided me to be not only a professional in my field but also a better leader. I would also like to thank my Ph.D. dissertation committee members, Professor Ron Grimm, Professor Lyubov Titova, Professor Danielle Cote, Professor Adam Powell and Professor Jamal Yagoobi for taking the time to provide suggestions and recommendations throughout my research.

I would like to extend my gratitude to all individuals who directly contributed to this work with their knowledge, insight, services, and feedback: Maryam Masroor, Tao Yan, Kateryna Kushnir, Dr. Lite Zhou, Dr. Teng Shi, Haochuan Zhang, Jeremy Jacobs, Sunhao Liu, Nicholas Pratt, Barbara Edilberti, Barbara Furhman, Payton Wilkins, Patricia Howe, Dr. Boquan Li, Dr. James Eakin and Dr. Arthur McClelland.

I want to express my sincere thanks to all my colleagues in the Mechanical Engineering Department as well as members of Nanoenergy Lab for their help and engaging discussions. I am also grateful for the support of funding agencies, National Science Foundation and Massachusetts Clean Energy Center.

Finally, I would like to thank my parents and my family members for their constant support and encouragement. Without their care and understanding, I wouldn't have come this far. I am also extremely thankful to my wife Yun for her patience and continuous support over these years.

Table of Contents

List of Figures	vii
List of Tables	xi
Nomenclature	xii
Chapter 1: Introduction	1
1.1. Motivation.....	1
1.2. Hydrogen Opportunity	3
1.3. Low-cost Optoelectronics	4
1.4. Scope and Objectives.....	5
Chapter 2: Background	7
2.1. Two Dimensional (2D) Materials	7
2.1.1. Graphene	7
2.2. Non-graphene Based 2D Metal Dichalcogenides	8
2.2.1. SnS ₂	9
2.3. Catalysis of Water Splitting	11
2.3.1. Electrocatalysis of Water Splitting.....	11
2.3.2. Photoelectrocatalysis/Photoelectrochemistry of Water Splitting.....	12
2.3.3. Figures of Merit	14
2.3.4. 2D Materials in Water Splitting.....	19
2.4. Optoelectronics and Photodetection.....	21
2.4.1. Metal Semiconductor Junctions/Contacts.....	21
2.4.2. Photodetectors.....	23
2.4.3. Figures of Merit	25
2.4.4. 2D Materials in Photodetection.....	28
2.5. Scalable Synthesis of 2D materials.....	29
2.5.1. Need for Scalable Synthesis.....	29
2.5.2. Synthesis of Graphene in Large Quantities.....	29
2.5.3. Synthesis of Metal Dichalcogenides in Large Quantities	30
Chapter 3: Close Space Sublimation of Vertical SnS₂ Nanoflakes.....	31
3.1. Literature Review of Synthesis Methods for SnS ₂	31
3.2. Advantages of Using Close Space Sublimation for SnS ₂	32
3.3. Objectives	33
3.4. Design of the Close Space Sublimation System	33

3.4.1. Heating System	33
3.4.2. Vacuum System	33
3.4.3. Building Materials.....	34
3.4.4. Tunability of Synthesis Parameters.....	34
3.4.5. Scalability of the System.....	34
3.5. Operation Procedure	35
3.5.1. Hydrothermal Synthesis of SnS ₂ Powder.....	36
3.5.2. Removal of Unreacted Sulfur	36
3.5.3. Growth of Vertical SnS ₂ Nanoflakes on Various Substrates	36
3.6. SnS ₂ Nanoflake Growth Mechanism	38
3.7. Conclusions.....	39
Chapter 4: Vertical SnS₂ Nanoflakes for Photoelectrochemical Water Oxidation	40
4.1. Literature Review.....	40
4.1.1. SnS ₂ for PEC Water Oxidation	40
4.1.2. Vertically Aligned SnS ₂ Nanoflakes	41
4.1.3. CSS-grown Vertical SnS ₂ Nanoflakes for PEC Water Oxidation.....	41
4.2. Objectives	42
4.3. Experimental Methods.....	42
4.3.1. SnS ₂ Growth.....	42
4.3.2. Morphology and Composition Characterization.....	44
4.3.3. Optoelectronic Characterization	44
4.3.4. Photoelectrochemical Characterization.....	45
4.4. Results and Discussion	47
4.4.1. Optimization of Synthesis Parameters	47
4.4.2. Measurement of PEC Performance.....	49
4.4.3. Characterization of Structural and Optoelectronic Properties.....	51
4.4.4. Influence of Synthesis Parameters on Nanoflake Characteristics.....	60
4.4.5. Investigation of Photoelectrochemical Stability	61
4.5. Conclusion	66
Chapter 5: Enhancement of PbS Quantum Dot Photodetectors Using High Mobility SnS₂ Nanoflakes	68
5.1. Literature Review.....	68
5.1.1. Lead Sulfide Quantum Dots (PbS QDs) for Photodetection.....	68
5.1.2. SnS ₂ for Photodetection	68
5.1.3. SnS ₂ /PbS QDs Heterostructure for Photodetection.....	69

5.2. Objectives	70
5.3. Experimental Methods	70
5.3.1. Photolithography of Gold Contacts.....	70
5.3.2. Growth of SnS ₂ Nanoflakes	71
5.3.3. Drop Casting of PbS QDs onto SnS ₂ Nanoflakes	72
5.3.4. Optoelectronic Characterization	72
5.4. Results and Discussion	73
5.4.1. SnS ₂ Photodetector.....	73
5.4.2. PbS QDs Photodetector.....	78
5.4.3. SnS ₂ Nanoflakes/PbS QDs Heterostructure Photodetector.....	79
5.4.4. Negative Photoconductivity	83
5.4.5. Photoconductivity Mechanism.....	85
5.4.6. Heterostructure Photodetector with Several Layers of PbS QDs.....	91
5.4.7. Response Time and Frequency Response	95
5.5. Conclusion	97
Chapter 6: Conclusion and Future Recommendations	98
6.1. Summary and Conclusion	98
6.2. Future Recommendations	99
Publications to Date and Planned Publications	102
Publications to Date	102
Manuscripts under Preparation	102
Appendix A	103
Appendix B	107
References	109

List of Figures

Figure 1-1. (a) Concentration of CO ₂ in the atmosphere; and (b) Total global CO ₂ emission from fossil fuels. Source: Global Carbon Project, Global Carbon Budget 2019 ^[1]	1
Figure 1-2. Projection of the generation of renewable electricity by 2050, Source: U.S. Energy Information Administration, Annual Energy Outlook 2020 ^[3]	2
Figure 1-3. SunShot Goals for 2020-2050, Source: US Department of Energy, Solar Energy Technologies Office ^[5]	2
Figure 1-4. Various pathways to produce hydrogen in the near- to long-term future, Source: Department of Energy, Fuel Cell Technologies Office ^[10]	3
Figure 2-1. An overview of the applications of graphene in various sectors ^[20]	7
Figure 2-2. Number of scientific papers published each year on the topic of graphene, MoS ₂ and SnS ₂ , Source: Web of Science.....	9
Figure 2-3. Schematic of the (a) top view and (b) side view of the crystal structures of 2H-SnS ₂ nanosheets.....	10
Figure 2-4. Photoelectrochemical water splitting with tandem photoanode and photocathode (a) with external voltage applied and (b) without any external voltage. (c) Corresponding band diagram of the photoanode and photocathode semiconductors without external voltage ^[55-57]	13
Figure 2-5. Representative Tafel plot with slope equal to Tafel slope and x-intercept equal to log of exchange current density.....	15
Figure 2-6. Band structure of two back-to-back metal/semiconductor junctions. (a) Ohmic contact with no bias; (b) Schottky contact with no bias; (c) Ohmic contact with bias; and (d) Schottky contact with bias	23
Figure 2-7. Device architecture of three main types of photodetectors: p-n photodiodes, photoconductors, and phototransistors.....	24
Figure 2-8. Various applications of photodetectors.....	24
Figure 2-9. Measurement of the rise and fall transit times of a photodetector.....	27
Figure 3-1. Schematic drawing of (a-c) hydrothermal synthesis of SnS ₂ powder followed by (d) the growth of vertical SnS ₂ nanoflakes on FTO using CSS.....	35
Figure 3-2. Picture of the CSS system.....	35
Figure 3-3. SEM images of SnS ₂ nanoflakes grown on various substrates using similar CSS parameters	38
Figure 3-4. Morphology and schematic representation of SnS ₂ nanoflakes grown by the same method on (a) SiO ₂ /Si substrate and (b) FTO substrate.....	39
Figure 4-1. Charge transport in 2 vertical SnS ₂ nanoflakes on the current collector.....	41
Figure 4-2. Schematic of the photoelectrochemical (PEC) measurement setup using SnS ₂ photoanode. All photoelectrochemical measurements were performed in a three-electrode configuration where SnS ₂ nanoflakes on FTO was the working electrode while saturated calomel electrode (SCE) was the reference electrode, and platinum wire was the counter electrode. A magnetic stirrer was used together with nitrogen gas purging to eliminate any mass transfer limitations.....	46
Figure 4-3. Optimization of SnS ₂ nanoflake growth by CSS. (a-c) SEM images of nanoflakes synthesized with T _{sub} = 424 °C, 453 °C and 471 °C; (d-f) SEM images of nanoflakes synthesized with d _{ss} = 19 mm, 15 mm and 10 mm. The insets show respective cross-section views.	48

Figure 4-4. Photocurrents obtained from SnS₂ nanoflake photoanodes at 1.23 V_{RHE} as a function of (a) substrate temperature and (b) growth time and (c) source-substrate distance. Test condition: 1sun illumination, electrolyte containing water, 1M pH7 phosphate buffer and 1M Na₂SO₃..... 49

Figure 4-5. (a) Linear sweep voltammetry of optimized SnS₂ nanoflakes in 0.5 M Na₂SO₄, 1 M phosphate buffer + 1 M Na₂SO₃, and 0.1 M KI + 1 M H₂SO₄ with back illumination; (b) Incident photon-to-current conversion efficiency (also known as external quantum efficiency) of vertical SnS₂ nanoflakes measured with front and back illumination in 0.1 M KI + 1 M H₂SO₄ at 0.6 V_{RHE}. 50

Figure 4-6. Characterization of optimized SnS₂ nanoflakes. (a) High-resolution TEM image of a nanoflake with the corresponding SAED pattern (inset); (b) TEM image of the nanoflake showing partially polycrystalline structure with holes/patches; (c) TEM image of the nanoflake showing stepped structure; (d) XRD of SnS₂ nanoflakes on FTO and (e) Raman spectroscopy of SnS₂ nanoflakes. 52

Figure 4-7. (a) Light Harvesting Efficiency (LHE); (b) indirect bandgap Tauc plot; (c) steady-state photoluminescence spectrum and (d) time-resolved photoluminescence of vertical SnS₂ nanoflakes following photoexcitation with 405 nm, ~20 ps pulses. 53

Figure 4-8. (a) Time-resolved terahertz spectroscopy showing picosecond dynamics of photoconductivity in single crystal SnS₂ and vertical SnS₂ nanoflakes following photoexcitation with 400 nm, ~ 100 fs pulses. Real ($\Delta\sigma_1$) and imaginary ($\Delta\sigma_2$) components of THz photoconductivity of (b) single crystal SnS₂ and (c) vertical SnS₂ nanoflakes on quartz measured at 20 ps after the excitation. The lines in (b-c) represent global fit for real and imaginary components of the conductivity to the Drude-Smith model.... 56

Figure 4-9. Morphological characterization of SnS₂ nanoflakes: (a) SEM image showing steps, (b) AFM image of a broken piece of SnS₂ nanoflake with false color map, (c) corresponding AFM height profile along the dotted line. SEM images of SnS₂ nanoflakes with (d) Cu particles deposited by reduction and (e) PbO_x particles deposited by oxidation, highlighting the edges and steps on the nanoflakes..... 58

Figure 4-10. Chronoamperometric (CA) test with back illumination of vertical SnS₂ nanoflakes in (a) phosphate buffer with and without 1M Na₂SO₃ at 0.6 V_{RHE}, (b) 1M H₂SO₄ at 0.6 V_{RHE}, and (c) 0.5M Na₂SO₄ at 1.23 V_{RHE}. The incident light was blocked for 2 seconds periodically to determine the baseline for the dark current..... 62

Figure 4-11. (a) SEM image of the pristine single crystal SnS₂ electrode prepared by directly bonding CVT-grown SnS₂ to nickel wire using silver glue; (b) SEM image of SnS₂ on ITO obtained by mechanically exfoliating single crystal SnS₂ from the same batch of CVT using thermal release tape (curing temperature 90 °C) and transferring onto ITO; (c) Stability tests (without area correction) of single crystal (blue) and exfoliated (red) SnS₂, performed in phosphate buffer with 1M Na₂SO₃ at 1.23 V_{RHE}. (d) SEM image of the single crystal SnS₂ after mild abrasion, and (e) Comparison of the photocurrents of single crystal SnS₂ before and after abrasion at 0.6 V_{RHE} in 0.1M KI + 1M H₂SO₄ electrolyte..... 63

Figure 4-12. XPS comparison of vertical SnS₂ nanoflakes: (a) as-grown nanoflakes, (b) nanoflakes tested in 1 M H₂SO₄ and (c) nanoflakes tested in 1 M phosphate buffer. The 1st row shows the respective SEM images. The 2nd row corresponds to XPS signal from Sn 3d orbital while the 3rd row corresponds to that from S 2p orbital. 64

Figure 4-13. (a) Chronoamperometric test at 0.6 V_{RHE}; (b) The first and the fifth LSV tests of SnS₂ nanoflakes. Condition: 1 m H₂SO₄ + 0.1 m KI with light chopping and back illumination. 65

Figure 4-14. (a) Stability test of non-optimized SnS₂ nanoflakes for 2 hrs at 0.6 V_{RHE} in 1 m H₂SO₄ + 0.1 m KI with light chopping (total 5 times) and back illumination. SEM images of the nanoflakes (b) before and (c) after the stability test..... 66

Figure 5-1. Photolithography steps used to make Au contacts on SiO ₂ /Si substrates.....	71
Figure 5-2. Close space sublimation setup used to grow SnS ₂ nanoflakes (from Chapter 3).....	72
Figure 5-3. The measurement system used to characterize the performance of SnS ₂ /PbS QDs photodetectors.....	73
Figure 5-4. SEM images of (a) short SnS ₂ nanoflakes grown for 2 min, and (b) tall SnS ₂ nanoflakes grown for 5 min on SiO ₂ /Si substrates.....	74
Figure 5-5. (a) I-V characteristics of SnS ₂ photodetectors and (b) transient photoresponse with pulsed 525 nm LED, 155 μW/cm ² and 5V bias.....	75
Figure 5-6. (a) Transient current measurements of SnS ₂ photodetector under Xenon Lamp (100 mW/cm ²) performed in air followed by vacuum, which is then followed by air again. Bias voltage = 5V. The image in (b) is a photo of the quartz chamber used to test the devices in vacuum.....	76
Figure 5-7. (a) I-V characteristics of the SnS ₂ photodetector and (b) its transient photoresponse with pulsed 780 nm LED, 350 μW/cm ² and 5V bias.....	76
Figure 5-8. Responsivity (a and b) and Photocurrent (c and d) of SnS ₂ photodetectors illuminated with 525nm (a and c) and 780nm LED (b and d).....	77
Figure 5-9. (a) Top and (b) side view SEM images of photodetectors made of 30 layers of PbS QDs on SiO ₂ /Si. The image in (b) shows the region where Au makes contact with the PbS QDs film.....	79
Figure 5-10. SEM images of PbS QDs coated (a) short nanoflakes and (b) tall nanoflakes used to make the photodetector. The insets show the cross-section SEM of the device consisting of.....	80
Figure 5-11. I-V characterization of (a) tall SnS ₂ /PbS QDs heterostructure photodetector and (b) PbS QDs photodetector. The intensity of 525nm and 780nm light were 155 μW/cm ² and 350 μW/cm ² respectively. The wavy pattern of the I-V curve in (b) was due to the inadequate bandwidth of the potentiostat used for the measurement.	80
Figure 5-12. Absolute responsivities of three types of devices with 10 layers of PbS QDs as a function of irradiance levels of (a) 525nm and (b) 780nm light. The chopping frequency was set to 0.1Hz and bias voltage was 5V.....	81
Figure 5-13. External quantum efficiency of three types of devices with 10 layers of PbS QDs as a function of irradiance levels of (a) 525nm and (b) 780nm light. The chopping frequency was set to 0.1Hz and bias voltage=5V.	82
Figure 5-14. Light harvesting efficiency of photodetectors with only 10 layers PbS QDs compared to that of tall SnS ₂ nanoflakes with 10 layers of PbS QDs.....	82
Figure 5-15. Transient current measurement of a photodetector made of tall SnS ₂ with 10 layers of PbS QDs compared to that of a photodetector made of only 10 layers of PbS QDs, illuminated with (a) 525nm LED (155μW/cm ²) and (b) 780nm LED (350μW/cm ²).....	83
Figure 5-16. Transient current response of photodetectors with tall SnS ₂ and 10 layers of PbS QDs obtained under (a) 525nm and (b) 780nm light before and after PMMA encapsulation.....	84
Figure 5-17. Band diagram of SnS ₂ /Au Schottky junction (a) with zero bias and (b) with non-zero bias .	85
Figure 5-18. (a) Schematic of the heterostructure consisting of SnS ₂ nanoflakes and PbS QDs and (b) Band diagram of the p-n junction formed between p-type PbS QDs and n-type SnS ₂ nanoflakes ^[98]	88
Figure 5-19. (a) Photocurrent and (b) responsivity of tall SnS ₂ with 5 layers of PbS QDs at various illumination intensities. The dotted square and diamond symbols represent the photo responses which are plotted in the next figure.	90
Figure 5-20. Transient response of photodetectors made of tall SnS ₂ with 5 layers of PbS QDs at various illumination intensities.....	90
Figure 5-21. (a) Dark current of the short SnS ₂ /PbS QDs photodetector as a function of no. of layers of PbS QDs; (b) Schematic representation of the depletion layer formation at SnS ₂ /PbS interface as more PbS QDs are added.....	91

Figure 5-22. Photocurrent (a) and responsivity (b) obtained from the tall SnS₂/PbS QDs device with varying number of PbS layers; Transient current response of the device (c-f) with just SnS₂ as well as with 10, 20 and 30 layers of PbS QDs, Bias voltage = 5V and λ=780nm. The corresponding Figure B-2 with 525nm is in Appendix B. 93

Figure 5-23. Photocurrent (a) and responsivity (b) obtained from the short SnS₂/PbS QDs device with varying number of PbS layers; Transient current response of the device (c-f) with just SnS₂ as well as with 5, 10 and 30 layers of PbS QDs, Bias voltage = 5V, λ=780nm. The corresponding Figure B-3 with 525nm is in Appendix B. 94

Figure 5-24. Responsivity and response time of the two best SnS₂/PbS heterostructure photodetectors in comparison to other photodetectors based on different 2D materials. The empty space in the top left corner shows the lack of photodetectors with both fast speed and high responsivity. Adapted from ^[103].. 95

Figure 5-25. Transient current response of (a) tall SnS₂ with 30 layers of PbS QDs; (b) short SnS₂ with 30 layers of PbS QDs; and (c) only 30 layers of PbS QDs. (d) Summary of the rise and fall times of the three devices when illuminated with 780nm LED..... 96

Figure 5-26. Frequency response of PbS only and SnS₂/PbS heterostructure devices. (a) tall SnS₂ with 30 layers PbS QDs under 525nm and 780nm illumination; and (b) all three devices under 525nm illumination..... 96

List of Tables

Table 2-1. Examples of 2D materials used for water splitting.....	19
Table 2-2. Ohmic or Schottky contact formed at a metal-semiconductor junction	21
Table 2-3. Examples of 2D materials used in photodetectors ^[97, 101-104]	28
Table 3-1. Several SnS ₂ synthesis methods reported in the literature.....	31
Table 4-1. ICP-OES results showing amount of Sn dissolved in the electrolyte after the test	65
Table 5-1. Responsivity and response time of two representative samples under 780nm illumination, 6.9 μW/cm ² and 5V bias	94

Nomenclature

Symbols and definitions

$\alpha \rightarrow$ Absorption coefficient (units: cm^{-1})

$\phi \rightarrow$ Barrier height (units: J)

$\chi \rightarrow$ Electron Affinity (units: J)

$\nu \rightarrow$ Frequency of the light (units: Hz)

$c \rightarrow$ speed of light in vacuum (units: m/s)

$\lambda \rightarrow$ wavelength of light (units: nm)

$\sigma \rightarrow$ Conductivity (units: Siemens/meter)

$\rho \rightarrow$ Resistivity (units: Ohm-meter)

$\tau \rightarrow$ Lifetime (units: s)

$\mu \rightarrow$ Mobility (units: cm^2/Vs)

$\eta \rightarrow$ Overpotential (units: V)

$\Delta G \rightarrow$ Gibb's free energy (units: J)

$T \rightarrow$ Absolute temperature (units: K)

$e \rightarrow$ Elementary charge constant (units: Coulomb)

$n \rightarrow$ Density of electrons (units: cm^{-3})

$p \rightarrow$ Density of holes (units: cm^{-3})

Subscripts and Superscripts

$T_{sub} \rightarrow$ Substrate temperature

$T_{src} \rightarrow$ Source temperature

$d_{ss} \rightarrow$ Source-substrate separation distance

$J_n \rightarrow$ Electron current

$J_p \rightarrow$ Hole current

$\phi_{Bn} \rightarrow$ Electron barrier height

$\phi_{Bp} \rightarrow$ Hole barrier height

$E^0 \rightarrow$ Equilibrium potential

$j_0 \rightarrow$ Exchange current density

$\eta_{\text{STH}} \rightarrow$ Solar-To-Hydrogen conversion efficiency

$A_n^* \rightarrow$ Effective electron Richard's constant for electrons

$A_p^* \rightarrow$ Effective Richard's constant for holes

$V_{ds} \rightarrow$ External bias between source and drain

$N_c \rightarrow$ Effective density of states at the conduction band

$N_v \rightarrow$ Effective density of states at the valence band

$E_c \rightarrow$ Conduction band energy

$E_v \rightarrow$ Valence band energy

$E_{Fn} \rightarrow$ Quasi Fermi level of electrons

$E_{Fp} \rightarrow$ Quasi Fermi level of holes

$L_D \rightarrow$ Diffusion length

Abbreviations

CVD→ Chemical Vapor Deposition	LSV→ Linear Sweep Voltammetry
CVT→ Chemical Vapor Transport	CA→ Chronoamperometry
PVD→ Physical Vapor Deposition	DFT→ Density Functional Theory
CSS→ Close Space Sublimation	EIS→ Electrochemical Impedance Spectroscopy
LPE→ Liquid Phase Exfoliation	2D→ Two Dimensional
SEM→ Scanning Electron Microscopy	MD→ Metal Dichalcogenides
HR-TEM→High Resolution Transmission Electron Microscopy	TMD→ Transition Metal Dichalcogenides
AFM→ Atomic Force Microscopy	EQE→External Quantum Efficiency
XRD→ X-ray Diffraction	IQE→ Internal Quantum Efficiency
XPS→ X-ray Photoelectron Spectroscopy	IPCE→ Incident Photon-to-current Conversion Efficiency
PL→ Photoluminescence	APCE→ Absorbed Photon to Electron Conversion Efficiency
TRPL→ Time-resolved Photo-Luminescence	ABPE→ Applied Bias Photon-to-current Efficiency
TRTS→ Time-resolved Terahertz Spectroscopy	LHE→ Light Harvesting Efficiency
PPC→ Positive Photoconductivity	SAED→Selected Area Electron Diffraction
NPC→ Negative Photoconductivity	ICP-OES→ Inductively Coupled Plasma - Optical Emission Spectrometry
QDs→ Quantum Dots	NEP→ Noise Equivalent Power
HER→ Hydrogen Evolution Reaction	PEC→Photoelectrochemistry
OER→ Oxygen Evolution Reaction	FTO→ Fluorine-doped Tin Oxide
RHE→ Reversible Hydrogen Electrode	EDT→ Ethanedithiol
SCE→ Saturated Calomel Electrode	
TOF→ Turnover Frequency	
PEC→Photoelectrochemical	

Chapter 1: Introduction

1.1. Motivation

Energy and Environment

Climate change is a threat to the well-being of human beings on the earth. One of the causes of climate change is the excessive use of non-renewable fossil fuels and emission of unsafe levels of carbon dioxide into the atmosphere. According to Figure 1-1, the concentration of CO₂ in the atmosphere has been increasing over the last several decades, and as of 2020, it has reached well above 400 ppm.^[1] At the same time, the global temperatures have increased at least 1.1°C above the pre-industrial average, and keeping this increase to a minimum over the next few decades will be a daunting challenge.^[2]

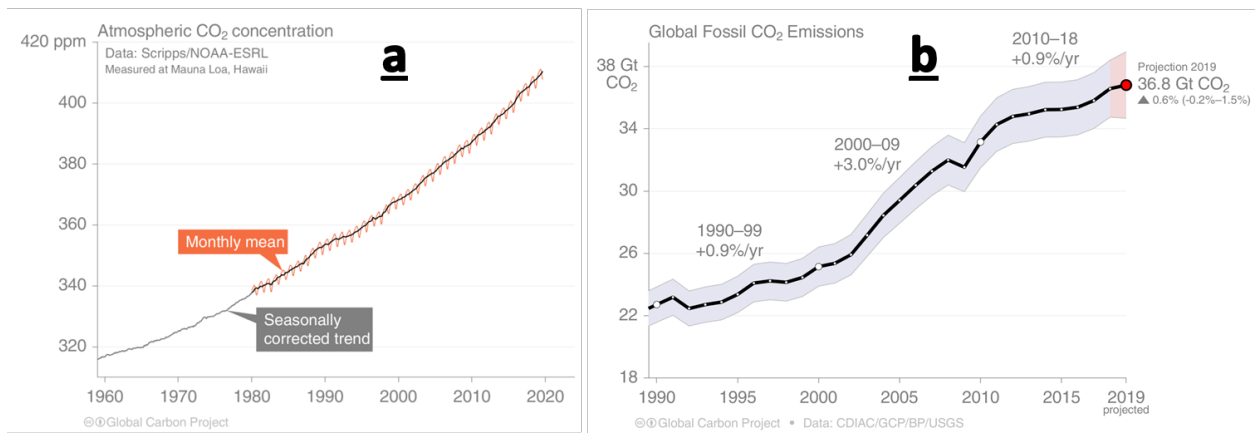


Figure 1-1. (a) Concentration of CO₂ in the atmosphere; and (b) Total global CO₂ emission from fossil fuels. Source: Global Carbon Project, Global Carbon Budget 2019^[1]

In the United States, most of the energy needs are still met using non-renewable fossil fuels. In 2019, renewable energy sources accounted for only about 19% of the total electricity generation (Figure 1-2),^[3] and out of the renewable energy sources, solar only accounted for the 15% however, this is expected to increase to 46% by 2050 (Figure 1-2).

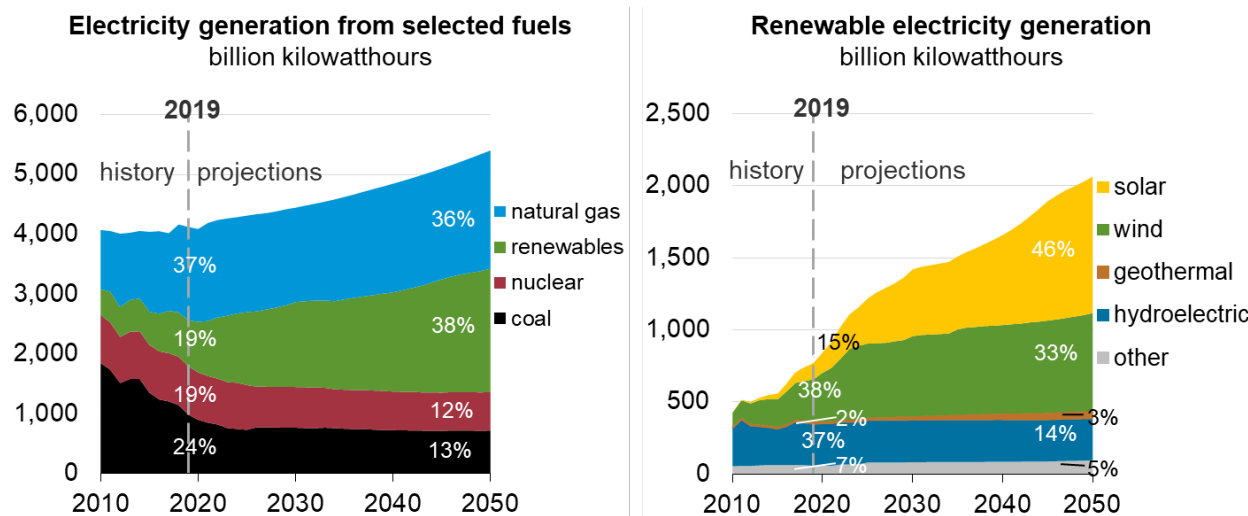


Figure 1-2. Projection of the generation of renewable electricity by 2050, Source: U.S. Energy Information Administration, Annual Energy Outlook 2020^[3]

One of the challenges for the quicker adoption of renewable energy in the US has been the decline in natural gas prices, which suggests that price can be a better motivator than the concern for the environment.^[4] Hence, SunShot, which is one of the US government initiatives that brings together industry and academia, was started with the common goal of making solar energy affordable and reducing carbon emissions.^[5] One important factor in lowering the cost of solar energy and achieving SunShot's 2050 target is the availability of low cost energy storage technologies (Figure 1-3).

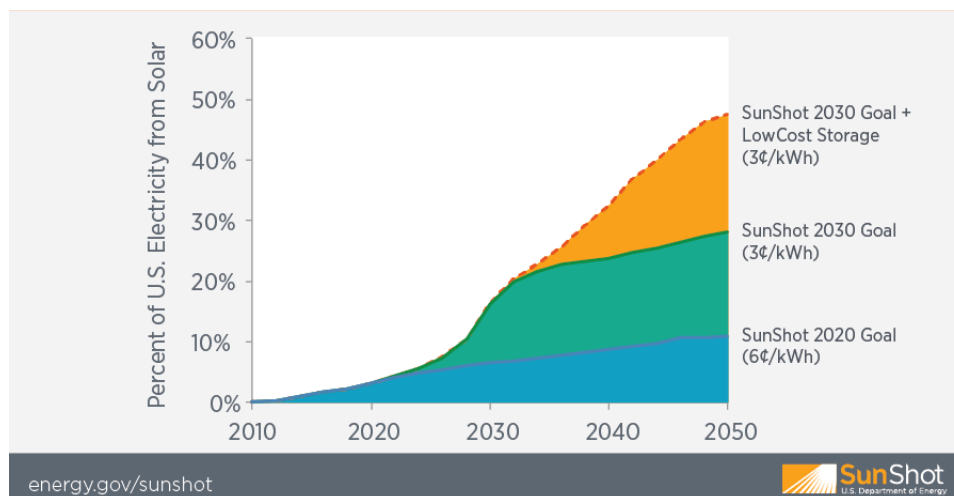


Figure 1-3. SunShot goals for 2020-2050, Source: US Department of Energy, Solar Energy Technologies Office^[5]

1.2. Hydrogen Opportunity

Hydrogen is a clean fuel with high gravimetric energy density (120 MegaJoules/kg) that has the potential to replace non-renewable fossil fuels.^[6] Some experts have even suggested that the entire economy can be based on hydrogen, also called “hydrogen economy”. Currently, the global market size for hydrogen is worth \$135 billion with the compound annual growth rate (CAGR) of 8%, and major consumptions in ammonia production, hydrocracking and removal of sulfur from fossil fuels.^[7-9] However, about 95% of this hydrogen is produced from steam reforming of non-renewable fossil fuels (Figure 1-4).^[10, 11] So, large-scale utilization of hydrogen needs sustainable methods of production, such as water electrolysis using renewable electricity, which could be not only cheap but also environmentally friendly.^[12]

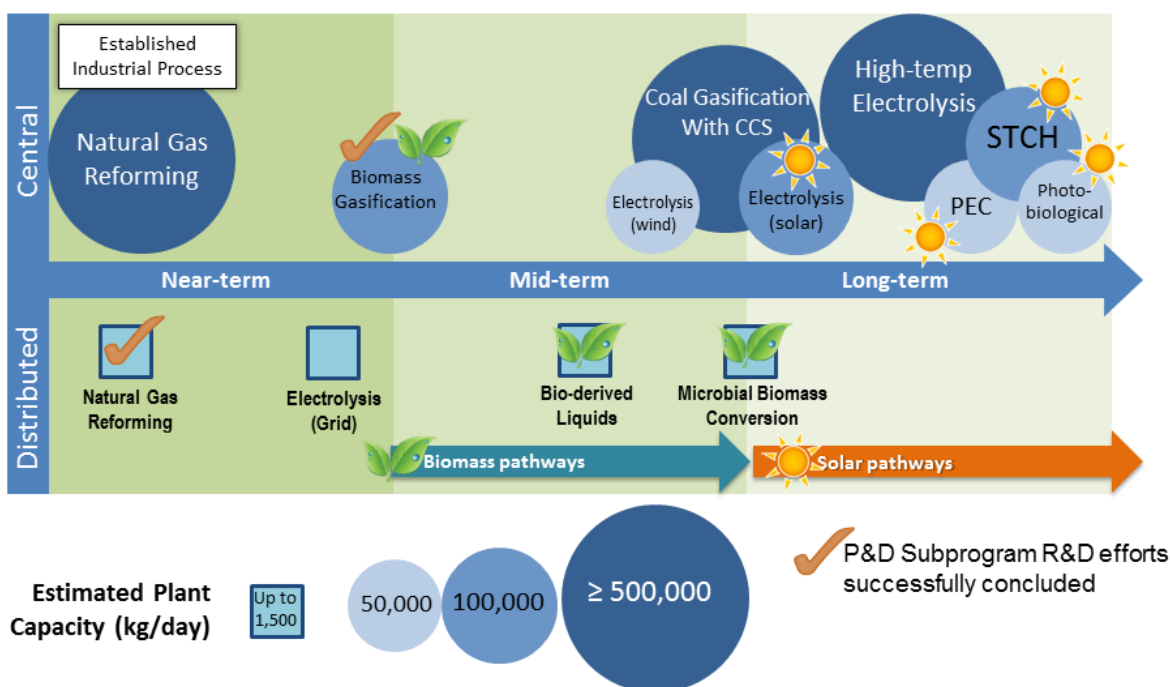


Figure 1-4. Various pathways to produce hydrogen in the near- to long-term future, Source: Department of Energy, Fuel Cell Technologies Office^[10]

Experts agree that the demand and production of hydrogen are only going to increase in the future due to the popularity of fuel cell vehicles. The few fuel cell vehicles that are currently in use get their hydrogen fuel via electrolysis at the refueling stations; however, these electrolytic systems are either inefficient or require the use of very expensive catalysts. This suggests that there is a need for cheaper catalytic materials with the right bulk and interfacial characteristics.

Another method of producing clean hydrogen is by using sunlight, also known as photoelectrochemical (PEC) water splitting. In PEC systems, some or all of the voltage required for water splitting is supplied by sunlight in the presence of a semiconductor with the suitable band gap. Although finding the perfect material for PEC water splitting is a difficult task, this dissertation tries to shed light on scalable synthesis of a relatively novel two-dimensional semiconductor known as tin disulfide (SnS_2), and how nanostructuring can be used to improve its PEC performance.

1.3. Low-cost Optoelectronics

The present optoelectronics sector is dominated by group III–V semiconductors due to their direct band gap and excellent absorption/emission characteristics.^[13, 14] However, these semiconductors are usually derived from rare, toxic and expensive elements. Cheaper and non-toxic alternatives to these materials have been explored but they come with their own set of challenges. 2D materials such as graphene, metal dichalcogenides and MXenes are some of those materials that have had a promising start.

Specifically, 2D metal dichalcogenides with the formula MX_2 where M = metal (eg. Sn, Mo, W) and X = chalcogen (eg. S, Se, Te) have been widely researched due to their low cost and ease of synthesis. Unlike graphene, they possess a large band gap, which is critical in reducing tunneling current as the size of transistors decreases. The best performance has been achieved by using them in monolayer form, which often requires unconventional equipment and synthesis methods. While most of the research community is focused on improving the yield and properties of monolayer metal dichalcogenides, there is a deficiency in research on multilayered 2D nanoflakes, which are still very promising for catalysis and optoelectronics. Hence, this dissertation explores the scalable fabrication of MSM photodiodes made of SnS_2 nanoflakes, and demonstrates that they can improve the performance of the well-known PbS QD photodetectors.

1.4. Scope and Objectives

This dissertation will mainly focus on synthesis and characterization of nanostructured two-dimensional tin disulfide (SnS_2) for PEC water oxidation as well as photodetector applications. The overall objectives of this dissertation are as follows:

1. To design and implement an in-situ close space sublimation (CSS) system for the growth of vertical SnS_2 nanoflakes directly on conductive and non-conductive substrates. Some desired features of the system are independent control of the source and substrate temperatures, ability to vary the gap between source and substrate, in addition to maneuverability of the source and substrate while the system is in vacuum.
2. To understand the influence of experimental parameters on nucleation and growth of layers and edges, stoichiometry, nanostructure morphology and crystallinity of SnS_2 nanoflakes.
3. To measure light absorption, anisotropic charge transport, photoelectrochemical performance and stability of SnS_2 nanoflake photoanodes. In addition, it will be important to determine the location and nature of active sites to fully understand the differences between the SnS_2 nanoflakes synthesized by CSS and those synthesized by other methods.
4. To elucidate the working mechanism of metal-semiconductor-metal (MSM) photodetectors based on vertical SnS_2 nanoflakes grown on non-conductive substrates
5. To develop a physical model to describe the behavior of heterostructure photodetectors made of vertical SnS_2 nanoflakes and lead sulfide quantum dots (PbS QDs). The model will be used to justify why forming a heterostructure is an effective strategy to improve the performance of PbS QDs photodetectors.

A brief description of the preceding chapters of this dissertation is given below:

Chapter 2 introduces key concepts in catalysis, optoelectronics and 2D nanomaterials. It provides essential background information for anyone new to the field before proceeding to the later chapters of the dissertation.

Chapter 3 discusses the design of the close space sublimation system and its various components. The system is then used to tune the growth of vertical SnS₂ nanoflakes for photoelectrochemical water oxidation and photodetector applications.

Chapter 4 goes over the first application of vertical SnS₂ nanoflakes in photoelectrochemical water oxidation. It not only describes the synthesis and characterization of SnS₂ nanoflakes but also explains the origin of the record performance of photoanodes based on these nanoflakes. This chapter is based on the work recently published in *Advanced Energy Materials*.^[15]

Chapter 5 goes over the second application of vertical SnS₂ nanoflakes in heterostructure photodetectors with lead sulfide quantum dots (PbS QDs). It also develops a physical model to explain the positive and negative photoconductivity observed in these photodetectors.

Chapter 6 concludes the dissertation and provides recommendations for continuation of this work in the future.

Chapter 2: Background

2.1. Two Dimensional (2D) Materials

Ever since the “rebirth” of graphene in 2004 for which the two scientists, Andre Geim and Konstantin Novoselov received the Nobel Prize in Physics in 2010, researchers all over the globe have been intrigued with the exceptional mechanical and optoelectronic properties of two-dimensional materials.^[16] Two dimensional materials are a category of materials that have atoms covalently bonded to each other in a layer and each layer is bonded to other layers by weak van der Waals force. Due to this weak bond between the layers, 2D materials can be separated into single layers and still retain most of the material properties.^[17]

2.1.1. Graphene

Graphene is a single layer of sp^2 hybridized carbon atoms arranged in a two-dimensional hexagonal lattice. The unhybridized p_z -electron forms π -bonds, which are responsible for most of the electronic properties of graphene. One of the notable properties of graphene is its Dirac cone, which allows the electrons to move in its lattice as massless particles.^[18] Graphene is of interest to not only the particle physicists interested in studying its anomalous behavior but also engineers interested in utilizing graphene’s properties in devices. Due to exceptional optoelectronic and physical properties, graphene has found applications in many fields including solar cells, sensors, batteries, water purification, gas separation, fuel cells, electronic circuits, and so on (Figure 2-1).^[19, 20]



Figure 2-1. An overview of the applications of graphene in various sectors^[20]

One of the limitations of graphene for electronic applications is the absence of band gap. Several attempts including the growth of graphene ribbons and attachment of oxygen functional groups to graphene have been focused on introducing small band gap at the cost of graphene's other electronic properties.^[21] However, other scientists have gone beyond graphene and focused on other promising two-dimensional materials such as transition metal dichalcogenides (TMDs) and phosphorene.

2.2. Non-graphene Based 2D Metal Dichalcogenides

Although the field of two dimensional materials started with graphene, a family of non-graphene based 2D materials have also been shown to possess outstanding properties relevant for electronics, energy harvesting and energy storage. Some of these transition metal dichalcogenides (TMDs) have even better properties than graphene for some applications. Although the mobility of TMDs ($<1000 \text{ cm}^2\text{V}^{-1}\text{s}^{-1}$) is much lower than that of graphene ($10,000\text{--}15,000 \text{ cm}^2\text{V}^{-1}\text{s}^{-1}$), they possess a band gap that can be tuned by varying the number of layers.^[22] Especially in photodetector applications, much lower steady-state dark current can be obtained with TMDs than with graphene.

TMDs consist of two elements and have a molecular formula of the form MX_2 , where M is a transition metal (i.e. W, Mo, Ta, Nb) and X is a chalcogen (i.e. S, Se, Te). MoS_2 and WS_2 are the most studied TMDs due to their direct band gap and applications in optoelectronics as well as catalysis.

With the popularity of TMDs, other metal chalcogenides were investigated as well. A good example of a two-dimensional metal dichalcogenide that has exciting properties similar to other TMDs is tin disulfide (SnS_2), where Sn is a group 14 metal. SnS_2 has seen applications ranging from electrochemical energy storage, photoelectrochemistry, electrocatalysis, optoelectronics as well as sensors, similar to other TMDs. The rising popularity of SnS_2 follows that of MoS_2 and graphene, which can be seen from the number of articles published over the last decade in Figure 2-2.

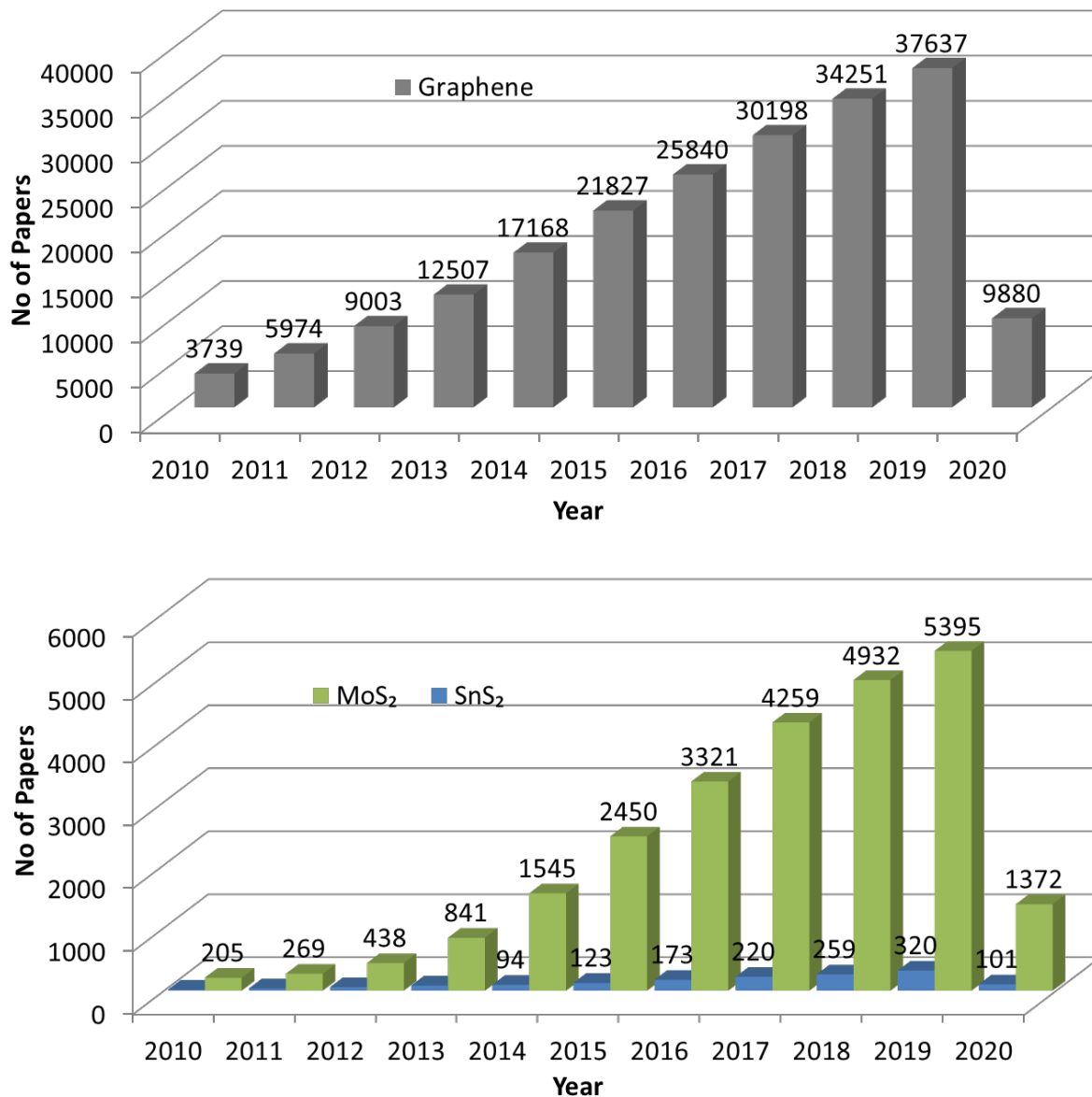


Figure 2-2. Number of scientific papers published each year on the topic of graphene, MoS₂ and SnS₂, Source: Web of Science

2.2.1. SnS₂

Tin disulfide (SnS₂) is a two dimensional (2D) material with CdI₂-type crystal structure, wherein the triatomic layers are held together by weak van der Waals forces.^[23, 24] It is an n-type semiconductor with an indirect bandgap of 2.08-2.44eV,^[25-27] high optical absorption coefficient exceeding 10⁴ cm⁻¹,^[26] and high carrier mobility of 18-760 cm²V⁻¹s⁻¹.^[28-30] In addition, both its elemental constituents have relatively high abundance in the earth's crust.

Due to the lack of direct band gap, SnS₂ is not as popular as MoS₂ for optoelectronic applications and several groups have tried to induce direct band gap in SnS₂ by applying strain or doping.^[31, 32] Nonetheless, due to high mobility and cheaper constituents, SnS₂ has been deemed promising for applications in photoelectrochemical water splitting,^[15, 33] electrochemical sensors,^[34-38] photodetectors,^[34, 39] photovoltaics,^[40-43] electrocatalysis,^[44, 45] and electrochemical energy storage.^[46, 47]

The hexagonal crystal structure of SnS₂ can be subdivided into polytypes, out of which 2H-SnS₂ is the ground state polytype.^[48] In 2H-SnS₂, tin atoms are located in the octahedral sites between two hexagonally close packed sulfur slabs to form a sandwich structure, which makes the basal plane (Figure 2-3). Each basal plane is stacked on top of another along the c-axis, and they are held together by weak van der Waals force. The presence of this weak force means that interlayer separation distance is larger than covalent bond lengths and each layer can be cleaved from the adjacent layer easily without breaking covalent bonds.

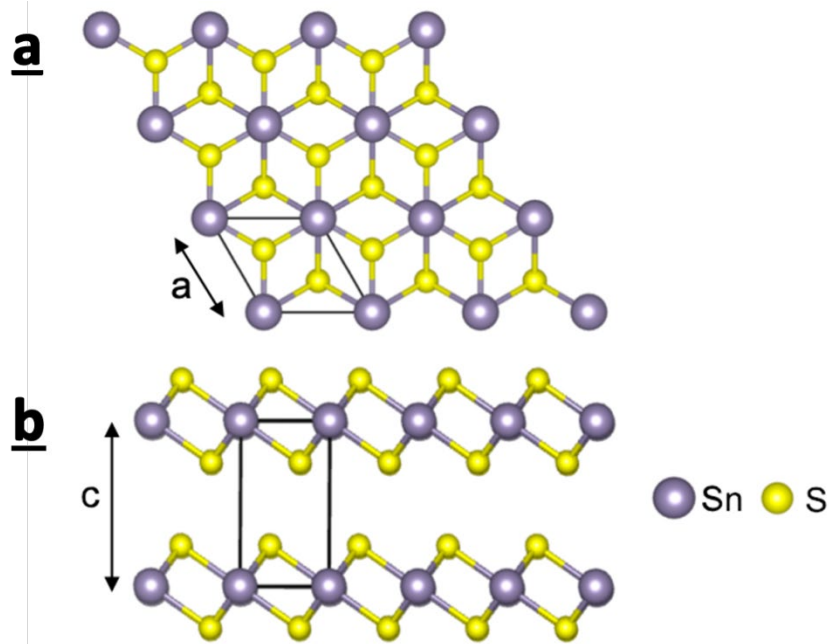


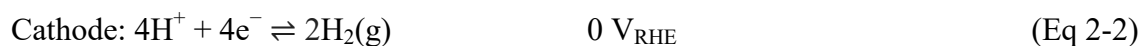
Figure 2-3. Schematic of the (a) top view and (b) side view of the crystal structures of 2H-SnS₂ nanosheets

2.3. Catalysis of Water Splitting

Water splitting is the term used to describe the reaction that converts water molecules to hydrogen and oxygen gas (Equation 2-1). The standard Gibbs free energy of water splitting is $\Delta G^0=237$ KJ/mol at 25°C, which corresponds to the minimum voltage of 1.23V required to perform water splitting.^[12]



This overall reaction can be divided into two half reactions, in which hydrogen is evolved at the cathode and oxygen is evolved at the anode.



However, in practical applications, the required voltage exceeds 2 volts, which makes the industrial application of this technology expensive. Hence, several catalysts are used to lower this additional potential (overpotential) for water splitting. This can be done by two main ways: electrocatalysis and photoelectrocatalysis

2.3.1. Electrocatalysis of Water Splitting

The simplest way to perform water splitting is by applying voltage in water using two electrodes. However, without proper design and optimization, this system would require high voltages, and lower the overall efficiency, raising the cost of hydrogen. One of the ways in which scientists improve the efficiency is by using electrocatalysts that lower the activation energy of the reaction. Since water splitting is a combination of two half reactions taking place at the anode and cathode, separate electrocatalysts are often needed for each reaction. The reaction at the cathode that produces hydrogen is known as hydrogen evolution reaction (HER) while the reaction at the anode that produces oxygen is known as oxygen evolution reaction (OER).

HER Catalysts

Platinum, palladium and iridium are known to be excellent catalysts for hydrogen evolution reaction (HER), however, their cost makes large scale adoption not economically feasible. Several other cheaper alternatives have been identified but their performance falls far below that

of precious metals. Hence, there is an ongoing search for HER catalysts that are not only cheap but also have high catalytic performance.

One of the tools scientists often use to find the right HER catalyst is a volcano plot. It relates exchange current density of a HER catalyst with the Gibb's free energy of hydrogen adsorption (ΔG_{H}^0), which is considered the rate limiting step in the overall hydrogen evolution process. Experts have identified relatively cheap and more abundant 2D materials such as MoS_2 and WS_2 , which are positioned favorably in the volcano plot but they still face many challenges that need to be resolved before they can be widely used.^[49, 50]

OER catalysts

A volcano plot analogous to HER has been used by researchers to guide the search for the best OER catalyst. However, instead of exchange current density and Gibbs free energy of hydrogen adsorption, overpotential is plotted against standard free energy expression $\Delta G_{\text{O}^*} - \Delta G_{\text{OH}^*}$, which is the difference in the binding energy of O^* and OH^* radical intermediates.^[51, 52] Precious metal oxides generally occupy the tip of the volcano in these plots.

Iridium oxide (IrO_x) is one of the best catalysts for oxygen evolution reaction (OER). Although it is not as expensive as platinum, iridium is still one of the expensive metals.^[53] More scalable materials based on alloying nickel, cobalt and iron have also shown promising results.^[52, 54]

2.3.2. Photoelectrocatalysis/Photoelectrochemistry of Water Splitting

Photoelectrocatalysis is a special case of electrocatalysis in which light-induced separation of charges provides additional voltage for the water splitting reaction, further decreasing the external voltage requirement. When a photon is absorbed by a photoelectrode, electrons and holes are separated into two energy levels, where they can help in the water splitting reaction. Since photoelectrocatalysis relies on the interaction of the electrodes with light, photoelectrocatalysts must have a band gap and their valence and conduction bands must be aligned suitably in order to transfer charges to/from the electrolyte (Figure 2-4).

Photoelectrocatalysts are categorized as photoanodes or photocathodes as they can act as an anode or a cathode. Water splitting can be achieved with one or both of the photoelectrodes and depending on the band structure of the materials, external voltage may or may not be needed.

When two or more semiconductors are used, the system is called a tandem photoelectrochemical system.

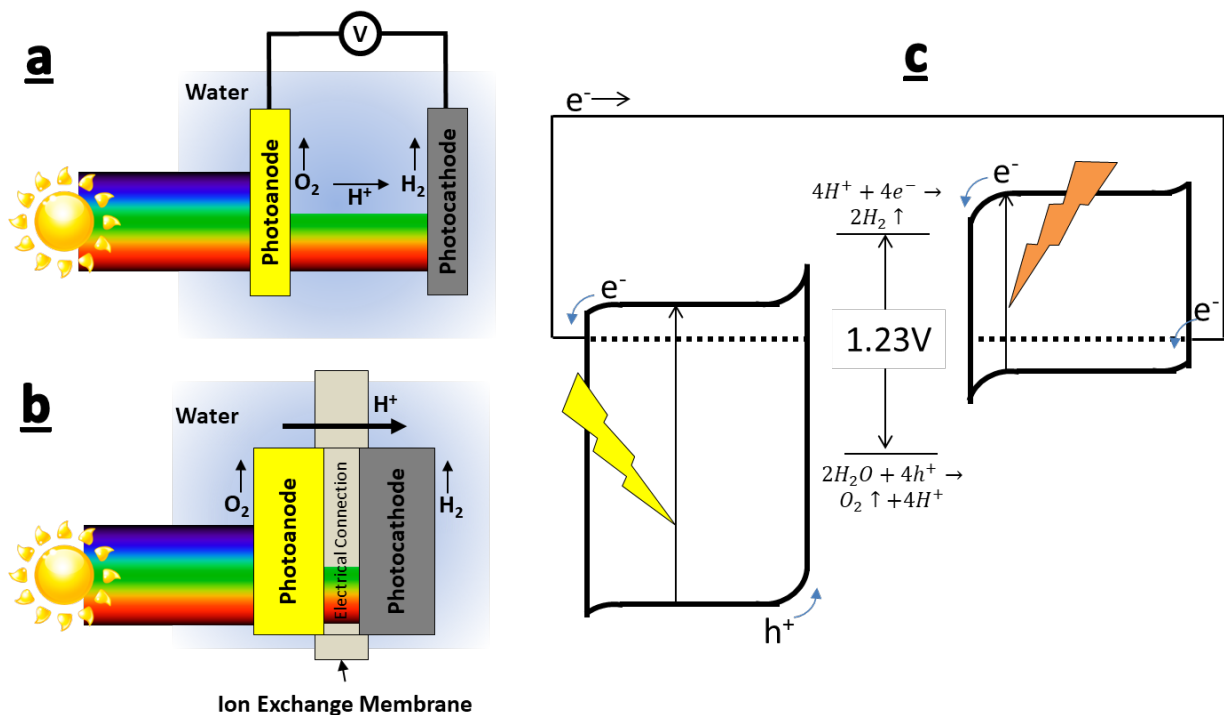


Figure 2-4. Photoelectrochemical water splitting with tandem photoanode and photocathode (a) with external voltage applied and (b) without any external voltage. (c) Corresponding band diagram of the photoanode and photocathode semiconductors without external voltage ^[55-57]

Metal oxide photoanodes such as $BiVO_4$, TiO_2 and Fe_2O_3 coupled with metallic electrocatalyst cathodes have been shown to carry out water splitting at potentials much lower than 1.23 V_{RHE} .^[58] Similarly, photocathodes made of p-Si or Cu_2O coupled with metallic electrocatalyst anodes have also demonstrated ability to reduce water at potentials more positive than 0 V_{RHE} .^[59, 60] Photoelectrocatalysts are not just limited to water splitting but have been used in a number of other solar energy conversion applications such as water decontamination and synthetic fuel production.^[61, 62] Photoelectrocatalysts are slightly different from photocatalysts, which can carry out overall water splitting without the need of any external electricity.

2.3.3. Figures of Merit

In order to assess the catalytic performance of electrocatalysts and photoelectrocatalysts, the following figures of merit are commonly used:

Figures of Merit for HER and OER Electrocatalysts

i. Overpotential (η)

Overpotential is defined as the additional voltage required for the reaction of interest. The thermodynamic potential for hydrogen evolution is 0 V_{RHE}, whereas the thermodynamic potential for oxygen evolution from water is 1.23 V_{RHE}. Hence, overpotential is defined accordingly using the general Equation 2-4 and is related to current density (j) by Butler-Volmer relation in Equation 2-5.

$$\eta = E - E^0 \quad (\text{Eq 2-4})$$

$$j = j_{anodic} + j_{cathodic} = j_0 \left[\exp\left(\frac{\alpha_a nF}{RT} \eta\right) - \exp\left(-\frac{\alpha_c nF}{RT} \eta\right) \right] \quad (\text{Eq 2-5})$$

In order to compare catalysts, parameters such as onset overpotential (η_0), which is the overpotential required for the anodic/cathodic current to start, and η_{10} , which is the overpotential required to obtain photocurrent density of 10 mAcm⁻² are commonly used.

ii. Tafel Slope (b)

The Tafel slope is an indication of the reaction kinetics and is estimated at higher overpotentials. A small Tafel slope implies that only a small additional overpotential is required to increase current density by tenfold. Tafel slope can be determined experimentally from the polarization curve by converting it to a linearized Tafel plot as shown in Figure 2-5.

iii. Exchange current density (j_0)

Similar to Tafel slope, exchange current density is a measure of the catalytic activity of the catalyst. It is referred to the current density at the equilibrium potential. Due to equal and opposite anodic and cathodic currents resulting in no net current through the external circuit, the exchange current density is estimated using the Tafel plot. A high exchange current implies the

presence of more active sites in the electrode and generally is an indication of better performance.

Exchange current density in an electrochemical system can be estimated using the x-intercept of the linear part of the Tafel plot as shown in Figure 2-5.

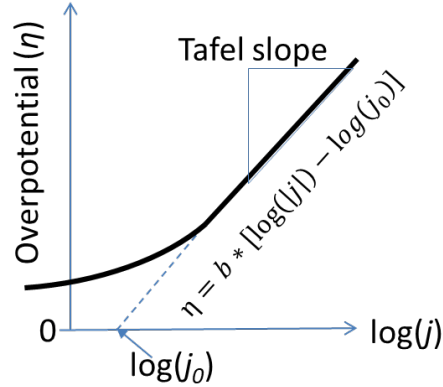


Figure 2-5. Representative Tafel plot with slope equal to Tafel slope and x-intercept equal to log of exchange current density

iv. Catalyst loading (g/cm^2)

The catalyst loading refers to the mass of the catalyst per unit geometric area of the electrode. In order to accurately compare catalysts, it is important to ensure the same catalyst loading.

$$\text{Catalyst Loading} = \frac{\text{Mass of catalyst(g)}}{\text{Geometric Area}(\text{cm}^2)} \quad (\text{Eq 2-6})$$

v. Turnover frequency (TOF)

Turnover frequency is defined as the total number of moles of desired product per active site per second. Its unit is s^{-1} . A larger TOF indicates a more active catalyst. The TOF of a catalyst is determined using Equation 2-7.

$$\text{TOF} (\text{s}^{-1}) = \frac{\text{Turnover Number}}{\text{time of reaction}} = \frac{\text{number of moles of product}}{\text{moles of catalytic active sites} * \text{time of reaction}} \quad (\text{Eq 2-7})$$

For HER catalysts, Equation 2-7 can be further simplified to Equation 2-8 using the parameters that can be measured experimentally.^[63, 64]

$$\text{TOF} (\text{s}^{-1}) = \frac{\# \text{total } \text{H}_2 \text{ turnovers per } \text{cm}^2 \text{ geometric area}}{\# \text{active sites per } \text{cm}^2 \text{ geometric area}} = \frac{J \left(\frac{\text{A}}{\text{cm}^2 \text{ geometric}} \right) * N_A \left(\frac{\#}{\text{mol}} \right)}{2 * F \left(\frac{\text{C}}{\text{mol}} \right) * n \left(\frac{\# \text{ activesites}}{\text{cm}^2 \text{ geometric}} \right)} \quad (\text{Eq 2-8})$$

vi. Stability and lifetime

In order to ensure reliability of water splitting systems, the catalysts in use need to be stable for thousands of hours so they don't have to be replaced too often. Long term stability at various pH values is a very important parameter to consider while designing these catalytic systems.

Figures of Merit for Photoelectrocatalysts

i. Photocurrent density at the thermodynamic potential

Most photoelectrodes are assessed by the photocurrent density they generate at the voltage of interest. For example, thermodynamic potential required to perform water oxidation is 1.23 V vs RHE, hence photoanodes with greater current density at this potential are considered better than the ones with smaller current density. Similarly, for iodide oxidation reaction, photocurrent at 0.53 V vs RHE is more relevant since the onset of iodide oxidation in the dark is at that potential.^[65] Hence, the photocurrent density obtained at this potential is used to identify the better electrode.

ii. Light absorption ($\eta_{absorption}$), charge separation ($\eta_{separation}$) and charge transfer efficiency ($\eta_{transfer}$)

When light is incident on the semiconductor photoelectrode, it is either reflected, transmitted or absorbed. The efficiency at which light is absorbed by the electrode is known as the light absorption efficiency ($\eta_{absorption}$), and it depends on the band gap, thickness as well as the surface texture of the electrode. Similarly, the charge separation efficiency ($\eta_{separation}$) relates to the ability of the semiconductor to transport photoexcited electrons and holes to their respective interfaces for either chemical reaction or transfer to another material. It is influenced by both the intrinsic properties and the presence of any defects/impurities in the semiconductor. Finally, charge transfer efficiency ($\eta_{transfer}$) refers to the efficiency of photoexcited charges being transferred to the electrolyte for the chemical reaction, and depends on the band alignment, surface defect states and the kinetics of the chemical reaction. The product of these three efficiencies determines the overall efficiency of the photoelectrode as shown in Equation 2-9,

$$J_{ph} \left(\frac{mA}{cm^2} \right) = J_{GAP} \left(\frac{mA}{cm^2} \right) * \eta_{absorption} * \eta_{separation} * \eta_{transfer} \quad (\text{Eq 2-9})$$

where J_{ph} is the measured photocurrent and J_{GAP} is the maximum photocurrent if each incident photon with energy greater than the bandgap generates an electron.

iii. External Quantum Efficiency (EQE) or Incident Photon-to-current Conversion Efficiency (IPCE)

EQE/IPCE is a function of the wavelength of light and is given by Equation 2-10.^[66]

$$\begin{aligned} \text{IPCE}(\lambda) = \text{EQE}(\lambda) &= \frac{\text{number of collected electrons per cm}^2 \text{ per second}}{\text{number of incident photons per cm}^2 \text{ per second}} \\ &= \frac{\left| J_{ph} \left(\frac{\text{mA}}{\text{cm}^2} \right) \right| * 1239.8 \text{ (V*nm)}}{P_{\lambda} \left(\frac{\text{mW}}{\text{cm}^2} \right) * \lambda \text{ (nm)}} \end{aligned} \quad (\text{Eq 2-10})$$

It is the measurement of the ability of a photoelectrode to generate current for a given amount of incident light with wavelength λ and intensity P_{λ} .

iv. Internal Quantum Efficiency (IQE) or Absorbed Photon to Electron Conversion Efficiency (APCE)

APCE measures the internal ability of the photoelectrode to convert the absorbed photons into current/electrons. It is given by Equation 2-11.^[66]

$$\begin{aligned} \text{APCE}(\lambda) = \text{IQE}(\lambda) &= \frac{\text{number of collected electrons per cm}^2 \text{ per second}}{\text{number of absorbed photons per cm}^2 \text{ per second}} \\ &= \frac{\text{IPCE}(\lambda)}{A(\lambda)} \\ &= \frac{\left| J_{ph} \left(\frac{\text{mA}}{\text{cm}^2} \right) \right| * 1239.8 \text{ (V*nm)}}{P_{\lambda} \left(\frac{\text{mW}}{\text{cm}^2} \right) * \lambda \text{ (nm)} * A(\lambda)} \end{aligned} \quad (\text{Eq 2-11})$$

Here, $A(\lambda)$ is the percent absorption of the light of wavelength λ .

v. Applied Bias Photon-to-current Efficiency (ABPE)

Since the IPCE and APCE can depend on the applied voltage as well, a more appropriate efficiency in some cases is ABPE that takes into account the externally applied bias voltage. ABPE is defined as:^[55]

$$\text{ABPE} = \frac{J_{ph} * (V_{redox} - V_{bias})}{P_{light}} = \frac{J_{ph} * (1.23 - V_{bias})}{P_{light}} \quad (\text{Eq 2-12})$$

where P_{light} is the total intensity of incident light, J_{ph} is photocurrent density and V_{bias} is the externally applied bias voltage between the working electrode and counter electrode in a two-electrode configuration.

vi. Solar-to-hydrogen conversion efficiency (η_{STH})

The techno-economic analysis by Pinaud et. al. has shown that solar-to-hydrogen conversion (STH) efficiency is the most significant cost driver for water splitting systems.^[57] STH efficiency is defined as the amount of chemical energy produced in the form of hydrogen divided by the solar energy input, with no externally applied bias. It is the benchmark efficiency used to compare materials and systems, and can be determined experimentally by measuring the amount of hydrogen produced.^[12] It is given by Equation 2-13:

$$\eta_{STH} = \frac{\text{Total energy generated per second}}{\text{Total energy input per second}} = \frac{\Delta G \left(\frac{J}{mol} \right) * r_{H_2} \left(\frac{mmol}{s} \right)}{P_{light} \left(\frac{mW}{cm^2} \right) * Area(cm^2)} \quad (\text{Eq 2-13})$$

where, r_{H_2} is the rate of hydrogen produced in moles per second and $\Delta G = 237$ kJ/mol is the change in Gibbs free energy for hydrogen production at 25 °C.

When the rate of hydrogen production is not available, the rate of hydrogen production can be expressed in terms of the product of short circuit current density (J_{sc}) and Faradaic efficiency (η_F) of hydrogen production, and ΔG in terms of voltage, like in Equation 2-14.^[12]

$$\eta_{STH} = \frac{1.23 V * J_{sc} \left(\frac{mA \text{ of } H_2}{cm^2} \right) * \eta_F}{P_{light} \left(\frac{mW}{cm^2} \right)} \quad (\text{Eq 2-14})$$

It should be noted that STH efficiency is calculated with two electrode configuration and short circuit condition. STH calculated with the half-cell using the reference electrode is not a valid device efficiency.^[12] Some examples of STH efficiencies^[12] reported in the literature for water splitting are 10% from triple junction CIGS(Copper Indium Gallium Selenide)^[67] and 18.3% from dual junction AlGaAs/Si based systems.^[68]

2.3.4. 2D Materials in Water Splitting

2D materials are very promising for water splitting due to their remarkable electronic and optical characteristics. Several researchers have already successfully utilized 2D materials such as graphene, metal dichalcogenides (SnS_2 , MoS_2 , WS_2), graphitic carbon nitride ($\text{g-C}_3\text{N}_4$), 2D metal oxyhalides, 2D metal oxides, and layered double hydroxides as electrocatalysts or photoelectrocatalysts to improve the efficiency of water splitting systems.^[69, 70] A summary of some of the 2D materials used in water splitting is provided in Table 2-1.

Table 2-1. Examples of 2D materials used for water splitting

2D Materials	Band Gap	Role in Water Splitting	Ref No
Graphene (Nanocomposite with CdS)	0 eV	Cocatalyst with CdS semiconductor	[71]
N-doped monolayer graphene	0 eV	Electrocatalyst on Silicon photocathode	[72]
Polymeric carbon nitride ($\text{g-C}_3\text{N}_4$)	2.7 eV	Tandem photocathode with CuInS_2 (1.5eV)	[73]
2H- MoS_2 Monolayers	1.9 eV	HER catalyst	[74]
1T- MoS_2 (Nanocomposite with reduced graphene oxide)	0 eV	HER catalyst	[75]
Vertically aligned 2H- WS_2 Nanosheets (with intentionally introduced defects)	0.85 eV	HER catalyst	[76]
Monolayer 1T- WS_2	0 eV	Cocatalyst with TiO_2 semiconductor	[77]
Few layer MoS_2/WS_2	-	Photoanode	[78]
Vertically aligned 2H- SnS_2 Nanosheets	2.18-2.25 eV	Photoanode	[79]
Few layer 2H- SnS_2	2.25 eV	Photoanode	[33]
Ni-Fe Layered Double Hydroxide (LDH)	-	OER catalyst	[80, 81]

Graphene in Water Splitting

Since pure graphene does not have a band gap, it can assist in water splitting by acting as one of the following:^[70]

- **Conducting Platform:** Graphene can act as a conducting platform since its conductivity is higher than many other catalytic materials
- **Host/Support:** Graphene can function as a high surface area host/support for other 2D materials that cannot form a continuous layer on their own
- **Light Harvester:** Graphene can be used to extend the light absorption edge and enhance the light absorption intensity of graphene/semiconductor composites via chemical bonding between semiconductor and graphene.

MoS₂ in Electrocatalytic Water Splitting

Gibbs free energy of adsorbed atomic hydrogen on MoS₂ is very close to zero, suggesting its potential in catalyzing hydrogen evolution reaction. Ever since Jaramillo et.al. showed that the edges of MoS₂ basal planes are catalytically active, there have been several attempts to intentionally create edges and sulfur vacancies in MoS₂ nanoflakes electrochemically or using oxygen plasma in the hopes of maximizing the catalytic activity.^[49, 82, 83] Another study revealed that not only the edges but also the grain boundaries in MoS₂ have a potential to catalyze HER.^[84] Over the last few years, the catalytic activity of MoS₂ has been improved significantly. Some of the best MoS₂ catalysts have Tafel slopes of 39 mV/dec, which approaches the 30 mV/dec of platinum catalysts.^[85]

SnS₂ in Photoelectrochemical Water Splitting

SnS₂ has a band gap of 2.2 eV and a high optical absorption coefficient, which makes it attractive for solar energy applications.^[15, 33, 40, 42, 79, 86] In addition, the conduction and valence bands of SnS₂ straddle oxidation and reduction potentials of water.^[48] However, most practical applications have been able to demonstrate only water oxidation using intrinsic SnS₂, where SnS₂ acts as a photoanode. Another property of SnS₂ important for water oxidation is the high carrier mobility.^[28-30] For water oxidation to benefit the most from the high mobility of SnS₂, the growth direction of SnS₂ nanoflakes need to be controlled, which will be discussed further in the later chapters of this dissertation.

2.4. Optoelectronics and Photodetection

Optoelectronics is an application based on the interaction of light with electronic materials such as semiconductors. It covers a wide range of devices including photodetectors, photomultipliers, phototransistors, light emitting diodes (LED), laser diodes, opto-couplers, optical modulators, charge-coupled devices and other integrated optical circuit elements.^[13] Unlike the majority of electronic devices, which are silicon based, optoelectronic devices are based on group III–V semiconductors such as InP, GaN, GaAs and GaSb, and their alloys.

Price is one of the important drivers of innovation in both electronics and optoelectronics sectors. Silicon is almost universally used in electronics but requires high temperature processing and extreme refining, which makes lowering its cost difficult. In addition, as silicon transistors continue to shrink beyond 10 nm, the effects such as quantum tunneling can lead to high leakage currents and low on-off ratios making it hard to keep up with the “Moore’s law of transistors”.^[87] Similarly, group III-V compounds used in optoelectronics are derived from rare and toxic elements, making it difficult to upscale production.

Fortunately, two-dimensional materials such as graphene and TMDs have shown promise to replace both silicon and group III-V compounds.^[88-93] The atomically thin profile of 2D materials means that many more functional devices can be fit into a small space. Furthermore, the high mobility of 2D materials helps lower heat generation in optoelectronic devices. Single layers of these 2D materials have been either synthesized directly or transferred onto silicon, making it convenient to combine electronics with optics.

2.4.1. Metal Semiconductor Junctions/Contacts

The junction between a semiconductor and a metal can be one of two types: Ohmic or Schottky, which is determined by the work functions (Φ) of the semiconductor and the metal. The specific type of junction formed when the work function of metal is greater or smaller than that of the semiconductor is summarized in Table 2-2.

Table 2-2. Ohmic or Schottky contact formed at a metal-semiconductor junction

	$\Phi_{\text{Metal}} > \Phi_{\text{Semiconductor}}$	$\Phi_{\text{Metal}} < \Phi_{\text{Semiconductor}}$
N-type Semiconductor	Schottky	Ohmic
P-type Semiconductor	Ohmic	Schottky

Both Ohmic and Schottky contacts have been used in the design of optoelectronic devices. For example, photoconductors/photoresistors are generally formed with ohmic contacts. However, Schottky diodes are formed with Schottky contacts.

Types of Currents

In a metal-semiconductor junction, three main types of current flow mechanisms are present, but depending on the exact device architecture, only one of them dominates over the others in practical applications. These mechanisms are as following:^[94]

- Diffusion of carriers from the semiconductor into the metal
- Thermionic emission of carriers across the Schottky barrier
- Quantum-mechanical tunneling through the barrier

In an ohmic junction, the main mechanism for current flow is diffusion of carriers from the semiconductor to the metal, however, in a Schottky junction, thermionic emission usually dominates the overall current. Thermionic emission is based on the theory that only energetic carriers with energy equal to or larger than the conduction band energy at the metal/semiconductor interface contribute to the current. The third type of current flow mechanism, quantum tunneling, is only relevant in highly doped semiconductors with very narrow barrier thickness.

Metal-Semiconductor-Metal Photodiodes (MSM-PD)

Metal-semiconductor-metal photodiodes are made of two back-to-back Schottky junctions, so when a voltage is applied across the two metals, one of the junctions is always forward biased and the other is always reverse biased (Figure 2-6). The presence of this reverse bias helps lower the dark current in these photodiodes. MSM-PDs have been popular in optoelectronics due to the following advantages:^[95, 96]

- Very fast photoresponse
- Compatible with integrated circuit (IC) chips manufacturing
- Low capacitance per unit area
- Low dark current
- Low noise and high sensitivity

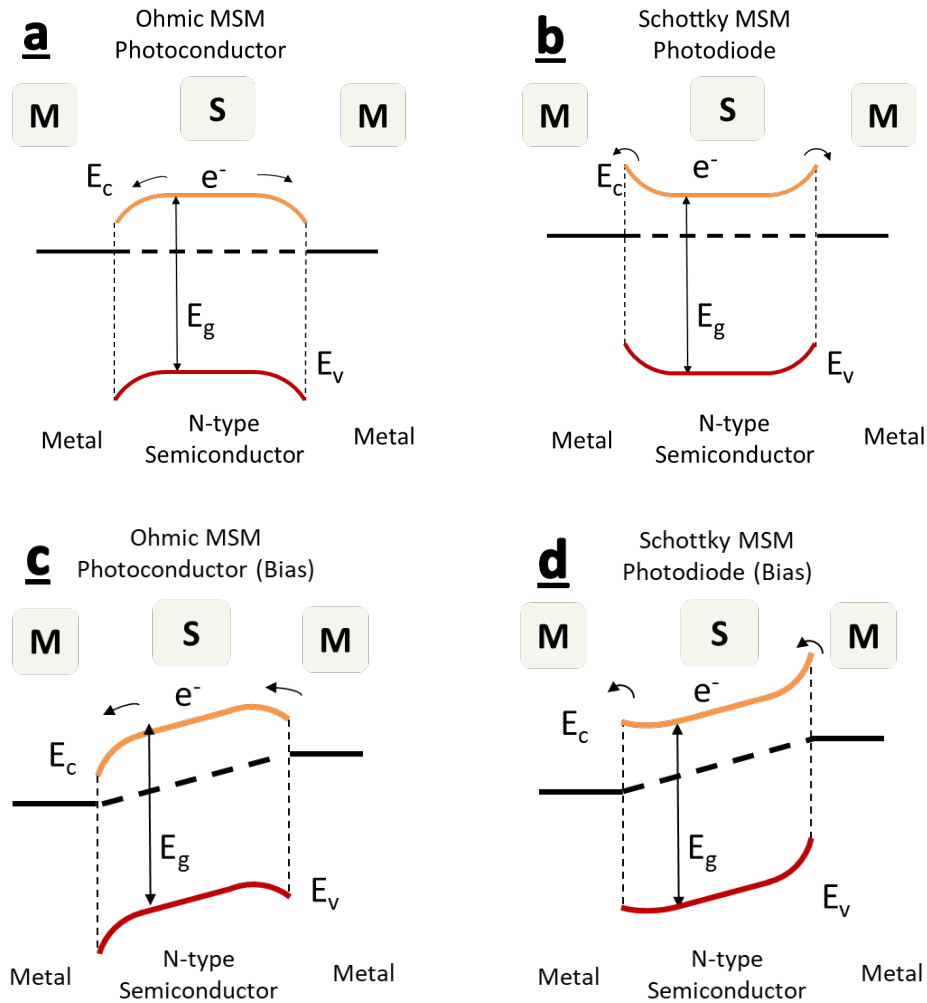


Figure 2-6. Band structure of two back-to-back metal/semiconductor junctions. (a) Ohmic contact with no bias; (b) Schottky contact with no bias; (c) Ohmic contact with bias; and (d) Schottky contact with bias

2.4.2. Photodetectors

Photodetectors can be broadly categorized into three main types based on their device structure: photodiodes, phototransistors and photoconductors/photoresistors (Figure 2-7).^[97] Photodiodes are popular due to their fast response times; however, their fabrication is more complex than that of photoconductors. Photoconductors are attractive due to their simplicity, high responsivity and photogain but they usually have slower response times. Phototransistors have shown promise to combine the better characteristics of both photodiodes and photoconductors. Their responses can also be tuned by using an external gate voltage, which makes them promising for multiple applications.^[97]

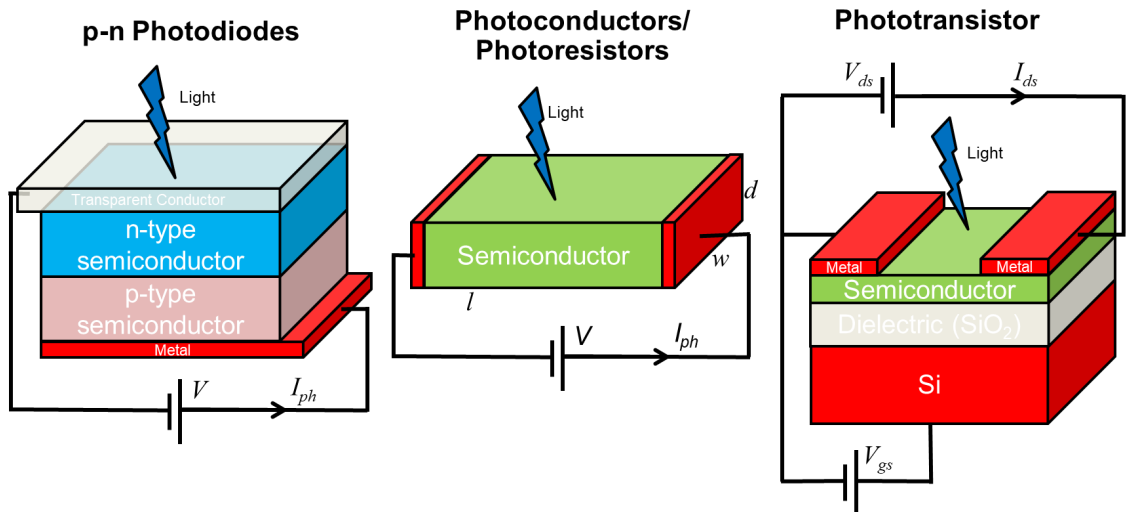


Figure 2-7. Device architecture of three main types of photodetectors: p-n photodiodes, photoconductors, and phototransistors

Photodetectors are used in a broad range of applications due to their versatility. Some of their important applications are highlighted in Figure 2-8.

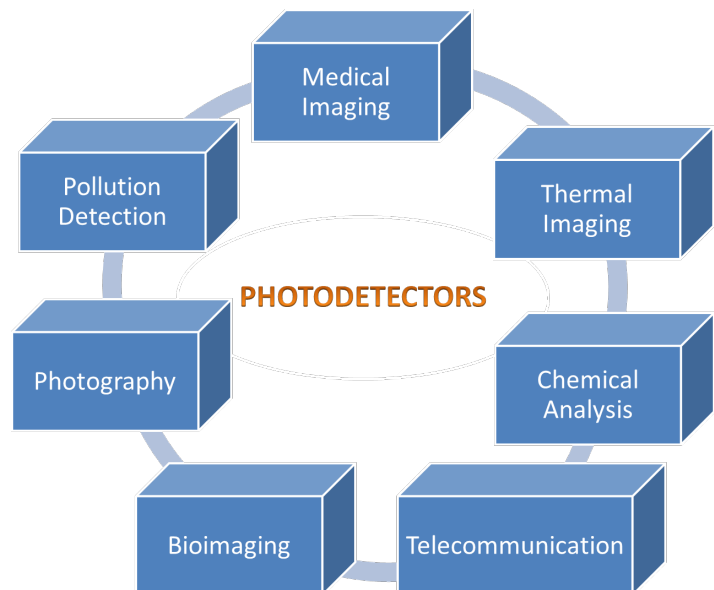


Figure 2-8. Various applications of photodetectors

2.4.3. Figures of Merit

The following figures of merit are used to assess the performance of photodetectors:

i. Spectral Range

A photodetector with a broad range of detection is preferred as it can be used in multiple applications. However, the range of most of the semiconductors is generally limited by their band gap. Heterojunctions consisting of two materials with different band gaps have been shown to widen the spectral range of individual materials.^[98]

ii. Responsivity

Responsivity is defined as:

$$\begin{aligned} \text{Responsivity (A/W)} &= \frac{\text{Photocurrent}}{\text{Incident Power}} = \frac{I_{\text{light}} - I_{\text{dark}}}{P_{\text{in}}} \\ &= \frac{I_{ph}(A)}{P_{in} \left(\frac{W}{m^2} \right) * L(m) * W(m)} \end{aligned} \quad (\text{Eq 2-15})$$

where, L and W are channel length and width respectively and I_{ph} is photocurrent. Responsivity is a measure of the photocurrent generated by a photodetector per unit incident light power. The higher responsivity of a device indicates a better performance.

iii. External Quantum Efficiency

External quantum efficiency is defined as:

$$\begin{aligned} \text{EQE } (\lambda) &= \frac{\text{number of electrons/holes generated per second}}{\text{number of incident photons per second}} \\ &= \frac{|I_{ph}(A)|}{P_{\lambda}(Wm^{-2}) * L(m) * W(m)} * \frac{h * c}{\lambda * e} \end{aligned} \quad (\text{Eq 2-16})$$

Here, h is Planck's constant, c is the speed of light, e is elementary charge and λ is wavelength of the incident light. Unlike in photoelectrocatalysis, EQE in photodetectors can exceed 100% due to the presence of photoconductive gain. In other words, for each slowly drifting minority carrier, several majority carriers can drift quickly through the channel and lead to EQE greater than 100%.

Equation 2-15 and 2-16 can be combined to obtain Equation 2-17 for spectral responsivity (R_{λ}):

$$R_{\lambda} = EQE_{\lambda} * \frac{\lambda * e}{h * c} \quad (\text{Eq 2-17})$$

iv. Photoconductive Gain

Photoconductive gain follows the definition of internal quantum efficiency (IQE) in photodetectors and is given by Equation 2-18, where I_{ph} is photocurrent and P_{abs} is the power of the light absorbed.

$$\text{Gain (G)} = \frac{\text{number of electrons/holes generated per second}}{\text{number of absorbed photons per second}} = \frac{I_{ph}(A)}{P_{abs}(W)} * \frac{h*c}{\lambda*e} \quad (\text{Eq 2-18})$$

This expression can be simplified to Equation 2-19 (derivation in Appendix A), assuming that the photogeneration is uniform throughout the channel, and the majority electrons are primary current-carrying species responsible for photocurrent (i.e. n-type semiconductor device).^[99]

$$\text{Gain (G)} = \frac{\tau_{min}}{L} (\mu_n + \mu_p) E = \frac{\tau_{min}}{t_{maj}} \left(1 + \frac{\mu_p}{\mu_n} \right) \quad (\text{Eq 2-19})$$

where, τ_{min} is minority hole lifetime, t_{maj} is majority carrier transit time along the channel length (L) and depends on the external bias, μ_p is hole mobility and μ_n is electron mobility. The expression $\frac{\tau_{min}}{t_{maj}}$ is sometimes referred to as gain coefficient as it determines the overall trend of the gain.^[100]

v. Noise Equivalent Power, NEP

NEP is an indication of the level of noise in a photodetector. It is defined as the input power required for the signal-to-noise ratio to be equal to 1 at 1 Hz bandwidth.

$$\text{NEP} \left(\frac{W}{\sqrt{\text{Hz}}} \right) = \frac{\text{Input power for SNR=1}}{\sqrt{\text{bandwidth}}} = \frac{P_1}{B^{\frac{1}{2}}} \quad (\text{Eq 2-20})$$

vi. On-off ratio

Defined simply as the ratio of on-current to off-current, on-off ratio represents an important characteristic of photodetectors. The small off current is needed in order to reduce power consumption by the device in the steady state.

$$\text{On-off ratio} = \frac{\text{Light Current}}{\text{Dark Current}} \quad (\text{Eq 2-21})$$

vii. Specific Detectivity

Detectivity is an indication of the sensitivity of the photodetector. Specific detectivity is defined as:

$$D^* \left(\text{Jones or } \frac{\text{cm}\sqrt{\text{Hz}}}{\text{W}} \right) = \frac{\sqrt{A}}{NEP} \quad (\text{Eq 2-22})$$

Here, A is the area of the photodetector in cm^2 .

viii. Response time

Response time for rise and fall of the photocurrent is an important parameter used to compare the performance of photodetectors. It is generally determined by measuring the time interval between the photocurrent reaching 10% and 90% of the maximum (Figure 2-9). A small response time is required for high-speed applications of the photodetector.

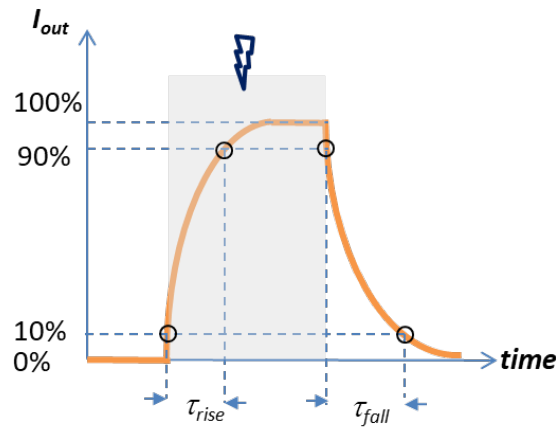


Figure 2-9. Measurement of the rise and fall transit times of a photodetector

2.4.4. 2D Materials in Photodetection

Photodetectors of different device architectures made from 2D materials have been reported in the literature. Table 2-3 gives a glimpse of some of the 2D materials that have recently been used in photodetectors.

Table 2-3. Examples of 2D materials used in photodetectors ^[97, 101-104]

Materials	Photodetector Architecture	Excitation λ	Responsivity (A/W)	Response Time (ms)	Ref. No.
Graphene decorated with PbS QDs	Field effect phototransistor	1200 nm	8×10^3	100	[105]
MoS₂ decorated with PbS QDs	Field effect phototransistor	635 nm	6×10^5	350	[106]
WS₂ decorated with PbS QDs	Field effect phototransistor	808 nm	14	0.153	[107]
SnS₂ decorated with PbS QDs	Field effect phototransistor	970 nm	10^6	160	[98]
WSe₂/SnS₂	p-n photodiode	550 nm	11.5	250	[108]
Graphene-MoTe₂-Graphene	Vertical Field Effect Transistor	1064 nm	0.11	0.046	[109]
Monolayer MoS₂	Phototransistor	561 nm	8.8×10^2	600	[110]
Few Layer SnS₂	MSM Photodiode	457 nm	0.009	0.05	[34]
Vertical MoS₂ nanoflakes	MSM Photodiode	635 nm	0.006	100	[111]

Some of the best photodetector performances in the literature were obtained by mechanical exfoliation of 2D materials, a method which suffers from low yield and high cost. A better strategy for some applications will be to use 2D nanoflakes without exfoliation, which can be more scalable and decrease the cost significantly while still providing moderate performance.

2.5. Scalable Synthesis of 2D materials

2.5.1. Need for Scalable Synthesis

Large scale application of any new technology always requires a low-cost and steady supply of raw materials as well as a reliable method of synthesis. Platinum is a well-known and reliable electrocatalyst for water splitting but its high cost has hindered its widespread use.^[74, 112] Similarly, Fe_2O_3 is a relatively cheap photoanode material but the systems based on Fe_2O_3 are not very robust for long-term use.^[113] Scientists and engineers around the globe have to consider these factors while perfecting the water splitting technology.

One benefit of using graphene or metal dichalcogenides is that their constituent elements are relatively more abundant on the earth. However, without scalable synthesis methods, catalytic or optoelectronic systems based on these materials can be costly. Therefore, it is important for scientists and engineers to consider the long-term goal of scalability in their research efforts.

2.5.2. Synthesis of Graphene in Large Quantities

Graphene, like any other 2D nanomaterial, can be synthesized using either top-down or bottom-up approach. Top-down approach refers to separation/exfoliation of individual graphene sheets from its bulk form graphite whereas bottom-up refers to the assembly of individual carbon atoms to form a continuous graphene layer. Both top-down and bottom-up approaches can be scalable.

Separation of graphite into graphene has been achieved by several methods such as solid phase mechanical exfoliation, liquid phase exfoliation and electrochemical exfoliation.^[19] The famous scotch tape method that was used to produce graphene by mechanical exfoliation for the first time is still used today.^[16] However, this method generally has low yield and cannot be scaled up. Liquid phase exfoliation is a more scalable alternative; however, it suffers from unwanted functionalization and instability.

Another important measure of scalability of graphene is its lateral size. Meter-sized single crystal graphene sheets have recently been synthesized using chemical vapor deposition on industrial copper substrates.^[114] Using a similar bottom-up approach known as epitaxial growth, researchers were able to grow bi-layer graphene of size $75\ \mu\text{m} \times 75\ \mu\text{m}$ on C-face 6H-SiC substrates.^[115]

2.5.3. Synthesis of Metal Dichalcogenides in Large Quantities

The scalable synthesis of metal dichalcogenides is an ongoing field of research. Several methods to synthesize them in either bulk or monolayer form have been reported. Bulk flakes of MoS₂, SnS₂ and WS₂ consisting of hundreds of layers can be synthesized using methods such as hydrothermal reaction, and chemical bath deposition (CBD). For millimeter to centimeter size crystals, chemical vapor transport (CVT) and physical vapor transport (PVT) are used.^[48, 116]

Majority of applications of these 2D materials use the monolayer form, which can be produced by top-down or bottom-up approaches, similar to graphene. Liquid phase exfoliation (LPE) is generally considered the most scalable top-down approach as large quantities of monolayers can be produced in a single batch.^[117, 118] This is suitable for catalytic applications, where the amount of material used is larger in comparison to that in optoelectronic applications. In contrast to mechanical exfoliation or plasma assisted exfoliation, the nanoflakes yielded by LPE are relatively small (few hundreds of nanometers).^[117] Wafer-size metal dichalcogenides have also been synthesized mostly using bottom up methods such as chemical vapor deposition (CVD), molecular beam epitaxy (MBE) and atomic layer deposition (ALD).^[119-122] However, they still have issues such as poor crystallinity, the need to transfer to a clean substrate and losses in performance due to grain boundaries.^[123]

Chapter 3: Close Space Sublimation of Vertical SnS₂ Nanoflakes

3.1. Literature Review of Synthesis Methods for SnS₂

Three main phases of tin and sulfur, namely SnS, Sn₂S₃ and SnS₂ have been synthesized by various methods. SnS is a p-type semiconductor with band gap of 1.1eV while SnS₂ is an n-type semiconductor with band gap around 2.2eV.^[124] Sn₂S₃ with band gap around 1.1eV has also been synthesized by a few groups and is an n-type material.^[124-127] Out of these three phases, SnS is mostly popular in photovoltaics, and SnS₂ is mostly popular in catalysis and optoelectronics.

Various methods of synthesizing SnS₂ have been reported in the literature, and the most suitable method may depend on the intended application. Table 3-1 shows some of the common synthesis methods of SnS₂ reported in the literature.

Table 3-1. Several SnS₂ synthesis methods reported in the literature

Synthesis Method	Form of SnS ₂	Application	Ref. No.
Chemical Vapor Deposition	thin crystals	photodetector	[34]
Chemical Vapor Transport	mm size single crystals	measurement of electronic and optical properties	[48]
Hydrothermal Method	randomly oriented nanoflakes	NH ₃ gas sensing	[128]
Mechanical Exfoliation	monolayer/few layers	photodetector	[98]
Liquid Phase Exfoliation	monolayer/few layers	photoanode	[33]
Spray Pyrolysis	nanoparticle thin film	nanobiosensor	[129]
Close Space Sublimation	vertical nanoflakes	measurement of structural and electrical properties	[130]

Large Single Crystals

SnS₂ is sometimes synthesized in the form of millimeter to centimeter size single crystals to study its bulk properties. The most common method to synthesize such crystals is chemical vapor transport (CVT) and physical vapor transport (PVT). Large crystals are also useful in applications where exfoliation is used to form monolayers.

Nanostructures (Nanoflakes, Nanoparticles, Nanorods)

For most engineering applications, SnS₂ is synthesized in the form of nanostructures. Synthesis methods such as chemical vapor deposition, spray pyrolysis, hydrothermal synthesis, exfoliation and close space sublimation have been used to obtain these nanostructures. Regardless of the synthesis method, SnS₂ nanostructures generally need to exhibit high purity and crystallinity for photoelectrochemical and optoelectronic applications.

3.2. Advantages of Using Close Space Sublimation for SnS₂

Close space sublimation (CSS) is one of the promising scalable ways to synthesize thin films. It is already used commercially to synthesize Zn and Cd chalcogenide solar cells.^[131-136] A few research groups have recognized the benefits of using CSS to grow SnS₂ nanoflakes.^[27, 130] One of the important properties of SnS₂ that makes it feasible to use CSS synthesis is its ability to sublime at temperatures below its melting point (600 °C).^[137, 138] The advantages of using CSS in the synthesis of vertical SnS₂ nanoflakes are discussed below:

- **Scalability:** CSS can be a suitable method for synthesis of large quantities of SnS₂ nanoflakes for catalytic and optoelectronic applications.
- **High Purity:** Impurities can adversely affect the performance of the devices based on SnS₂, but by using CSS, the amount of impurities can be minimized.
- **Grain Size Control:** The size of grains/flakes of SnS₂ can easily be controlled by tuning the source and substrate temperatures during synthesis

Despite the obvious advantages of using CSS in SnS₂ synthesis, the number of researchers that implemented this method successfully is small.^[27, 130] One of the reasons for this could be the high cost of commercial close space sublimation systems. Since SnS₂ is generally considered a cheaper alternative to more exotic semiconductors, using an expensive synthesis method can increase the overall cost. Therefore, in this project, a low-cost CSS system was designed and customized to synthesize SnS₂ nanoflakes.

3.3. Objectives

The main objectives of this project are as following:

- To design a functioning CSS system that can be used to synthesize vertical SnS₂ nanoflakes but at a fraction of the cost of commercial systems
- To maintain reliability of the system and consistency of the growth of SnS₂ nanoflakes
- To allow tunability of synthesis parameters so that users can obtain SnS₂ nanoflakes with the right set of properties
- To ensure that the system meets the following requirements for SnS₂ synthesis:
 - Source temperatures of 300 to 600 °C
 - Substrate temperatures in the range of 300-500 °C
 - Vacuum pressure lower than 50 mtorr
 - Substrate sizes of at least 2cm by 2cm

3.4. Design of the Close Space Sublimation System

3.4.1. Heating System

Several types of heat sources were considered for the CSS system, such as electrical resistance heater, infrared heater and a flat flame burner. However, the flat flame burner already set up in the laboratory for the synthesis of metal oxide nanowires was chosen in order to avoid additional cost of a new heat source. One of the advantages of the flat flame burner system is uniform heating, which allows homogeneous growth of SnS₂ throughout the substrate. It can also easily achieve temperatures up to 1000 °C relatively quickly, leading to shorter preheating times.

3.4.2. Vacuum System

One of the important decisions in building CSS system was the choice of a vacuum pump. Commercial CSS systems use very low pressures to ensure that the final product is not contaminated; however, it was observed that even with moderate vacuum, very fine quality SnS₂ nanoflakes could be obtained if proper attention was paid to handling precursors and flushing the system with inert gas prior to use. Hence, a ~\$2500 pump that can reach a vacuum level of 1 millitorr was used instead of more powerful and more expensive vacuum pumps that reach few orders lower.

3.4.3. Building Materials

The CSS chamber was built using a quartz tube because quartz can easily withstand high temperatures and low pressures of the CSS system. The quartz tube had two open ends, which allowed easy insertion and removal of source and substrate material into the chamber. During operation, the two ends, which were at least 6 inches away from the flame and stayed relatively cool, were capped using high temperature silicone stoppers. These soft caps also allowed the vacuum and coolant tubes to be fitted without the need of expensive feedthroughs.

Similarly, the substrate holder was constructed out of stainless steel as it is not easily corroded. The source boat was also made out of stainless steel and no evidence of cross contamination from stainless steel was observed in the SnS₂ nanoflakes.

3.4.4. Tunability of Synthesis Parameters

One of the objectives of this project was to allow users to tune the synthesis parameters as needed, hence, the CSS system was designed accordingly. The source temperature could be tuned by controlling the flow rate of fuel (CH₄) and air through the flat flame burner. Similarly, substrate temperature could be tuned by changing the flow rate and temperature of the coolant (water) running through the substrate holder. The distance between the source and substrate was varied by changing the number of metal spacers between the substrate and the substrate holder. Finally, growth duration could be controlled by deciding when to turn off the flame and push the source boat out of the hot zone.

3.4.5. Scalability of the System

The scalability issue was considered in choosing every components of the final CSS system. Although the final system was only able to make samples of size 2cm by 2.5cm and met the requirements for research purposes, larger volume production can be envisioned with slightly modified components. First of all, the flat flame burner can be easily scaled up by changing the size of the burner and having multiple burners running simultaneously in a row. Similarly, the substrate size can be increased in proportion to the size of the flame.

The source powder, which is synthesized by hydrothermal method, can be scaled up easily using larger reactors. At the end of the growth, the SnS₂ source powder changes to SnS phase, which can easily be collected and re-sulfurized for the next growth, reducing the waste.

3.5. Operation Procedure

The overall process of synthesizing vertical SnS_2 nanoflakes on various substrates is presented in Figure 3-1. A photograph of the system is shown in Figure 3-2.

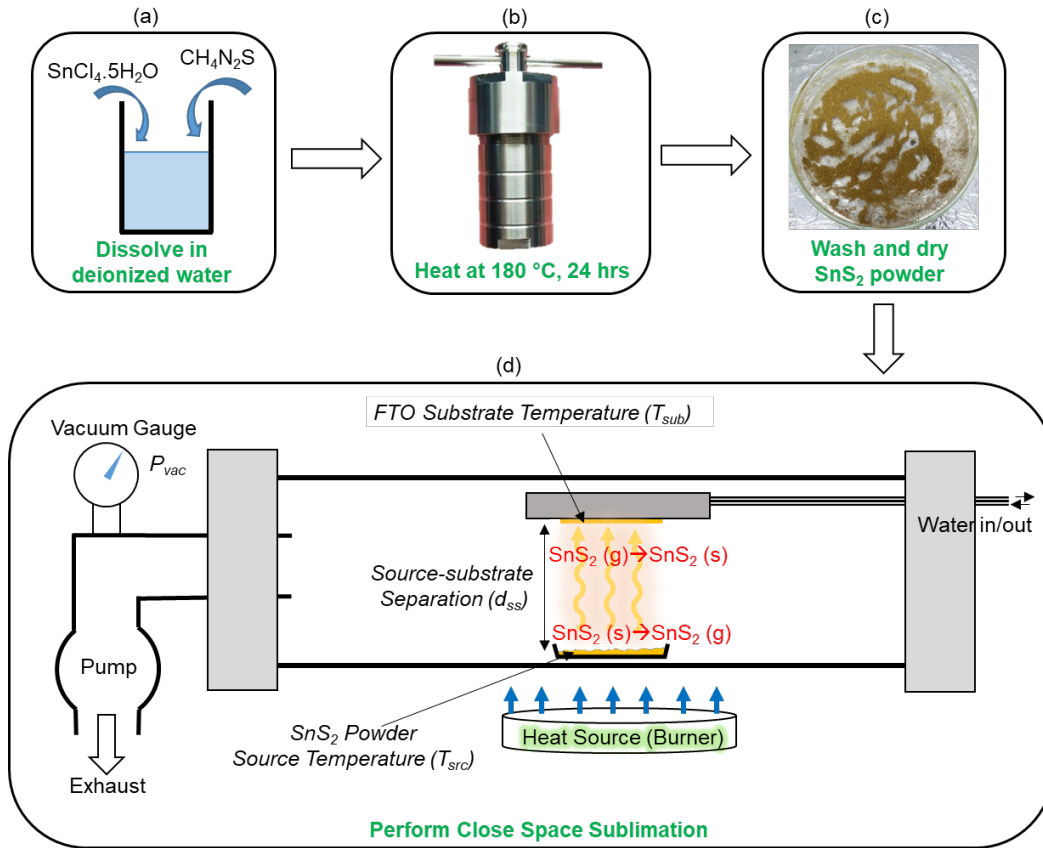


Figure 3-1. Schematic drawing of (a-c) hydrothermal synthesis of SnS_2 powder followed by (d) the growth of vertical SnS_2 nanoflakes on FTO using CSS

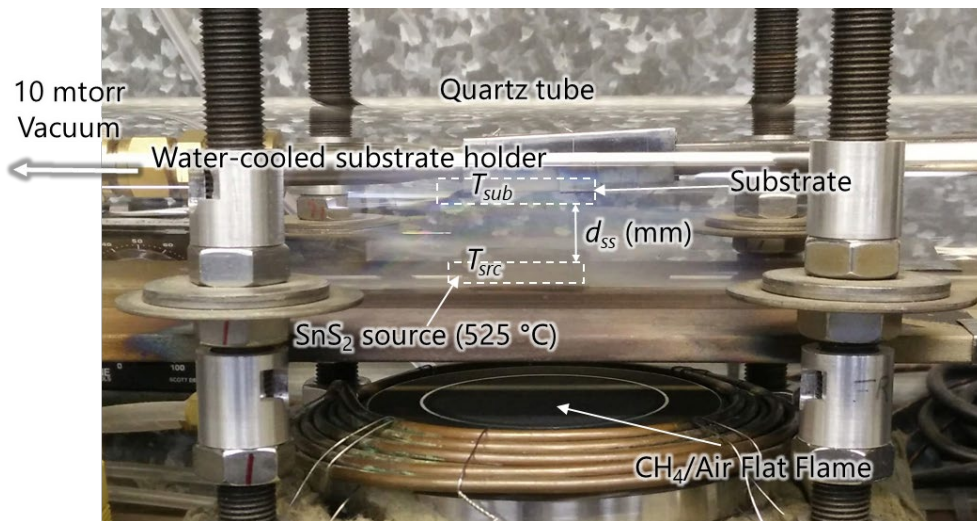


Figure 3-2. Picture of the CSS system

3.5.1. Hydrothermal Synthesis of SnS₂ Powder

SnS₂ powder to be used as an evaporation source for close space sublimation was synthesized by modifying a method reported elsewhere.^[139] At first, 0.3M thiourea (Sigma Aldrich, >99%) and 0.1M tin (IV) chloride pentahydrate (Sigma Aldrich, >98%) were dissolved in 40 mL deionized (DI) water and stirred vigorously for 30 min. The excess sulfur precursor was to ensure complete sulfurization of SnS₂. Then, the solution was poured into a Teflon-lined steel autoclave and heated at 180 °C for 24 hours. Afterwards, the SnS₂ precipitate was collected, and rinsed with ethanol and deionized (DI) water several times.

3.5.2. Removal of Unreacted Sulfur

The precipitate from the hydrothermal reaction consisted of SnS₂ powder and unreacted sulfur. At first, the precipitate was dried on hot plate at 50 °C to get rid of water. Then it was further dried in vacuum for 8 hours at either 80°C or 200°C to get rid of any remaining moisture as well as unreacted sulfur that may be trapped inside powder particles.

Drying the SnS₂ powder at only 80°C left unreacted sulfur inside the powder particles, which led to unpredictable scattering of powder particles. Therefore, for all the SnS₂ nanoflake growths discussed in this dissertation, the powder was instead dried at 200°C for 8 hours in vacuum. It should be noted that SnS₂ was not affected by heating at 200 °C in vacuum.

Another interesting observation was that the nanoflakes grown on quartz substrates were denser when the source powder was dried at 80°C rather than at 200°C. This could be the result of excess sulfur vapor helping the nucleation of SnS₂ crystals on quartz surface at lower temperatures.

3.5.3. Growth of Vertical SnS₂ Nanoflakes on Various Substrates

Before using the CSS system to grow vertical SnS₂ nanoflakes, the substrates were cleaned by sonicating in 1:1:1 mixture of deionized water, isopropanol and acetone followed by drying with compressed air. Then the CSS setup was wiped clean with the help of acetone and clean paper so that there were no residues from the previous batch. A substrate of choice was mounted onto the substrate holder using thin stainless steel wires at two points. Finally, the source boat containing SnS₂ powder was placed inside the quartz tube and the ends were closed off using silicone stoppers.

When the vacuum level reached 10mtorr, the fuel and air were flown in to the burner and ignited with a lighter to produce a stoichiometric flame. This marked the beginning of preheating, where the entire setup was heated until the substrate reached a desired temperature. Meanwhile, the source boat was placed away from the flame to not cause sublimation during preheating. After the growth time had elapsed, the growth was stopped by turning off the heat source and pushing the source boat off to a side. When the system had naturally cooled to room temperature, the sample was taken out.

The following substrates were used to grow SnS₂ nanoflakes and the optimum synthesis parameters were slightly different for each substrate depending on their surface roughness.

- Glass/fluorine doped tin oxide (FTO)
- Glass/Indium tin oxide (ITO)
- Glass/FTO/TiO₂
- Carbon foil
- Stainless steel foil
- Mica
- Quartz slide
- SiO₂/Si

Any substrate that does not react with sulfur and can withstand temperatures up to 450°C can be used as substrates. Figure 3-3 shows SEM images of SnS₂ nanoflakes grown on Glass/ITO, carbon foil, stainless steel foil and mica substrates. The growths on Glass/FTO and SiO₂/Si are discussed in the next section.

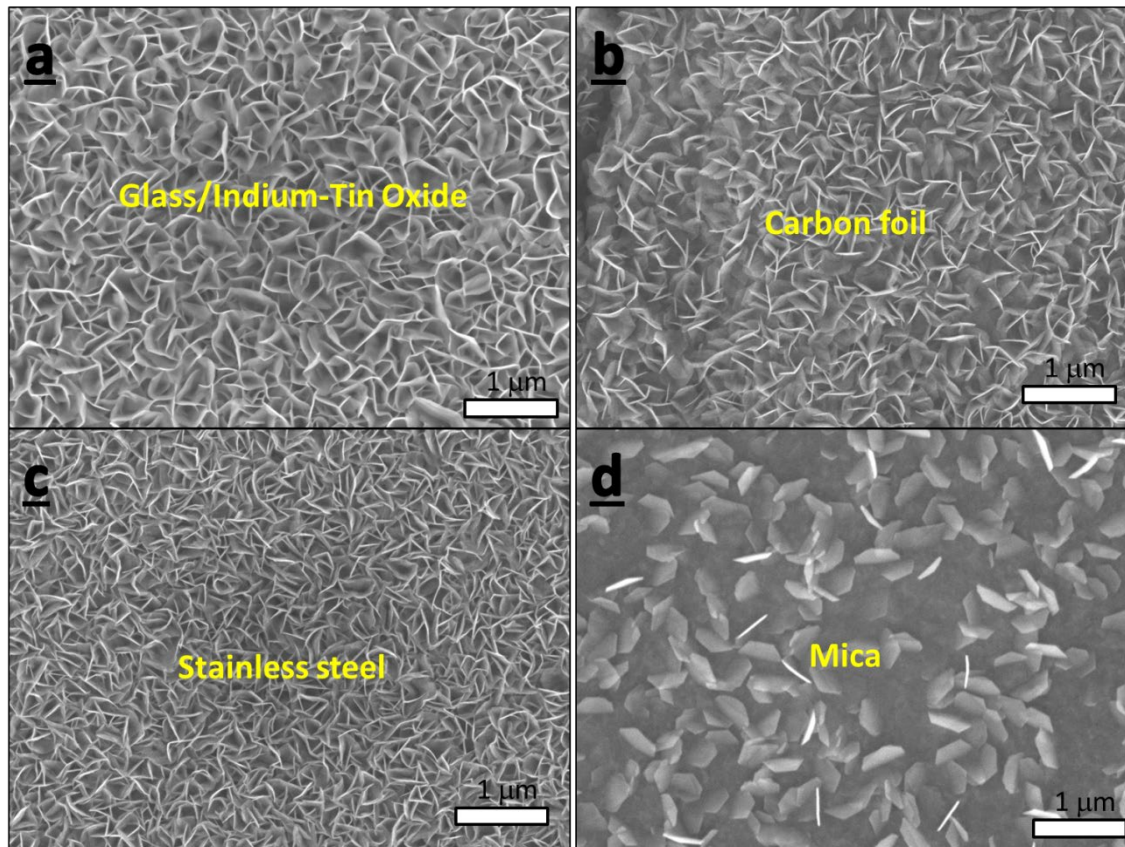


Figure 3-3. SEM images of SnS₂ nanoflakes grown on various substrates using similar CSS parameters

3.6. SnS₂ Nanoflake Growth Mechanism

SnS₂, being a 2D material, has a higher tendency to continue growth along a basal plane than nucleate new basal planes.^[140] This results in anisotropic crystal growth in the form of nanoflakes. However, the alignment/orientation of the nanoflakes is influenced by the roughness of the substrate, as observed in our experiments (Figure 3-4) and reported in the literature for other 2D materials.^[141] On the relatively flat SiO₂/Si surface, SnS₂ first nucleates islands which then grow horizontally until they interact with other islands. During this interaction, the basal planes get pushed upwards, which results in the vertical orientation of the nanoflakes. The evidence of this phenomenon can also be observed in the cross-section SEM images of SnS₂ growth on SiO₂/Si substrates in Figure 3-4a (inset). In the case of FTO substrate with relatively rough surface, the SnS₂ basal planes either grow purely vertically or first grow conformal to the facets of FTO grains followed by vertical growth, as shown in Figure Figure 3-4b. In both of these scenarios, the basal planes can form direct connection to FTO for efficient charge transfer.

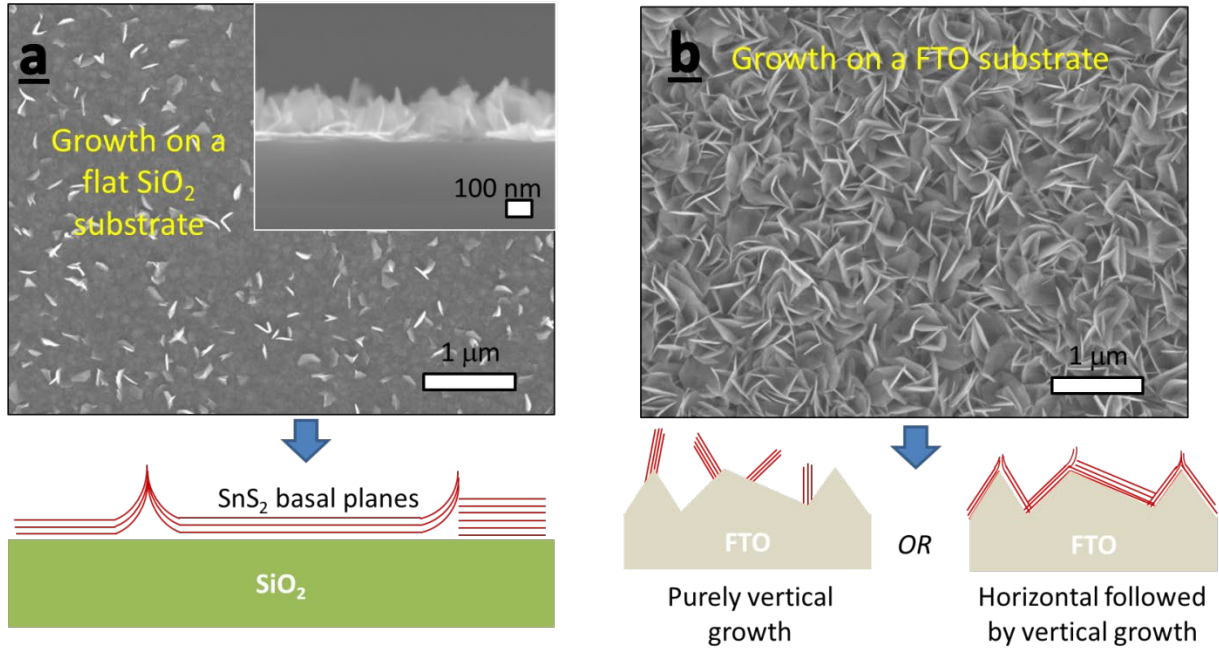


Figure 3-4. Morphology and schematic representation of SnS₂ nanoflakes grown by the same method on (a) SiO₂/Si substrate and (b) FTO substrate

The SnS₂ nanoflake growth mechanism is important in understanding the origin of photoconductive properties of SnS₂ thin films grown on SiO₂/Si substrates. If each of the individual nanoflakes were grown entirely vertically from the substrate without interaction with other nanoflakes, the SnS₂ thin film on SiO₂ would not behave as a continuous channel.

3.7. Conclusions

In this project, a close space sublimation system was designed and built in order to facilitate the growth of SnS₂ nanoflakes. Various system components were chosen to meet the requirements of SnS₂ growth while also keeping the cost low. The CSS system is reliable and can be used to grow SnS₂ nanoflakes with the desired morphology on various substrates. SnS₂ nanoflakes grown on FTO and SiO₂/Si substrates were used in photoanodes and MSM photodetectors respectively, which will be discussed in the later chapters. Furthermore, the CSS system developed here also inspired other CSS systems that were used to synthesize BiI₃ and CuI, with compressed air as a coolant and electrical heat wrap as heat source.

Chapter 4: Vertical SnS₂ Nanoflakes for Photoelectrochemical Water Oxidation

4.1. Literature Review

4.1.1. SnS₂ for PEC Water Oxidation

SnS₂ has been synthesized and studied by several researchers because of its potential suitability for applications in electrochemical sensors,^[34-38] photodetectors,^[34, 39] photovoltaics,^[40-43] electrocatalysis,^[44, 45] and electrochemical energy storage.^[46, 47] It is a two dimensional (2D) material with CdI₂-type crystal structure, wherein the triatomic layers are held together by weak van der Waals forces.^[23, 24] It is an n-type semiconductor with an indirect bandgap of 2.08-2.44eV,^[25-27] high optical absorption coefficient exceeding 10⁴ cm⁻¹,^[26] and high carrier mobility of 18-760 cm²V⁻¹s⁻¹.^[28-30] In addition, both its elemental constituents have relatively high abundance in the earth's crust.

One of the promising applications of SnS₂ is in the field of photoelectrochemical water splitting. The energies of the conduction and valence bands of single crystal SnS₂ straddle the oxidation and reduction potentials of water, making SnS₂ promising for water splitting.^[48] The band gap of SnS₂ is similar to that of cadmium sulfide, which it could replace in single or tandem photoanodes or photovoltaics.^[124] A few groups have already demonstrated the potential of SnS₂ photoanodes in photoelectrochemical (PEC) water oxidation.^[33, 79, 86, 142]

Several methods of synthesizing vertically oriented SnS₂ nanoflakes on conductive substrates have been reported in the literature such as hydrothermal reaction,^[43] chemical vapor deposition (CVD),^[79, 143] and close space sublimation (CSS).^[27, 130] However, only few of these methods have been used to optimize the nanoflakes for photoelectrochemical applications. In one case,^[79] vertical SnS₂ nanoflakes were synthesized on a fluorine doped tin oxide (FTO) current collector using CVD, and a photocurrent of ~1.5 mAcm⁻² was obtained at the thermodynamic potential for water oxidation (1.23 V_{RHE}) in 0.5 M Na₂SO₄. In spite of having strong light absorption, these SnS₂ nanoflakes yielded photocurrents much lower than the theoretically possible ~11 mAcm⁻² for 2.2 eV band gap material.^[144] In order to further understand and improve the performance of SnS₂ photoanodes, vertical SnS₂ nanoflakes were synthesized on FTO using CSS, and the dependence of photocurrent on composition and morphology was studied.

4.1.2. Vertically Aligned SnS₂ Nanoflakes

The PEC application of SnS₂ can benefit immensely from the ability to control its nanostructure during synthesis. In particular, when the basal planes of SnS₂ are perpendicular to the current collector, photoexcited charges can be transported more efficiently because conductivity along the SnS₂ basal planes is $\sim 10^4$ times that across them.^[23] In other words, any photogenerated electrons or holes in the nanoflakes can quickly move to either the current collector or the SnS₂-electrolyte interface without requiring to hop between the neighboring basal planes. One method of achieving perpendicular orientation is by growing SnS₂ in the form of vertical nanoflakes on the current collector (Figure 4-1).

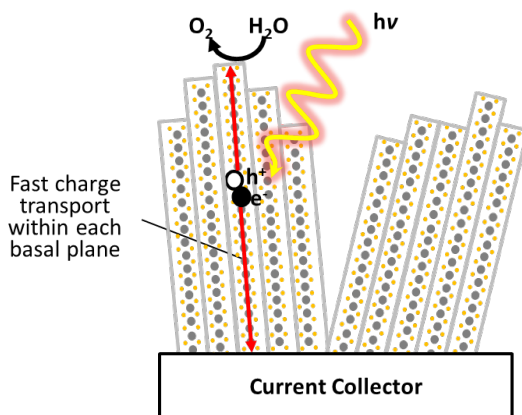


Figure 4-1. Charge transport in 2 vertical SnS₂ nanoflakes on the current collector

In addition to the vertical orientation, the height of SnS₂ nanoflakes needs to be optimized so that the competing requirements of light absorption and diffusion of photoexcited charges are balanced.

4.1.3. CSS-grown Vertical SnS₂ Nanoflakes for PEC Water Oxidation

Close space sublimation is often used in the semiconductor industry to produce high quality thin films of zinc and cadmium chalcogenides for solar cells.^[131-133] It is popular due to its ability to grow large crystals without impurities. In most cases, post annealing of the thin films is not necessary and deposition of multiple layers simultaneously or sequentially is possible. CSS was used to synthesize SnS₂ thin films by researchers demonstrating that it is possible to grow vertically aligned SnS₂ nanoflakes.^[130] However these films were not optimized for PEC application, suggesting the need for this current study.

4.2. Objectives

The specific objectives of this project were as following:

- To grow vertical SnS₂ nanoflakes directly on FTO substrates using the custom-built CSS system
- To tune the experimental parameters to minimize phase impurities and maximize photocurrent from SnS₂ nanoflake photoanodes
- To understand the origin of high photocurrent in SnS₂ photoanodes by probing their morphological, optoelectronic and electrochemical characteristics
- To investigate the long-term stability of SnS₂ photoanodes

4.3. Experimental Methods

4.3.1. SnS₂ Growth

Growth of SnS₂ Nanoflakes on Glass/FTO by CSS

First, fluorine-doped tin oxide (FTO) glass (Hartford Glass, IN) substrates of typical size 2cmx2.5cm were sonicated and cleaned 3 times in a 1:1:1 mixture of isopropanol, acetone, and deionized water. Then they were dried with compressed air, and used to grow SnS₂ nanoflakes by CSS.

A custom-built CSS system developed in Chapter 3 was used to grow vertical SnS₂ nanoflakes directly on FTO-coated glass substrates. The system consisted of a 2-inch diameter quartz tube that enclosed a stainless steel (SS) fixture for holding the FTO substrate, and a custom-made stainless steel source boat (LxWxH: 25mmx7mmx5mm) containing SnS₂ powder. A rotary vane pump (KJLC-RV206) was used to pump down the tube. A 60-mm diameter co-flow premixed laminar flat-flame porous-plug burner equipped with a co-flow shroud (manufactured by Holthuis and Associates, Sebastopol, CA) was used to provide heat externally. The source temperature was controlled by the CH₄-to-air ratio (typical flow rates: 3.5 lpm CH₄ and 35 lpm air) in the flat flame burner while the substrate temperature was controlled by the flow rate of water (typical flow rate: 0.5 lpm) through the substrate holder. Source and substrate temperatures were measured using K-type thermocouples that were in contact with the source and substrate,

respectively, and the total pressure in the quartz tube was monitored by a convection enhanced Pirani gauge.

In a typical growth, a clean FTO substrate was mounted onto the underside of the water-cooled substrate holder using stainless steel wires such that it was directly above the flat flame. The source boat containing 0.1 g SnS₂ powder was placed off to one side of the substrate and the tube was pumped down to about 10 mtorr. Then, the burner was started in order to preheat the system. To ensure that the substrate had the same temperature throughout the growth process, the source boat was pushed under the substrate only after the substrate temperature had stabilized. This was marked as the beginning of growth. When the desired growth time had elapsed, the flat flame was extinguished and the system was allowed to cool naturally to room temperature while maintaining vacuum. The quartz tube was then vented and the sample was removed.

Synthesis of single crystal SnS₂

Chemical vapor transport (CVT) yielded the single-crystal SnS₂ material. Quartz tubes (19 mm O.D., 17 mm I.D., G.M. Associates, Oakland, California) were sealed at one end. Cleaning included a one-week submersion in a 10 w/v % aqueous KOH solution, rinsing in 18 MΩ water, and oven drying at >100 °C. Loading under an air ambient included 1.3 g tin (99.999% purity, 1-3 mm pieces, Strem, Newburyport, Massachusetts, used as received), 0.75 g sulfur (≥99.5%, Sigma-Aldrich, used as received), and 0.20 g iodine (99.999% trace metal basis, Sigma-Aldrich, used as received). The iodine mass was chosen to yield an approximately 4 mg cm⁻³ charge for a 23-cm-long tube that, in concert with the temperature values below, yield the 18R polymorph with minimal contributions from other polytypes.^[145] Connection to a diffusion-pump-equipped Schlenk line with a base pressure below 1 x 10⁻³ torr afforded tube evacuation. Prior to evacuation, the tube contents were cooled in a water ice bath for 5 minutes to minimize the loss of iodine vapor during evacuation, followed by expeditious sealing under vacuum. Heating in a two-zone tube furnace utilized rapid heating to 800 °C at the newly sealed deposition side, and 2 °C min⁻¹ heating to 700 °C in the "source" zone. Following a six-hour period of 700 °C in the source zone and 800 °C in the deposition zone, the temperature in the deposition zone decreased directly to and remained at 575 °C for 240 hours whilst the source zone remained at 700 °C. Following this growth period, two successive cooling steps included one six-hour step of decreasing the temperature in the source zone at 2 °C min⁻¹ to 300 °C while raising the

temperature in the deposition zone at $2\text{ }^{\circ}\text{C min}^{-1}$ to $600\text{ }^{\circ}\text{C}$, and a second cooling step to room temperature in both zones at a maximum rate of $2\text{ }^{\circ}\text{C min}^{-1}$.

4.3.2. Morphology and Composition Characterization

The morphologies and crystal structures of SnS_2 nanoflakes on FTO were characterized using scanning electron microscope (SEM, JEOL 7000F, 10 kV), transmission electron microscope (TEM, JEOL 2100, 200kV), atomic force microscopy (NaioAFM, Nanosurf, static force mode) and parallel beam X-ray diffraction (XRD, PANalytical Empyrean, $\text{Cu-K}\alpha$, 45 kV, 40 mA). The ICDD# 00-023-0677, ICDD# 04-03-3325, ICDD# 00-014-0619 and ICDD#00-039-0354 were used as standard patterns for 2H- SnS_2 , 4H- SnS_2 , Sn_2S_3 and SnS respectively.

X-ray photoelectron spectroscopy (XPS) compared surface compositions of the as-grown SnS_2 nanoflakes with those following tests in sulfuric acid and in phosphate buffer. Measurements were performed using a Phi 5600 instrument that utilized a monochromated $\text{Al-K}\alpha$ anode operating at 13.5 kV and 300 W with photoelectron collection in 25 meV steps at a 23.5 eV pass energy.^[146, 147] Similarly, inductively coupled plasma optical emission spectrometry (ICP-OES, Agilent 5100) was also used to measure the concentration of dissolved tin ions in the electrolyte after degradation tests.

4.3.3. Optoelectronic Characterization

Wavelength-dependent light harvesting efficiency (LHE) of the SnS_2 photoanode was measured using an integrating sphere with white-light illumination from the Xe lamp (model 6258, Oriel) and calculated from the measured reflection (R) and transmission (T) as $\text{LHE}(\lambda) (\%) = 100\% - \text{R}(\lambda) (\%) - \text{T}(\lambda) (\%)$.

Raman spectra of the samples was obtained using XploRa Raman microscope (Horiba Scientific, USA) operating with a 532 nm laser. Laser light was focused on the sample using a 100x magnification lens from Olympus, and a 2400-line grating was used along with accumulation time of 2s and 25 repetitions to collect the signal.

The photoluminescence (PL) of SnS_2 nanoflakes was measured using a Horiba iHR550 Spectrometer with 405 nm fiber coupled laser and Horiba Synapse CCD camera. Similarly, time-resolved photoluminescence (TRPL) was measured using Becker and Hickl's time correlated single photon counting system (SPC-150) and ID Quantique's single photon avalanche

photodiode (ID-100-50-STD). The pump was a 20 picosecond pulsed laser with a frequency of 19.4 MHz, average power of 0.5 μW and a spot size of about 1 mm^2 . Hence, the instantaneous peak intensity of the pulsed laser incident on the sample was about 128 mWcm^{-2} , which is similar to one-sun condition.

Intrinsic mobility of photoexcited charge carriers in SnS_2 nanoflakes was estimated using time-resolved THz spectroscopy (TRTS). The vertical nanoflakes on quartz were excited by ~ 100 fs duration, 400 nm pulses from a regeneratively amplified 1 kHz repetition rate Ti:sapphire laser at normal incidence as described in previous reports.^[148, 149] The sample was placed behind a 1.5 mm aperture in the center of a ~ 3 mm 400 nm beam spot to ensure uniform excitation of the studied portion. THz probe pulses were generated using optical rectification of the 800 nm pulses from the same laser source in a 1 mm thick [110] ZnTe crystal and focused onto the sample by a combination of off-axis parabolic mirrors. Transmitted THz pulses were focused onto a second [110] ZnTe crystal and detected using free space electro-optic sampling.

4.3.4. Photoelectrochemical Characterization

Electrode preparation:

The SnS_2 electrodes were made by bonding nickel-chromium alloy wire to the FTO using silver epoxy (Ted Pella #16043), which was then covered using non-conductive epoxy (Loctite 1C). For single crystal electrodes, mm-size single crystals of SnS_2 were stuck directly onto silver epoxy and any surface other than SnS_2 was covered using non-conductive epoxy. Similarly, the exfoliated SnS_2 electrode was prepared by mechanically exfoliating single crystal SnS_2 pieces and transferring to ITO using thermal release tape.

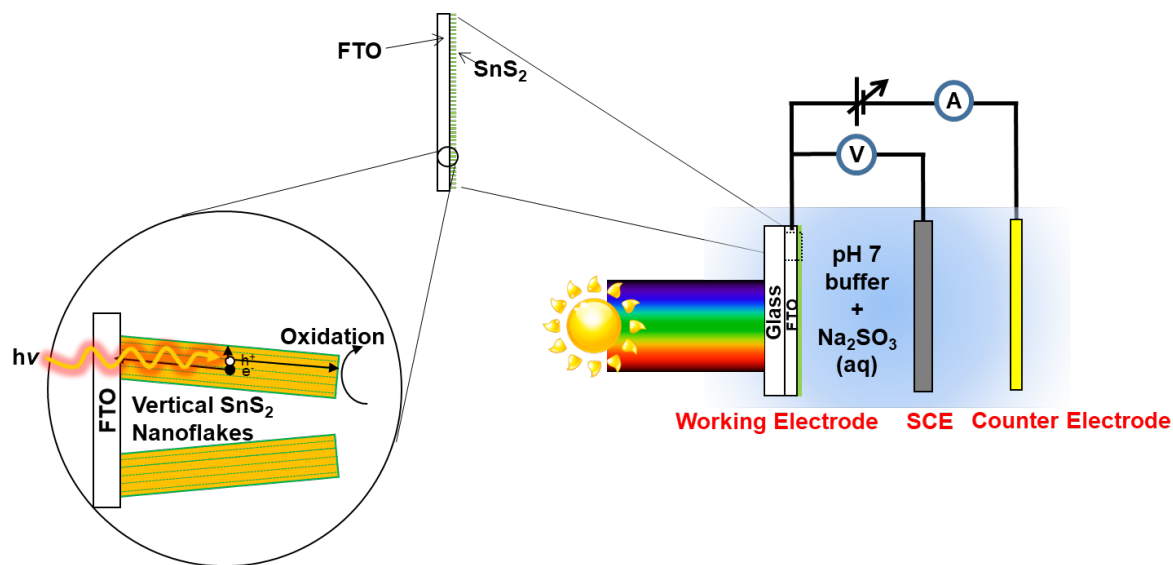


Figure 4-2. Schematic of the photoelectrochemical (PEC) measurement setup using SnS₂ photoanode. All photoelectrochemical measurements were performed in a three-electrode configuration where SnS₂ nanoflakes on FTO was the working electrode while saturated calomel electrode (SCE) was the reference electrode, and platinum wire was the counter electrode. A magnetic stirrer was used together with nitrogen gas purging to eliminate any mass transfer limitations.

Photoelectrochemical measurements:

All photoelectrochemical measurements were performed in a three-electrode configuration (Figure 4-2) where the electrode with SnS₂ nanoflakes on FTO was the working electrode while saturated calomel electrode (SCE) was the reference electrode and platinum wire was the counter electrode. All voltages measured using SCE were converted to reversible hydrogen electrode (RHE) using the equation:

$$V_{RHE} = V_{SCE} + 0.059 * pH + 0.244 \quad (\text{Eq 4-1})$$

A magnetic stirrer was used together with nitrogen gas purging to eliminate any mass transfer limitations. In the linear sweep voltammetry (LSV) measurements, the sweep rate was set to 10 mV/s.

Simulated sunlight for these measurements was provided by a Xenon lamp (model 6258, Oriel) equipped with an AM1.5G filter (model 81094, Oriel), and the spectral irradiance was measured by a spectrometer (model USB2000+Rad, Ocean Optics). During the PEC tests, the incident light was chopped/blocked at regular intervals to establish the dark current level.

For incident photon to current efficiency (IPCE) measurements, monochromatic light at various wavelengths were produced with a monochromator (Cornerstone 130 1/8 m, Newport), and the following equation was used:

$$\text{IPCE } (\lambda) = \frac{1240 * J_{\text{ph}} \left[\frac{\text{mA}}{\text{cm}^2} \right]}{P_{\lambda} \left[\frac{\text{mW}}{\text{cm}^2} \right] * \lambda [\text{nm}]} * 100\% \quad (\text{Eq 4-2})$$

Several electrolytes were used throughout this project: 1 M H₂SO₄ (pH 0.5), 1 M H₂SO₄ + 0.1 M KI (pH 0.5), 1 M phosphate buffer (pH 7), 1 M phosphate buffer + 1 M Na₂SO₃ (pH 7) and 0.5 M Na₂SO₄ (pH 7.6). The phosphate buffer was prepared by dissolving potassium phosphate monobasic (KH₂PO₄) and potassium phosphate dibasic (K₂HPO₄) in deionized water while sulfuric acid of unit molarity was prepared by diluting commercially available concentrated acid with deionized water.

Deposition of copper (Cu) and lead oxide (PbO_x) particles:

Copper particles were electrodeposited onto SnS₂ nanoflakes in 1 M CuSO₄·5H₂O (pH 3.8) by applying cyclic voltammetry (20 times) from 0.74 to 0.57 V_{RHE}. Similarly, PbO_x was photoelectrochemically deposited in 0.1 M Pb(NO₃)₂ + 1 M HNO₃ by applying voltage from 1.28 to 2.08 V_{RHE} over 2 minutes. Then, a constant voltage of 1.78 V_{RHE} was maintained for 6 minutes to allow PbO_x particle growth.

4.4. Results and Discussion

4.4.1. Optimization of Synthesis Parameters

The custom-built CSS system was designed to allow independent control of source temperature (T_{src}), substrate temperature (T_{sub}) and source-substrate separation (d_{ss}). Controlled experiments were carried out to determine the optimal growth conditions (T_{src} , T_{sub} , d_{ss} and growth duration). X-ray diffraction (XRD), scanning electron microscopy (SEM) and PEC measurements with Na₂SO₃ hole scavenger were carried out to characterize the purity, morphology and PEC performance of the nanoflakes at each growth condition. T_{src} was fixed at 525 °C because lower temperatures (< 450 °C) did not cause sublimation and higher temperatures (> 600 °C) led to the deposition of black Sn₂S₃ particles. The growth duration was fixed at 30 minutes because longer durations resulted in only small increases in SnS₂ nanoflake length and performance due to conversion of the source material to SnS. Increasing T_{sub} from 424 °C to 453 °C caused the

growth of taller and wider SnS₂ nanoflakes with higher PEC performance, but further increasing T_{sub} to 471 °C caused the formation of Sn₂S₃ nanorods, which produced extremely low photocurrent (Figure 4-3a-c). Then, keeping T_{sub} fixed at 450 °C, and decreasing d_{ss} from 19 mm to 10 mm resulted in taller nanoflakes with increased opacity (Figure 4-3d-f) as expected because the concentration of the SnS₂ vapor is higher closer to the source. The maximum photocurrent of 4.5 mAcm⁻² was obtained from the tallest nanoflakes (~ 1.5 μm height) grown with d_{ss} = 10 mm. Positioning a boat containing sulfur powder (at ~ 200 °C) close to the source boat containing SnS₂ powder during the growth suppressed the conversion of the SnS₂ source to SnS and resulted in increased sublimation and a further increase of nanoflake height to ~2.3 μm. However, these nanoflakes produced much lower photocurrents, thus placing the optimal nanoflake height in the 1.5 - 2.3 μm range, but likely closer to 1.5 μm.

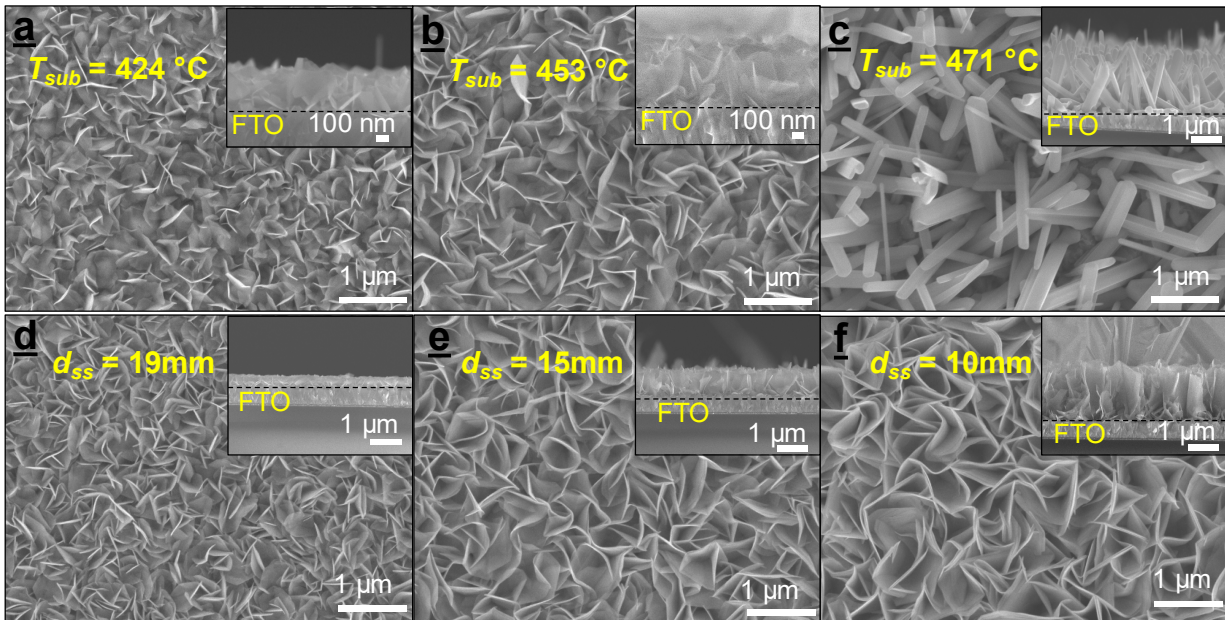


Figure 4-3. Optimization of SnS₂ nanoflake growth by CSS. (a-c) SEM images of nanoflakes synthesized with T_{sub} = 424 °C, 453 °C and 471 °C; (d-f) SEM images of nanoflakes synthesized with d_{ss} = 19 mm, 15 mm and 10 mm.

The insets show respective cross-section views.

During optimization, the photocurrent at 1.23V_{RHE} in the electrolyte with hole scavenger was measured as a function of the T_{sub} , t and d_{ss} . According to Figure 4-4, increasing T_{sub} from 424°C to 453°C only increased the photocurrent from 1 to 1.4 mAcm⁻². Similarly, increasing growth time from 20 min to 60 min only improved photocurrent from 1 to 2 mAcm⁻². On the contrary, decreasing d_{ss} from 19 mm to 10 mm resulted in more than doubling of the photocurrent from

2.1 to 4.5 mAcm⁻². This suggests that d_{ss} is the most sensitive synthesis parameter to control the PEC performance of SnS₂ nanoflake photoanodes. As the substrate is brought closer to the source, the vapor concentration increases significantly such that the tall and vertical nanoflakes grow rapidly. Unlike the other parameters (i.e. T_{sub} , T_{src} and t), d_{ss} is the cheapest and simplest parameter to tune, which makes it very powerful in CSS synthesis.

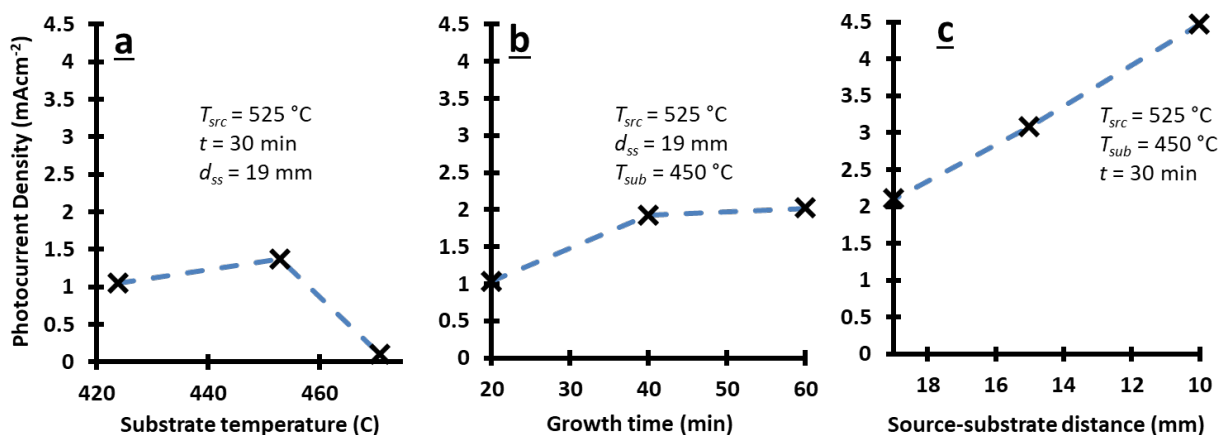


Figure 4-4. Photocurrents obtained from SnS₂ nanoflake photoanodes at 1.23V_{RHE} as a function of (a) substrate temperature and (b) growth time and (c) source-substrate distance. Test condition: 1sun illumination, and electrolyte containing water, 1M pH7 phosphate buffer and 1M Na₂SO₃.

4.4.2. Measurement of PEC Performance

Based on the preceding optimization experiments, the optimal nanoflake height was $\sim 1.5\text{ }\mu\text{m}$, which could be obtained with $T_{sub} = 450\text{ }^{\circ}\text{C}$, $t = 30\text{ min}$ and $d_{ss} = 10\text{ mm}$. Several SnS₂ nanoflake photoanodes were prepared under these experimental conditions and their PEC performance was measured by linear sweep voltammetry (LSV) in different electrolytes for comparison (Figure 4-5a). The same SnS₂ nanoflakes that produced a maximum photocurrent of 4.5 mAcm⁻² at 1.23 V_{RHE} under AM1.5G illumination in phosphate buffer + 1 M Na₂SO₃, produced 2.6 mAcm⁻² in 0.5 M Na₂SO₄ (i.e. for water oxidation) without the Na₂SO₃ hole scavenger. The aqueous solution of Na₂SO₄ is commonly used to characterize water oxidation performance of photoanodes because SO₄²⁻ ions require a high potential of 2.01 V_{RHE} to be oxidized to S₂O₈²⁻ while water can be oxidized to oxygen at 1.23 V_{RHE}.^[150] The photocurrent of 2.6 mAcm⁻² obtained from our nanoflakes is about 1.7 times the photocurrent reported previously from CVD-grown vertical SnS₂ nanoflakes at 1.23 V_{RHE} in 0.5 M Na₂SO₄ under similar light illumination, and represents a new record for photocurrent, to the best of our knowledge.^[79]

However, since the photocurrent produced by the SnS₂ nanoflakes decreased rapidly within a few minutes in Na₂SO₄ solution (also discussed in section 2.4), it is not meaningful to report an efficiency for photoelectrochemical water oxidation. Instead, an electrolyte containing 0.1 M KI and 1 M H₂SO₄, in which SnS₂ nanoflakes are very stable and produce a photocurrent of 2.7 mAcm⁻² at 0.6 V_{RHE}, was used to further characterize the performance and measure the wavelength-dependent incident photon to current efficiency (IPCE, also known as external quantum efficiency) for photoelectrochemical iodide oxidation. The excellent ability of the optimized SnS₂ nanoflakes to absorb and generate photocurrent is evident in the IPCE (Figure 4-5b) measured under both front-side (electrolyte-side) and back-side (glass-side) illumination in 0.1 M KI + 1 M H₂SO₄ at a fixed voltage of 0.6 V_{RHE}. As shown in Figure 4-5b, the IPCE with front illumination reaches almost 100% at shorter wavelengths and that with back illumination peaks around 62% at 440nm. Both front and back IPCE plots have an onset near 580 nm. At shorter wavelengths, IPCE with back illumination is lower than that with front illumination because the light is absorbed or scattered by the glass/FTO substrate, whereas this difference is not significant at longer wavelengths. The LSV and IPCE measurements were validated by integrating the IPCE over the measured spectral irradiance of the incident light from the Xe lamp solar simulator used during the PEC tests. This resulted in a photocurrent of 3.0 mAcm⁻² for back illumination, which is very similar to the photocurrent of 2.7 mAcm⁻² measured at 0.6 V_{RHE} by LSV.

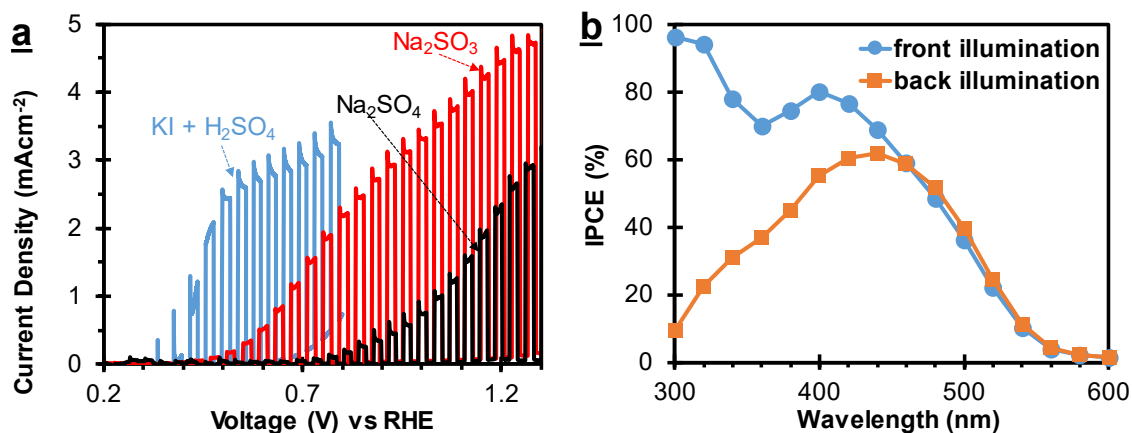


Figure 4-5. (a) Linear sweep voltammetry of optimized SnS₂ nanoflakes in 0.5 M Na₂SO₄, 1 M phosphate buffer + 1 M Na₂SO₃, and 0.1 M KI + 1 M H₂SO₄ with back illumination; (b) Incident photon-to-current conversion efficiency (also known as external quantum efficiency) of vertical SnS₂ nanoflakes measured with front and back illumination in 0.1 M KI + 1 M H₂SO₄ at 0.6 V_{RHE}.

4.4.3. Characterization of Structural and Optoelectronic Properties

In order to investigate the source of high photocurrent and the reason behind the existence of an optimum height of the SnS₂ nanoflakes, the structural and optoelectronic properties of the optimized nanoflakes were analyzed. The high-resolution TEM image of a nanoflake in Figure 4-6a along with the corresponding selected area electron diffraction (SAED) pattern (inset) shows that the SnS₂ nanoflake is crystalline and possesses hexagonal crystal structure. The measured in-plane d-spacing of 3.16 Å is consistent with that of the (100) planes of 2H-SnS₂ (ICDD# 00-023-0677). It is also evident from the SAED pattern with [001] zone axis that the flat surface of the SnS₂ nanoflakes is formed by the (001) basal planes of SnS₂. In addition, although the SAED pattern is dominated by bright spots originating from a SnS₂ single crystal nanoflake, the faintly visible ring-like pattern indicates a partially polycrystalline character of the nanoflakes.

Furthermore, the low magnification TEM image in Figure 4-6b shows that the nanoflakes have surfaces formed by incomplete basal planes that contain small holes/patches (~5 nm), which are stacked on top of fully-formed single crystalline basal planes. The holes/patches could be the result of non-uniform growth of new basal planes on existing nanoflake surfaces limited by island nucleation and lateral motion of steps at a low supersaturation of SnS₂ vapor, as predicted by crystal nucleation theory, and as observed in the CVD growth of 2D monolayers.^[151-154] However, such patches were not reported in the CVD-grown vertical SnS₂ nanoflakes, which could be due to higher supersaturation of SnS₂ vapor in their experiments.^[34, 79] An even lower magnification TEM image in Figure 4-6c shows the presence of discrete steps in our nanoflakes. It is assumed that both the nanoscale holes/patches (Figure 4-6a and b) and the microscale steps (Figure 4-6c) on the surface of the nanoflakes provide additional edges that can act as electrochemically active sites and boost the rate of surface charge transfer, leading to enhanced photocurrent. The edges in MoS₂ electrocatalysts are reported to have a similar role.^[82, 155] While the edges of these steps, holes and patches can also act as carrier trapping centers, the enhancement in surface charge transfer due to increased density of electrochemically active sites can outweigh the loss due to trap-mediated recombination. The role of these edges on the PEC performance will be addressed experimentally and discussed in the later sections.

The XRD pattern of the optimized nanoflakes on FTO (Figure 4-6d) shows the most dominant peaks from (001) and (100) crystal planes, and matches well with 2H-SnS₂ standard. Similarly,

the room temperature Raman characterization (Figure 4-6e) also suggests that our optimized nanoflakes are of high quality. A narrow band is observed at 313.5 cm^{-1} , consistent with the out-of-plane (A_{1g}) vibrational mode of 2H-SnS₂ measured by several groups.^[29, 130, 156, 157] According to a previous report,^[156] 2H-SnS₂ also exhibits a single band at 205.5 cm^{-1} , unlike 4H-SnS₂ or 18R-SnS₂ that exhibit multiple bands near that wavenumber. Hence, a single band around 204.5 cm^{-1} shown in the 50 times enlarged spectrum in Figure 4-6e can be assigned to in-plane (E_g) vibrational mode of 2H-SnS₂.

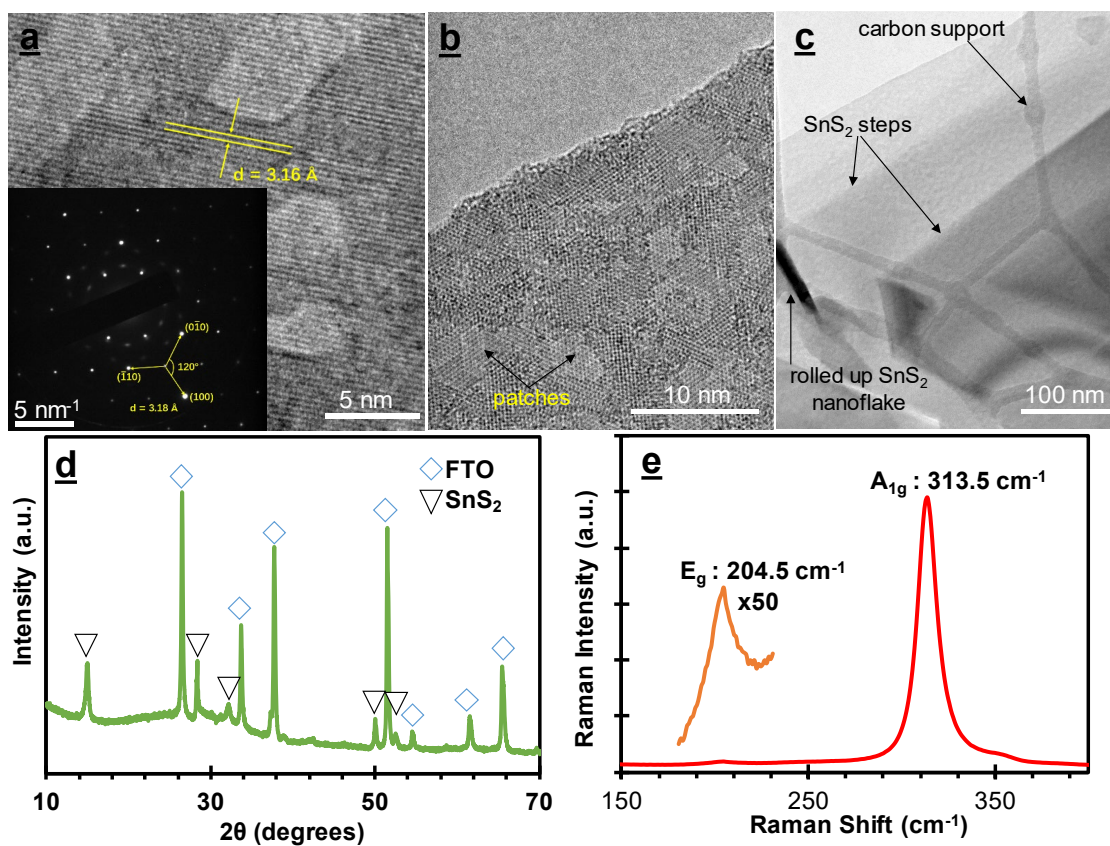


Figure 4-6. Characterization of optimized SnS₂ nanoflakes. (a) High-resolution TEM image of a nanoflake with the corresponding SAED pattern (inset); (b) TEM image of the nanoflake showing partially polycrystalline structure with holes/patches; (c) TEM image of the nanoflake showing stepped structure; (d) XRD of SnS₂ nanoflakes on FTO and (e) Raman spectroscopy of SnS₂ nanoflakes.

The optimized nanoflakes exhibit high light harvesting efficiency (LHE), which is essential for yielding high photocurrent. The LHE of optimized nanoflakes was measured using an integrating sphere, as described in a previous report.^[158] As shown in Figure 4-7a, LHE of about 90% was achieved at shorter wavelengths with absorption onset at around 580 nm. The Tauc plot in Figure

4-7b shows the indirect bandgap of SnS₂ to be about 2.1 eV, which is in agreement with other reports in the literature.^[25-27, 157] This indirect band gap is also evident from the broad photoluminescence (PL) peak centered at 588 nm (2.11 eV) in Figure 4-7c.

Another important factor that impacts the performance of photoanodes is diffusion length (L_D) of the photoexcited charge carriers, which can be calculated from carrier lifetime (τ) and mobility (μ) using Equation (4-3), where k_B is the Boltzmann constant, T is absolute temperature and e is elementary charge.

$$L_D = \sqrt{\left(\frac{k_B T}{e} * \mu\right) * \tau} \quad (\text{Eq 4-3})$$

The radiative charge carrier lifetime in the optimized SnS₂ nanoflakes was determined using time-resolved photoluminescence (TRPL) decay of the 2.11 eV peak, corresponding to the band gap emission, after exciting with 405 nm laser at near one-sun peak excitation intensity ($\sim 128 \text{ mWcm}^{-2}$), as shown in Figure 4-7d. Immediately after the excitation, a fast response with lifetime of 78 picoseconds is observed, which is attributed to the response of the measurement system. After fitting a double exponential, the radiative carrier lifetime in SnS₂ nanoflakes is estimated to be $\sim 1.3 \text{ ns}$.

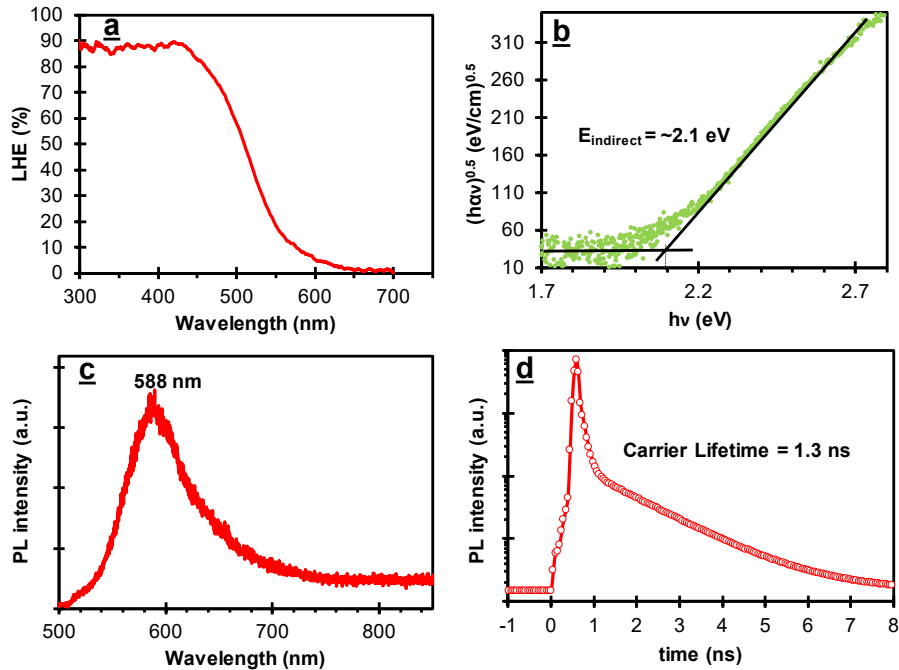


Figure 4-7. (a) Light Harvesting Efficiency (LHE); (b) indirect bandgap Tauc plot; (c) steady-state photoluminescence spectrum and (d) time-resolved photoluminescence of vertical SnS₂ nanoflakes following photoexcitation with 405 nm, $\sim 20 \text{ ps}$ pulses.

Similarly, a contact-free time-resolved terahertz spectroscopy (TRTS) technique was used to study the dynamics of photoexcited free charge carriers on picosecond time scales, and estimate intrinsic mobility of SnS₂ nanoflakes.^[159-164] CSS-grown SnS₂ vertical nanoflakes were optically excited with 400 nm laser pulses with 100 fs duration and with 28 μJcm⁻² fluence, and transient photoconductivity (Figure 4-8a) was measured using a terahertz probe in the 0.25 – 1.70 THz frequency range, which corresponds to 1-7 meV energy range. With energy in meV range, terahertz pulses are absorbed by the free carriers, and transient change in transmission of the terahertz probe pulse peak is a measure of photoconductivity (Figure 4-8a). For comparison, chemical vapor transport (CVT)-grown SnS₂ single crystals were also measured in the same manner. Photoconductivity in both single crystal SnS₂ and vertical SnS₂ nanoflakes exhibits a multi-exponential decay. The fastest component (2 - 3 ps) is more pronounced at higher excitation fluence values, and can be thus ascribed to carrier-carrier scattering. The slower, 10 - 15 ps decay likely represents carrier trapping at defect and edge states. Finally, a much slower component that is attributed to free carrier recombination, decays over >250 ps. The corresponding free carrier lifetime is difficult to determine accurately from TRTS measurement as it is limited by the pump-probe delay that is available to us. However, while ~ 250 ps is the lower limit of the photoexcited carrier lifetime, the radiative lifetime of ~1.3 ns determined by TRPL is the upper limit. Thus, the lifetime of the photoexcited carriers in the optimized vertical nanoflake array can be placed in (0.25 - 1.30 ns) range. The lower end of this range is similar to the radiative lifetime of 0.25 ns measured for exfoliated single crystals,^[29] while the higher end of the range is closer to the values of 2.4 ns and 3.0 ns measured for CVD-grown thin (20 nm) and thick (32 nm) SnS₂ nanoflakes, respectively.^[157]

In addition to providing insights into free carrier lifetimes after photoexcitation, TRTS allows us to measure intrinsic mobility. Photoexcitation-induced changes in the amplitude and the phase of the THz pulse waveform transmitted through the sample^[159, 165-167] were used to extract complex photoinduced change in conductivity 20 ps after excitation with 28 μJ/cm², 400 nm pulses. At 20 ps, carrier-carrier scattering is no longer appreciable, and thus intrinsic carrier scattering time and mobility can be determined. Real ($\Delta\sigma_1$) and imaginary ($\Delta\sigma_2$) photoconductivity components are plotted in Figure 4-8b and c for single crystals and vertical nanoflakes respectively as a function of THz frequency (ω). In general, the complex conductivity ($\hat{\sigma}$) of both of these samples can be described by Equation (4-4), (also known as the Drude-Smith model), where N is the

charge carrier density, m^* is the effective carrier mass, τ_{DS} is the effective scattering time and the c -parameter characterizes the degree of carrier localization due to the presence of boundaries.^[166, 168-176]

$$\hat{\sigma}(\omega) = \frac{Ne^2\tau_{DS}/m^*}{1-i\omega\tau_{DS}} \left[1 + \frac{c}{1-i\omega\tau_{DS}} \right] \quad (\text{Eq 4-4})$$

The c -parameter and τ_{DS} were first determined by fitting the measured frequency-resolved complex conductivity to this model. Then, intrinsic and long-range mobility of carriers in our samples were estimated using Equation (4-5) and (4-6) respectively, where a previously-reported value of effective mass $m^* = 0.375m_e$ was used.^[177]

$$\mu_{intrinsic} = \frac{e}{m^*} \tau_{DS} \quad (\text{Eq 4-5})$$

$$\mu_{long-range} = \frac{e}{m^*} \tau_{DS} (1 + c) \quad (\text{Eq 4-6})$$

For single crystal SnS₂, Equation (4-5) reduces to the Drude model (with $c = 0$) and the mobility is estimated to be 800 cm²V⁻¹s⁻¹, which is similar to a theoretically-predicted value of electron mobility in monolayer SnS₂.^[30] However, for vertical nanoflakes, the localization parameter is nonzero ($c = -0.72$) due to confinement of carriers within individual nanoflakes, and the intrinsic and long-range mobilities are estimated to be 330 cm²V⁻¹s⁻¹ and 90 cm²V⁻¹s⁻¹ respectively. This intrinsic mobility is slightly higher than that reported in previous studies and approaches the theoretically predicted one, which is a testament to the high crystallinity of the nanoflakes and low defect concentration.^[29, 30, 124, 178] Since the important charge transport in PEC applications occurs within individual nanoflakes, the high intrinsic mobility can improve the overall photocurrent in SnS₂ photoanodes.

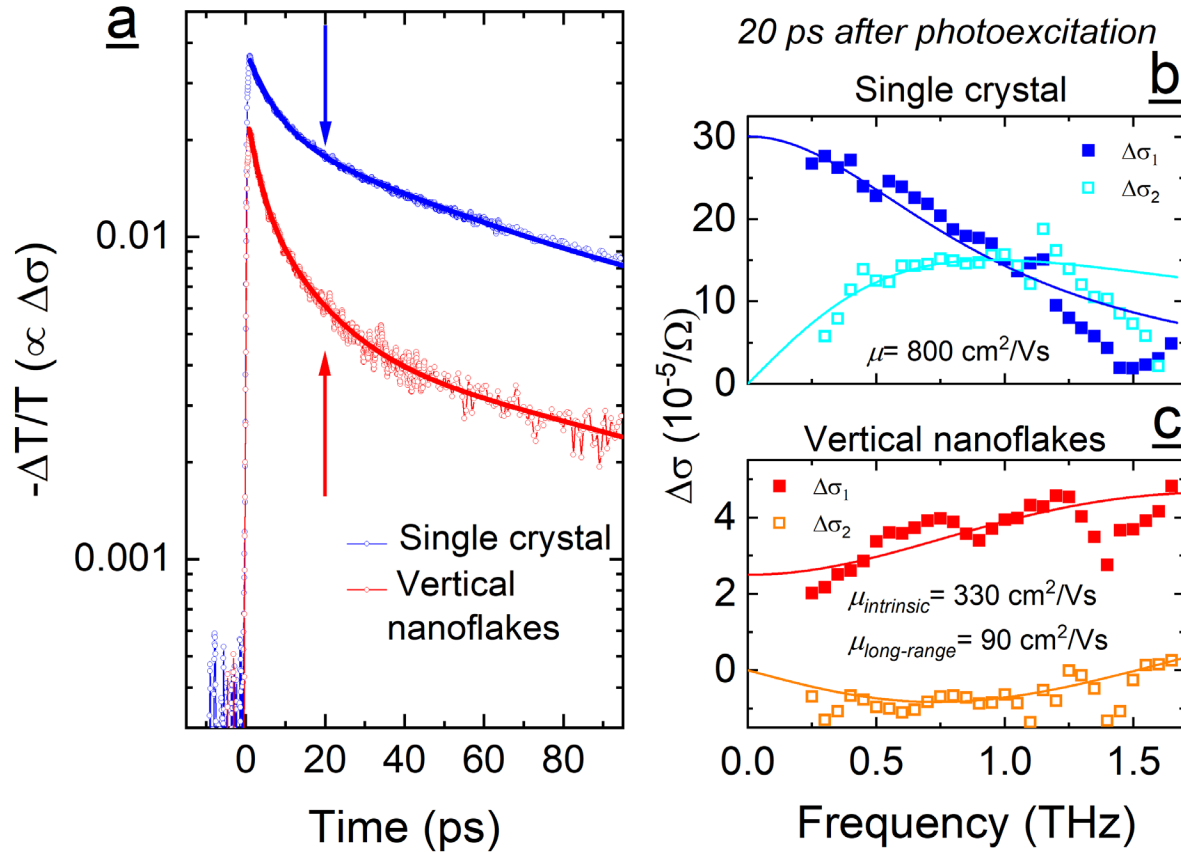


Figure 4-8. (a) Time-resolved terahertz spectroscopy showing picosecond dynamics of photoconductivity in single crystal SnS_2 and vertical SnS_2 nanoflakes following photoexcitation with 400 nm, ~ 100 fs pulses. Real ($\Delta\sigma_1$) and imaginary ($\Delta\sigma_2$) components of THz photoconductivity of (b) single crystal SnS_2 and (c) vertical SnS_2 nanoflakes on quartz measured at 20 ps after the excitation. The lines in (b-c) represent global fit for real and imaginary components of the conductivity to the Drude-Smith model.

Our finding of an optimum height of SnS_2 nanoflakes is expected to be due to a balance between two competing requirements - the generation of photoexcited charges by optical absorption, and the diffusion of those photoexcited charges. In terms of optical absorption, $\sim 2 \mu\text{m}$ thick SnS_2 is required to absorb most of the photon energies. Similarly, in terms of photoexcited carrier diffusion, combining the carrier lifetime (0.25 - 1.30 ns) and TRTS mobility using Equation (4-3) yields the diffusion length of $\sim (0.4 - 1.0 \mu\text{m})$ in our nanoflakes. As expected, the optimized nanoflake height of $\sim 1.5 \mu\text{m}$ falls in between the absorption depth and the diffusion length.

Optimized height is likely not the only reason for the enhanced photocurrent in our SnS_2 nanoflakes compared to the previously-reported CVD-grown SnS_2 nanoflakes, which also had high packing density and heights in the range of few micrometers, yet achieved significantly

lower photocurrent.^[79] Upon closer examination of the nanostructure of our SnS₂ nanoflakes using high magnification SEM (Figure 4-9a), it can be observed that our nanoflakes consist of discrete steps on the sides (which were also observed by TEM in Figure 4-9c). It is believed that the edges are the sites of the electrochemical reaction, so the photocurrent could be improved by spreading these reaction sites over the entire nanoflake, similar to the case of stepped MoS₂.^[179] These steps in CSS-grown SnS₂ nanoflakes are formed either due to nucleation and growth of new basal planes onto the sides of the existing basal planes at high vapor concentrations or due to interaction of neighboring nanoflakes during the prolonged growth. The steps on the side of the nanoflakes are also visible in the AFM image in Figure 4-9b, which was taken from a horizontally laid piece of a nanoflake obtained by separating the as-grown SnS₂ nanoflakes from the growth substrate by sonicating in ethanol, followed by drop-casting onto a Si/SiO₂ substrate. The height profile in Figure 4-9c shows that the height of the discrete steps is about 4-5 nm while the overall thickness of the nanoflake is about 30 nm, which is similar to the average nanoflake thickness measured using SEM.

In order to support our claim that CSS grown SnS₂ nanoflakes contain multiple edge sites which are electrochemically active, Cu particles were deposited by electrochemical reduction and PbO_x particles by photoelectrochemical oxidation. As shown in Figure 4-9d (Cu) and Figure 4-9e (PbO_x), the nanoparticles are preferentially deposited on the top edges of the nanoflakes as well as at the steps on the sides of the nanoflakes, indicating that multiple edge sites are available in every nanoflake for the redox reaction. This not only demonstrates the presence of these steps but also that the steps and edges in SnS₂ are electrochemically more active than the other regions, which has been previously reported for MoS₂.^[179] The selective deposition of nanoparticles has also been used by many other researchers to visualize and identify active sites.^[84, 180] Since each of our optimized SnS₂ nanoflakes contains additional active sites on their faces due to the presence of steps, the overall photocurrent can be expected to be higher than CVD-grown nanoflakes that lack the stepped structure.

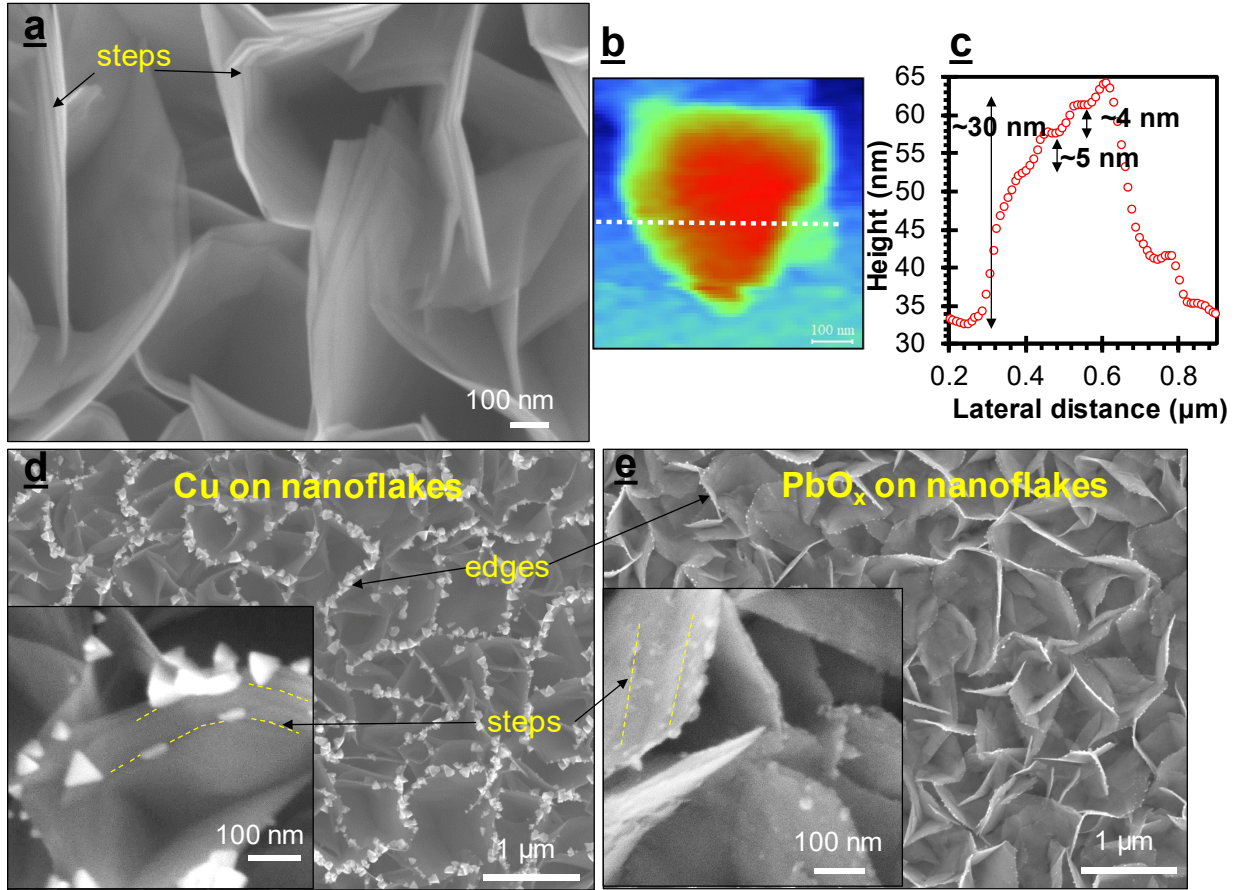


Figure 4-9. Morphological characterization of SnS₂ nanoflakes: (a) SEM image showing steps, (b) AFM image of a broken piece of SnS₂ nanoflake with false color map, (c) corresponding AFM height profile along the dotted line. SEM images of SnS₂ nanoflakes with (d) Cu particles deposited by reduction and (e) PbO_x particles deposited by oxidation, highlighting the edges and steps on the nanoflakes.

It is acknowledged that the photocurrent of 2.6 mAcm⁻² for water oxidation is still lower than the maximum possible photocurrent of $J_{max} = 9.2 \text{ mAcm}^{-2}$, which is estimated by integrating irradiance over all the wavelengths shorter than the band gap wavelength ($\lambda_{gap} = 588 \text{ nm}$) of SnS₂ using Equation 4-7, where e is elementary charge, h is Planck's constant, c is speed of light and I is irradiance from the solar simulator.

$$J_{max} \left(\frac{A}{cm^2} \right) = \frac{e}{hc} \int_0^{\lambda_{gap}} I \left(\frac{W}{cm^2 nm} \right) * \lambda(m) * d\lambda(nm) = 9.2 \frac{mA}{cm^2} \quad (\text{Eq 4-7})$$

The presence of low photocurrent in comparison to the maximum possible photocurrent can be understood using Equation 4-8, where $\eta_{absorption}$, $\eta_{separation}$, and $\eta_{transfer}$ are light absorption/charge generation, charge separation and charge transfer efficiencies respectively.

$$J_{H_2O} = J_{max} * \eta_{absorption} * \eta_{separation} * \eta_{transfer} = 2.6 \frac{mA}{cm^2} \quad (\text{Eq 4-8})$$

The charge generation or absorption efficiency ($\eta_{absorption}$) of SnS₂ nanoflakes can be determined by multiplying the integrand of Equation 4-7 with light harvesting efficiency (LHE) and dividing the result by J_{max} , as shown in Equation 4-9.

$$\eta_{absorption} = \frac{\frac{e}{hc} \int_0^{\lambda_{gap}} I \left(\frac{W}{cm^2 nm} \right) * \lambda(m) * LHE_{\lambda} * d\lambda(nm)}{\frac{e}{hc} \int_0^{\lambda_{gap}} I \left(\frac{W}{cm^2 nm} \right) * \lambda(m) * d\lambda(nm)} = \frac{4.85 \frac{mA}{cm^2}}{9.2 \frac{mA}{cm^2}} = 52\% \quad (\text{Eq 4-9})$$

When a hole scavenger such as Na₂SO₃ is added to the electrolyte, the charge transfer limitation is removed and the observed photocurrent is only due to other effects. Hence,

$$J_{Na_2SO_3} = 9.2 \left(\frac{mA}{cm^2} \right) * \eta_{absorption} * \eta_{separation} = 4.5 \frac{mA}{cm^2} \quad (\text{Eq 4-10})$$

Hence, the charge transfer efficiency during water oxidation can be estimated using Equations 4-8 and 4-10.

$$\eta_{transfer} = \frac{J_{H_2O}}{J_{Na_2SO_3}} = \frac{2.6 \left(\frac{mA}{cm^2} \right)}{4.5 \left(\frac{mA}{cm^2} \right)} \sim 57\%$$

Finally charge separation efficiency can be estimated using Equation 4-11.

$$\eta_{separation} = \frac{J_{H_2O}}{J_{max} * \eta_{transfer} * \eta_{absorption}} = \frac{2.6 \left(\frac{mA}{cm^2} \right)}{9.2 \left(\frac{mA}{cm^2} \right) * 0.57 * 0.52} \sim 95\% \quad (\text{Eq 4-11})$$

The high charge separation efficiency of 95% is due to vertical alignment of SnS₂ nanoflakes and high mobility of charge carriers in the basal planes. It proves our hypothesis that vertical alignment enhances charge transport in SnS₂ nanoflakes.

On the contrary, both charge generation and charge transfer efficiencies are low, and account for most of the loss in our nanoflake photoanodes. The low charge transfer efficiency of only 57% could be a result of slow kinetics of water oxidation reaction that forces holes to be accumulated at the SnS₂-water interface and recombine with photoexcited electrons. One way to mitigate this issue is by employing co-catalysts at the nanoflake/electrolyte interface to enhance this charge transfer and lower surface recombination of photoexcited charge carriers. Similarly, the low absorption efficiency could be due to un-optimized packing density of SnS₂ nanoflakes and the indirect band gap of SnS₂ that leads to weaker absorption of light.

4.4.4. Influence of Synthesis Parameters on Nanoflake Characteristics

Several experimental parameters such as vacuum level in the quartz chamber, preheating time for SnS₂ powder, source temperature, substrate temperature, source-substrate separation, growth duration, coolant temperature, coolant flow rate, CH₄ and air flow rate, etc. can be adjusted during CSS synthesis. However, only three most important parameters (i.e. substrate temperature, source-substrate separation and growth duration) were investigated in more detail because these parameters capture the overall effect of varying other parameters, and are the most useful in reproducing the results in a different CSS system. For example, flow rate of CH₄ and air ultimately determine the source temperature. Similarly, the coolant temperature and coolant flow rate ultimately determine the substrate temperature.

Although vacuum level in the quartz chamber was not investigated in detail, it is important in controlling the purity of SnS₂ nanoflakes during growth. In general low vacuum level is desired such that the quartz chamber contains negligible amounts of reactive oxygen gas or moisture in order to prevent tin oxide formation. Similarly, source temperature is another important synthesis parameter however, the temperature range for sublimation of SnS₂ nanoflakes is small since at high temperatures, the SnS₂ undergoes phase change to SnS/Sn₂S₃ phases and at low temperatures, SnS₂ is unable to sublime. Hence, source temperature was not studied in detail.

Among the three parameters that were studied, growth duration was the least significant. Simply prolonging growth duration increased the height and lateral size of SnS₂ nanoflakes, however, the growth rate declined after a while due to conversion of SnS₂ source powder to SnS phase, which requires higher temperature to sublime. Although it wasn't explicitly verified, it is expected that the excellent optoelectronic properties of SnS₂ nanoflakes remained the same regardless of the growth duration. In terms of stepped morphology, it was unclear whether the growth duration had any impact.

Another important synthesis parameter studied was substrate temperature, which mostly influenced the phase and grain size of SnS₂ nanoflakes. At too low substrate temperatures, the SnS₂ nanoflakes had small height and lateral size. However, at too high substrate temperatures, the SnS₂ nanoflake morphology was replaced by Sn₂S₃ nanorod morphology. Hence, the substrate temperature is expected to strongly influence the optoelectronic properties of SnS₂ nanoflakes.

The most influential synthesis parameter for height and stepped morphology of SnS₂ nanoflakes was expected to be source-substrate distance. As discussed in the earlier section, the nanoflake height was significantly increased simply by decreasing source-substrate distance. This is also expected to increase vapor concentration and lead to fast nucleation and growth of basal planes resulting in a stepped morphology of SnS₂ nanoflakes.

In Section 4.4.3., it was observed that the SnS₂ nanoflakes with the best performance had charge generation efficiency of 52%, charge transfer efficiency of 57% and charge separation efficiency of 95%. The charge generation efficiency is related to the amount of light absorption, hence the synthesis parameters growth time and source-substrate distance that control the height of SnS₂ nanoflakes can be attributed to this efficiency. Similarly, charge transfer efficiency is related to the presence of stepped edges which allow efficient charge transfer from SnS₂ to the electrolyte and this can be controlled using source-substrate distance, however, the low efficiency of 57% implies that these stepped edges also suffer from degradation. Finally, the high charge separation efficiency of 95% can be attributed to the vertical alignment of SnS₂ nanoflakes, which allows photoexcited charges to be transported efficiently from SnS₂ to the FTO or electrolyte interfaces. No single synthesis parameter can be associated with vertical orientation since the entire CSS was designed to grow vertical SnS₂ nanoflakes.

4.4.5. Investigation of Photoelectrochemical Stability

SnS₂ is known to be stable in ambient conditions and is free of surface oxides. However, it has relatively poor stability in aqueous solutions.^[24, 44] This is also evident in the chronoamperometric (CA) tests of our optimized SnS₂ nanoflake photoanodes (Figure 4-10a-b). Photocurrents from these photoanodes decrease significantly during the 10-min test in 1 M phosphate buffer, 1 M phosphate buffer + 1 M Na₂SO₃, and 1 M H₂SO₄ at a constant applied potential of 0.6 V_{RHE}. The photoanodes are also unstable in 0.5 M Na₂SO₄, as shown in CA tests performed at 1.23 V_{RHE} in Figure 4-10c.

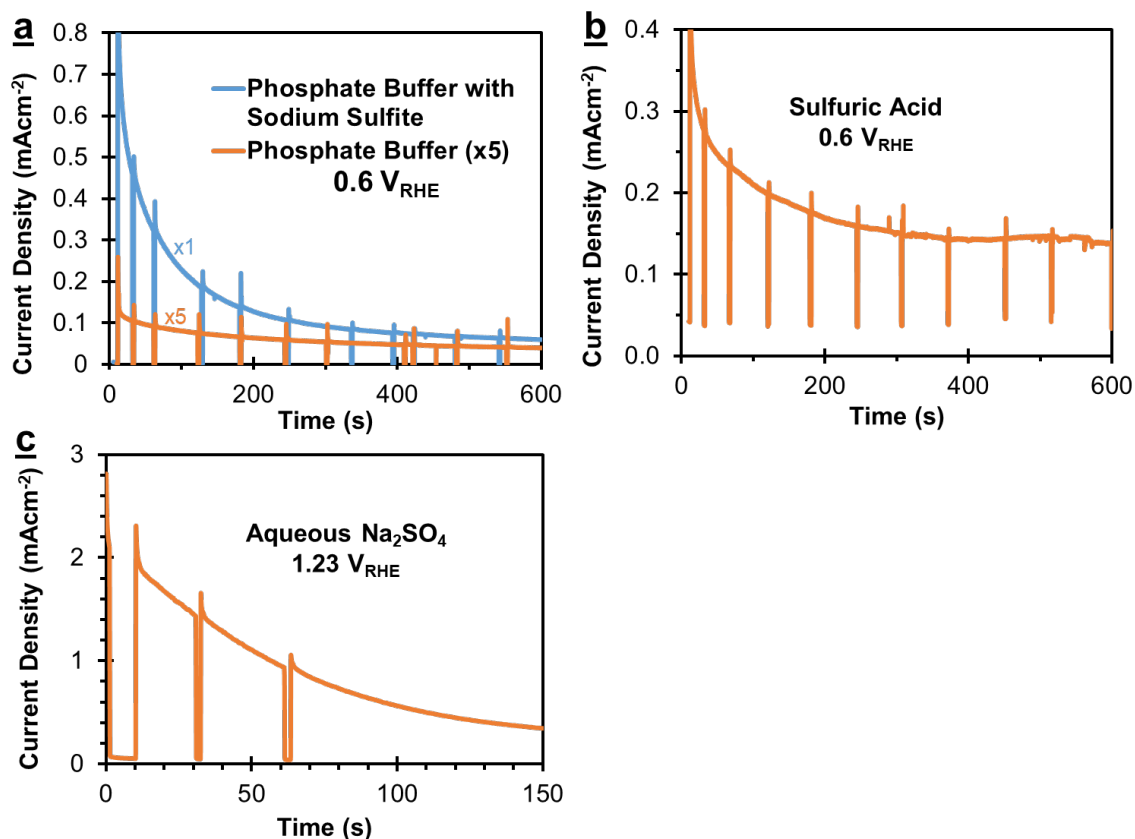


Figure 4-10. Chronoamperometric (CA) test with back illumination of vertical SnS₂ nanoflakes in (a) phosphate buffer with and without 1M Na₂SO₃ at 0.6 V_{RHE}, (b) 1M H₂SO₄ at 0.6 V_{RHE}, and (c) 0.5M Na₂SO₄ at 1.23 V_{RHE}. The incident light was blocked for 2 seconds periodically to determine the baseline for the dark current.

Controlled stability tests performed on CVT-grown single crystal SnS₂ (Figure 4-11a-e) suggest that the edges of SnS₂ are not only the active sites responsible for improving photocurrent but also the main sites of degradation. As shown in Figure 4-11a-c, while the pristine single crystal SnS₂ electrode (with minimal edges) shows no signs of degradation, the same SnS₂ transferred to ITO (with significantly more edges formed during mechanical exfoliation) shows significant loss of performance over time, implying that SnS₂ edges are responsible for degradation. This result is similar to reports on MoS₂, for which it has been proven that edges are preferentially oxidized in water.^[181] Due to the difference in area coverage of our single crystal and exfoliated SnS₂ samples, the values of the photocurrents could not be compared directly. Hence, another single crystal SnS₂ electrode was tested in KI + H₂SO₄ (in which SnS₂ was shown to be stable) with and without mild abrasion as shown in Figure 4-11d-e. The abrasion introduces steps and edges onto the otherwise flat single crystal SnS₂, which approximately doubles the photocurrent,

further supporting our claim that the steps and edges are responsible for increased photocurrent by behaving as electrochemically active sites. Even though the CVT-grown SnS_2 single crystals used here are not the same as our CSS-grown SnS_2 nanoflakes, the nature of the edges can be expected to be similar.

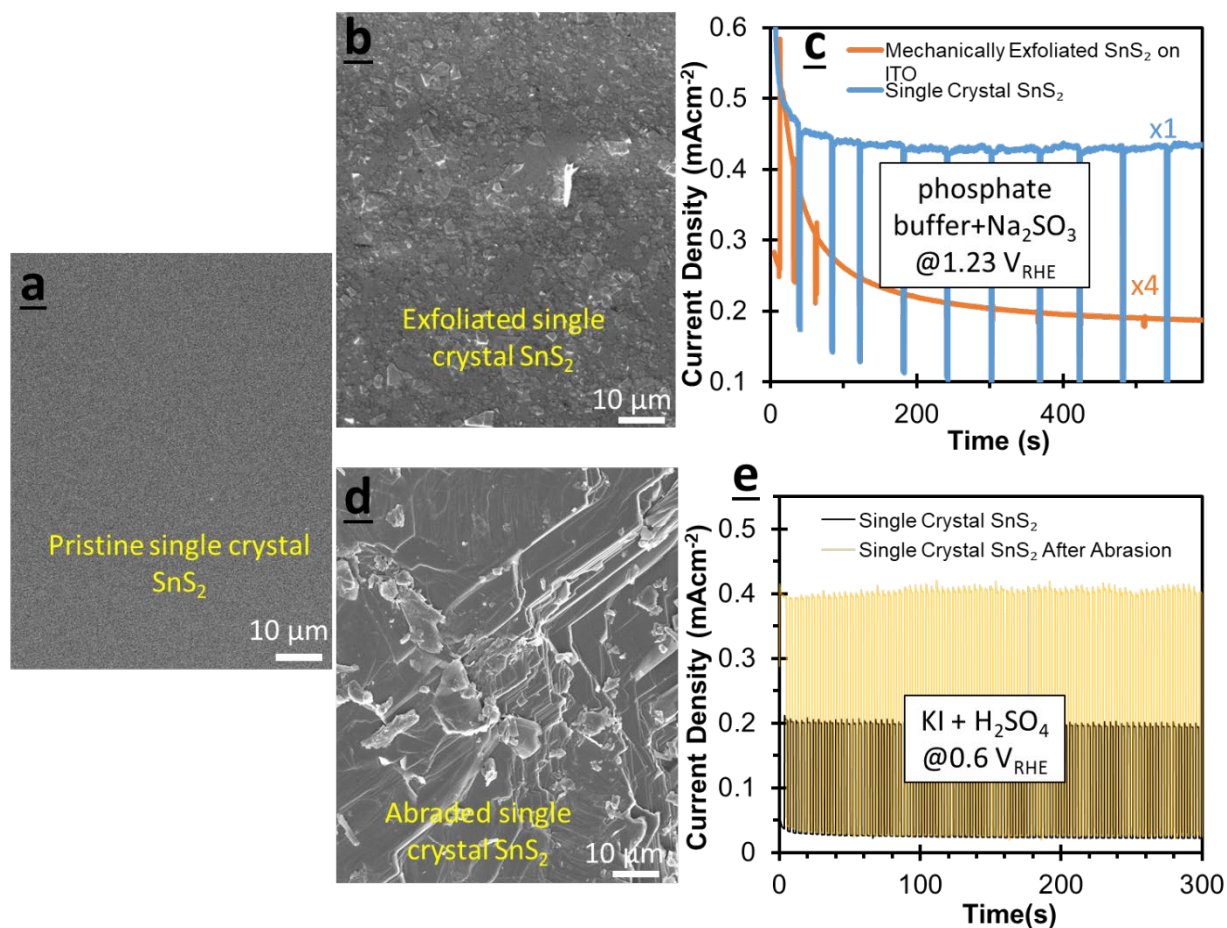


Figure 4-11. (a) SEM image of the pristine single crystal SnS_2 electrode prepared by directly bonding CVT-grown SnS_2 to nickel wire using silver glue; (b) SEM image of SnS_2 on ITO obtained by mechanically exfoliating single crystal SnS_2 from the same batch of CVT using thermal release tape (curing temperature 90°C) and transferring onto ITO; (c) Stability tests (without area correction) of single crystal (blue) and exfoliated (red) SnS_2 , performed in phosphate buffer with $1 \text{ M Na}_2\text{SO}_3$ at $1.23 \text{ V}_{\text{RHE}}$. (d) SEM image of the single crystal SnS_2 after mild abrasion, and (e) Comparison of the photocurrents of single crystal SnS_2 before and after abrasion at $0.6 \text{ V}_{\text{RHE}}$ in $0.1 \text{ M KI} + 1 \text{ M H}_2\text{SO}_4$ electrolyte.

In order to investigate the modes of degradation in our SnS_2 nanoflakes, XPS was carried out before and after PEC tests in phosphate buffer and sulfuric acid without any sacrificial agents. Compared to the as-grown SnS_2 nanoflakes (Figure 4-12a), those tested in sulfuric acid show

significant anodic dissolution (Figure 4-12b), evident from SEM images and XPS peak for elemental sulfur, which is one of the products of the dissolution reaction.^[24] This observation is further corroborated by ICP-OES (Inductively coupled plasma optical emission spectrometry) analysis (Table 4-1) that shows high concentration of Sn dissolved in the electrolyte. Similarly, the nanoflakes tested in phosphate buffer undergo surface oxidation (Figure 4-12c), which seems to slow anodic dissolution, as the nanoflakes appear more intact in the SEM images. All of these findings corroborate oxidation and dissolution of SnS₂ photoanodes observed by other researchers.^[24, 44]

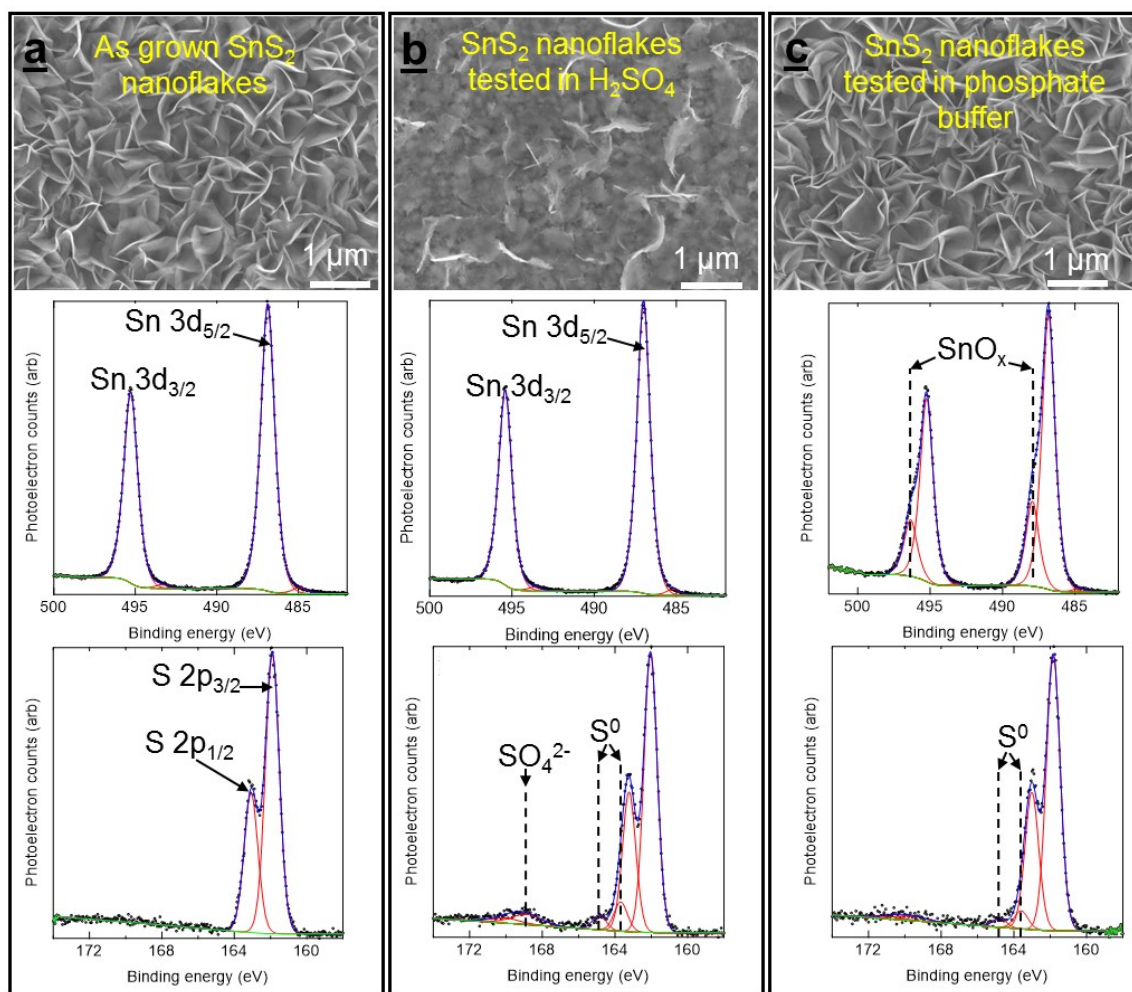


Figure 4-12. XPS comparison of vertical SnS₂ nanoflakes: (a) as-grown nanoflakes, (b) nanoflakes tested in 1 M H₂SO₄ and (c) nanoflakes tested in 1 M phosphate buffer. The 1st row shows the respective SEM images. The 2nd row corresponds to XPS signal from Sn 3d orbital while the 3rd row corresponds to that from S 2p orbital.

Table 4-1. ICP-OES results showing amount of Sn dissolved in the electrolyte after the test

	Concentration of dissolved Sn in the electrolyte [mgL^{-1}]
Phosphate buffer (pH7)	0.266
1 M H_2SO_4 (pH0.5)	4.345

In contrast, the SnS_2 nanoflakes showed substantially improved stability in the presence of iodide ions in the acidic electrolyte, which is consistent with a previous report.^[24] During both CA and LSV tests in 1 M H_2SO_4 + 0.1 M KI (Figure 4-13), our optimized SnS_2 nanoflakes showed no signs of degradation. Furthermore, the maximum stable photocurrent of 2.7 mAcm^{-2} was obtained at $0.6 \text{ V}_{\text{RHE}}$. In order to test longer-term stability in KI+ H_2SO_4 , a non-optimized SnS_2 nanoflake sample was used. As shown in Figure 4-14a-c, the SnS_2 nanoflakes maintain their photocurrent beyond 2 hours (after which the test was terminated), and their nanostructure is not affected by the test. This suggests that both dissolution and oxidation of SnS_2 are effectively suppressed by the fast kinetics of the iodide oxidation reaction. Due to relatively high photocurrent and photoelectrochemical stability, these SnS_2 nanoflakes can be utilized directly in applications such as iodine evolution, and dye-sensitized solar cells with iodide-triiodide redox couples. As for the photoelectrochemical water oxidation, suitable strategies need to be developed to protect the edges during prolonged use.

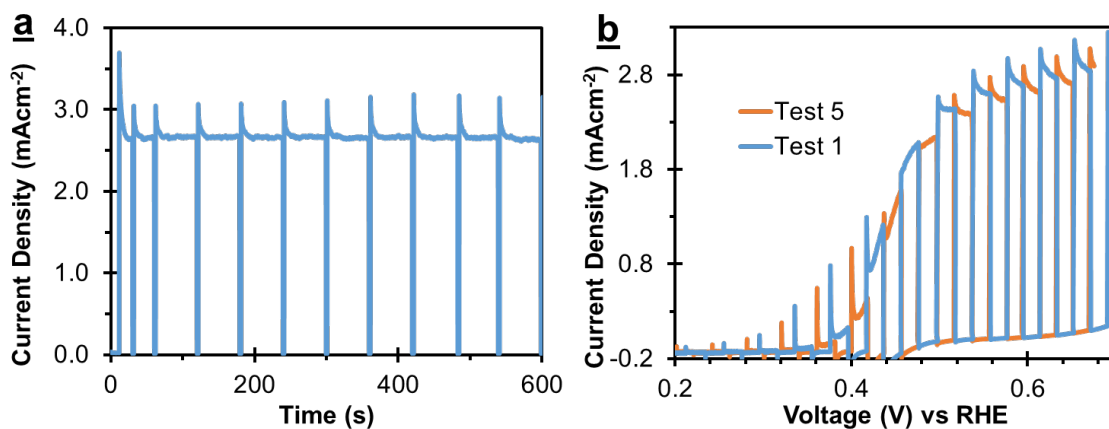


Figure 4-13. (a) Chronoamperometric test at $0.6 \text{ V}_{\text{RHE}}$; (b) The first and the fifth LSV tests of SnS_2 nanoflakes. Condition: 1 m H_2SO_4 + 0.1 m KI with light chopping and back illumination.

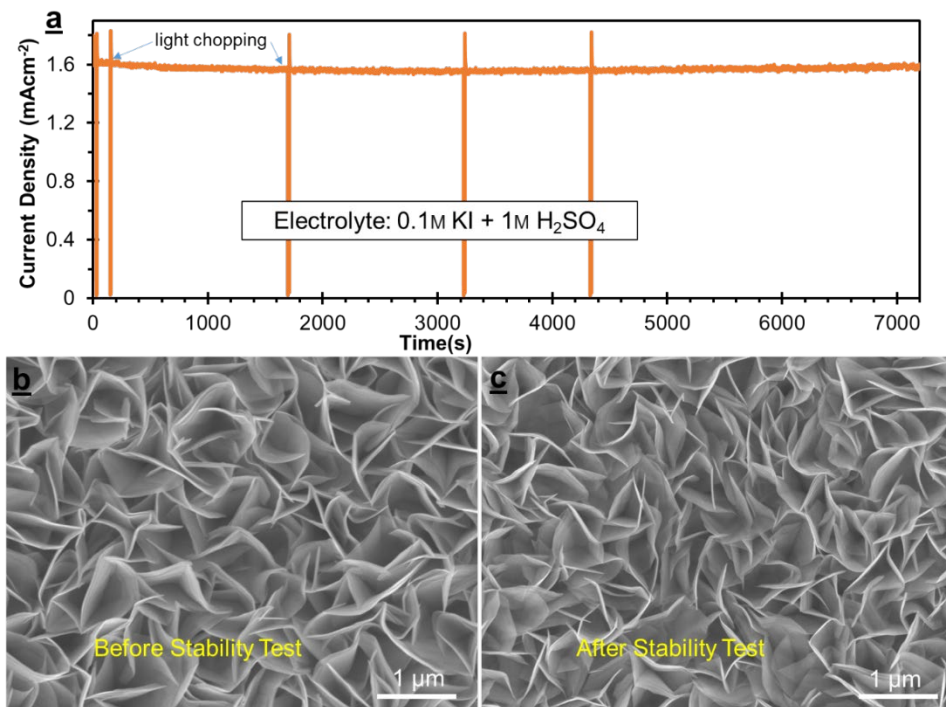


Figure 4-14. (a) Stability test of non-optimized SnS₂ nanoflakes for 2 hrs at 0.6 V_{RHE} in 1 m H₂SO₄ + 0.1 m KI with light chopping (total 5 times) and back illumination. SEM images of the nanoflakes (b) before and (c) after the stability test.

4.5. Conclusion

In summary, the growth of vertically aligned SnS₂ nanoflakes directly on FTO substrates has been optimized using a custom-designed close space sublimation system, and obtained nanoflakes with excellent optoelectronic and photoelectrochemical properties. The optimized SnS₂ nanoflakes exhibit high intrinsic carrier mobility (330 cm²V⁻¹s⁻¹) and long photoexcited carrier lifetimes (1.3 ns), which result in large diffusion lengths of ~1 μm. Photoanodes made of these nanoflakes yield photocurrents as high as 4.5 mAcm⁻² in aqueous phosphate buffer with 1 M Na₂SO₃ and 2.6 mAcm⁻² in aqueous 0.5 M Na₂SO₄, both at 1.23 V_{RHE} under simulated sunlight. They also produce stable photocurrents up to 2.7 mAcm⁻² at 0.6 V_{RHE} in the electrolyte containing 1 M H₂SO₄ and 0.1 M KI. Using various characterizations, and nanoparticle deposition, the origin of this high photocurrent is shown to be the combination of excellent optoelectronic properties, unique stepped morphology that exposes multiple edge sites in every nanoflake, and the optimized nanoflake height (~1.5 μm) that balances light absorption and charge transport. Out of these factors, the unique stepped morphology is believed to be the most

significant in yielding higher photocurrents than the CVD-grown SnS₂ nanoflakes. In addition, the vertical orientation is believed to be the most significant in producing higher photocurrents than exfoliated SnS₂. It is also understood that the thickness and packing density of the vertical nanoflakes need to be optimized, which can be addressed in the future. Through this work, a unique path to controlling the orientation and morphology of 2D SnS₂ nanoflakes for efficient solar energy conversion is highlighted.

Chapter 5: Enhancement of PbS Quantum Dot Photodetectors Using High Mobility SnS₂ Nanoflakes

5.1. Literature Review

5.1.1. Lead Sulfide Quantum Dots (PbS QDs) for Photodetection

One of the materials commonly used in photodetectors is lead sulfide (PbS) due to its high optical absorption and ease of synthesis. It is a relatively cheap material and its band gap can be easily tuned by controlling the diameter while forming quantum dots (QDs). This type of band gap tuning is advantageous because photodetectors with different specifications for multiple applications can be produced using the same material. In the case of PbS, band gaps ranging from 0.37eV (bulk) to 1.82eV (quantum dots) have been reported.^[182, 183] However, thin films photodetectors made from PbS quantum dots suffer from poor charge transport because the charges need to hop from one quantum dot to another before being collected. This lowers the effective mobility of charge carriers in PbS QD films to the range of 10^{-4} - 10^{-1} cm²/Vs, which results in low responsivity of the photodetectors.^[184-186] For applications that require high responsivity and fast response, other exotic semiconductors such as III-V InGaAs or HgCdTe systems with high manufacturing costs are used instead.^[187]

5.1.2. SnS₂ for Photodetection

Two-dimensional materials such as SnS₂, MoS₂, WS₂ and graphene with large mobility have emerged as promising alternatives to the expensive photodetector materials. They have the potential for achieving excellent performance at low cost.^[187] Tin disulfide (SnS₂) is one of those 2D materials that has been proven to have an outstanding mobility (18-760 cm²/Vs) and suitable bandgap of 2.1 eV relevant for photodetectors.^[15] It has a CdI₂-type layered crystal structure, hence, single or few layers of SnS₂ can be produced using top-down methods such as exfoliation as well as bottom-up methods such as chemical vapor deposition and epitaxial growth.^[29, 39, 188] Few researchers have demonstrated SnS₂ based photodetectors.^[29, 178, 189] These photodetectors have achieved maximum responsivities of 100 A/W^[29] and fast response times in the order of tens of milliseconds.^[39] Since these photodetectors use few layers of SnS₂ to obtain high mobility, they are often poor light absorbers and their spectral range is limited to ultraviolet and visible wavelengths due to the large band gap of SnS₂. If a broader range of detection is desired,

other materials such as lead sulfide quantum dots (PbS QDs) with tunable band gaps can be combined with SnS₂.

5.1.3. SnS₂/PbS QDs Heterostructure for Photodetection

A strategy that has been proven to improve photodetector performance even further is to form a heterostructure consisting of few layers of SnS₂ sensitized by PbS QDs.^[98, 106] The resulting device combines the high optical absorption of PbS QDs with the high mobility of SnS₂, and exhibits excellent responsivity and response times. In addition, the heterostructure has the tunability of PbS QDs and broader range of detection than SnS₂-only devices. Due to fast charge transport in its basal planes, SnS₂ can provide high-mobility pathways for the photogenerated charges injected from PbS quantum dots to be transported efficiently between the contacts. Such a device has been shown to achieve responsivities in the order of 10⁵ AW⁻¹, which is greater than 10² AW⁻¹ obtained from single-layer SnS₂ phototransistors as well as 10³ AW⁻¹ obtained from PbS quantum dot photodetectors.^[29, 190]

Despite the excellent figures of merit of the photodetectors based on SnS₂/PbS QD heterostructure, none of the existing reports have sufficiently demonstrated scalability of SnS₂ fabrication. Instead, they have focused on either mechanically exfoliating SnS₂ to few layers or growing few layer SnS₂ sparsely on a substrate using chemical vapor deposition (CVD). Both of these approaches lead to unpredictable distribution of SnS₂ flakes on the substrate requiring expensive alignment equipment for depositing contacts on each photodetector. This undoubtedly makes it hard to form an array of detectors needed for various applications such as cameras and digital displays. Hence, there is a need for a more scalable method with higher yield and easier fabrication while not compromising sensitivity, photogain, response time and on-off ratio.

In this work, heterostructure photodetectors based on SnS₂ nanoflakes and PbS QDs were fabricated using only scalable synthesis methods. The SnS₂ nanoflakes were synthesized using scalable close space sublimation method on SiO₂/Si substrates with pre-patterned metal contacts, and PbS QDs were coated onto these nanoflakes by drop casting. To the best of our knowledge, this is the first report in which heterostructure photodetectors made of SnS₂ nanoflakes and PbS quantum dots have been realized. These photodetectors exhibit responsivities of 2 orders of magnitude higher than that of devices based on PbS QDs only or SnS₂ only.

5.2. Objectives

The main objectives of this project were as following:

- To fabricate heterostructure photodetectors made of SnS₂ nanoflakes and PbS QDs using only scalable methods
- To investigate the photoconductivity mechanism and the origin of enhanced performance of the heterostructure photodetectors
- To provide a better understanding of the role played by the amount of PbS QDs in determining the overall characteristics of the heterostructure photodetector

5.3. Experimental Methods

5.3.1. Photolithography of Gold Contacts

SnS₂/PbS photodetectors were fabricated using only scalable methods. The first step involved making gold contacts on SiO₂/Si substrate. This specific substrate was chosen to demonstrate that these photodetectors are compatible with silicon optoelectronics. The 300nm SiO₂ layer was formed by wet oxidation and rest of the silicon was highly p-doped (resistivity 0.001-0.005 Ωcm) to allow application of gate voltage to the photodetector channel, although gate voltages were not applied in this project.

The gold contacts with 20 μm gaps and 5 mm wide were made using conventional contact photolithography. The steps involved in the process are shown in Figure 5-1. The negative photoresist known as SU-8 was first spin coated onto a SiO₂/Si wafer. Then the photoresist was exposed to ultraviolet (UV) light through a mask. The photoresist that was not exposed was dissolved during developing stage, yielding trenches, which were then filled with thermally evaporated Au. Finally, the remaining SU-8 was dissolved or peeled away with the help of acetone. Additional details on this photolithography process can be found in Appendix A.

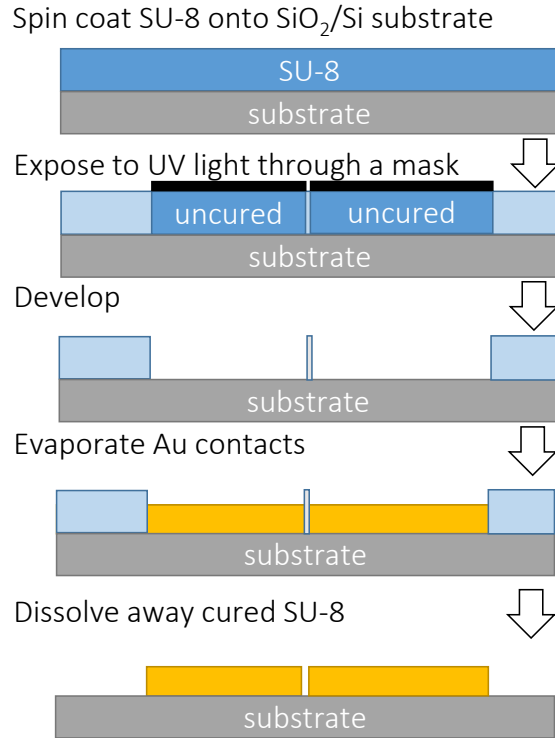


Figure 5-1. Photolithography steps used to make Au contacts on SiO₂/Si substrates

5.3.2. Growth of SnS₂ Nanoflakes

The second step is the growth of SnS₂ nanoflakes in the photodetector channel defined by the Au contacts. For this, the same close space sublimation setup described in Chapter 3 was used (Figure 5-2). The SiO₂/Si substrate with the Au patterns was mounted onto the substrate holder and placed in the vacuum chamber. Source temperature (T_{src}), substrate temperature (T_{sub}) and source-substrate separation (d_{ss}), were 525 °C, 430 °C and 10 mm respectively. The growth was carried out for 2min for short samples and 5min for tall samples.

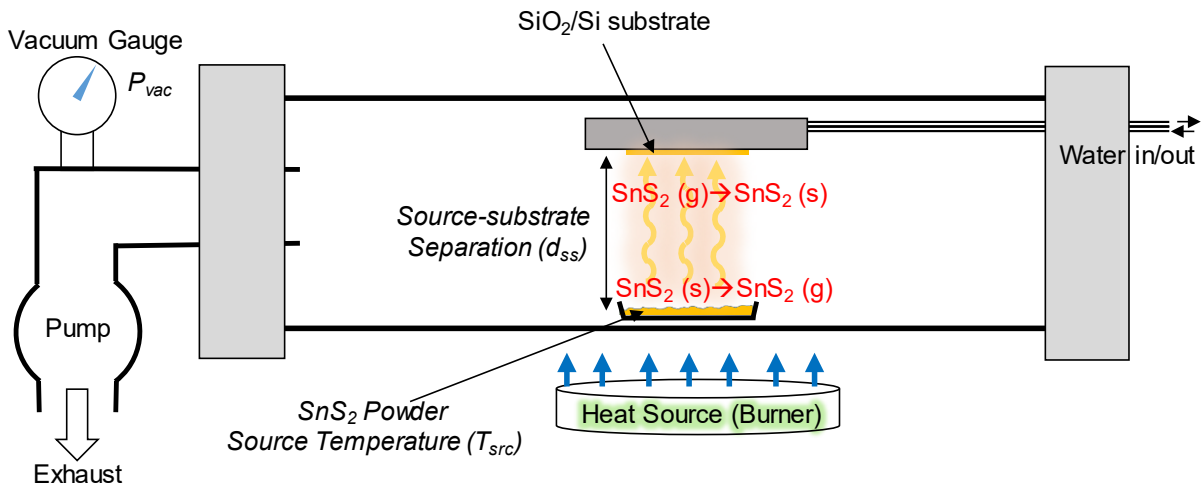


Figure 5-2. Close space sublimation setup used to grow SnS₂ nanoflakes (from Chapter 3)

5.3.3. Drop Casting of PbS QDs onto SnS₂ Nanoflakes

10mg/ml PbS QDs in toluene with emission wavelength of 900nm were bought from Sigma Aldrich (Part No. 900733). The QD suspension was further diluted to 5mg/ml with anhydrous toluene also purchased from Sigma Aldrich (Part No. 244511). 2% ethanedithiol (EDT) was prepared by adding 20ul EDT (Sigma Aldrich, Part No. 02390) in 1ml of anhydrous acetonitrile (Sigma Aldrich, Part No. 271004).

The PbS QDs were coated onto SnS₂ nanoflakes using a layer by layer (LBL) method. Several layers of PbS QDs (up to 30 layers) were coated on some samples to obtain various thicknesses of PbS QDs film. The as-purchased PbS QDs were capped using oleic acid ligands, which are long chain molecules used to extend the shelf life of quantum dots but are insulating for making thin films. The use of layer by layer method allowed the exchange of these long oleic acid ligands with shorter ethanedithiol ligands, which improved charge transfer between QDs. The steps involved in each layer of PbS QDs are illustrated in Appendix A, Table A-1.

5.3.4. Optoelectronic Characterization

A simple driver circuit was constructed to control the illumination of the photodetectors (Figure 5-3). Two LEDs (Thorlabs, Part no. LED525L and LED780E) of wavelengths 525 nm and 780 nm were used because 525nm light is absorbed by both SnS₂ and PbS QDs whereas the 780nm light is only absorbed by PbS QDs. A function generator was used to control the frequency and

duty cycle of the pulses sent to the LED. The LED power was varied by changing V_{cc} while keeping the current lower than the maximum forward current of the LED.

The photodetector was connected to the potentiostat or a LabVIEW data acquisition system that applied appropriate bias voltage while measuring the current in the order of nanoamperes.

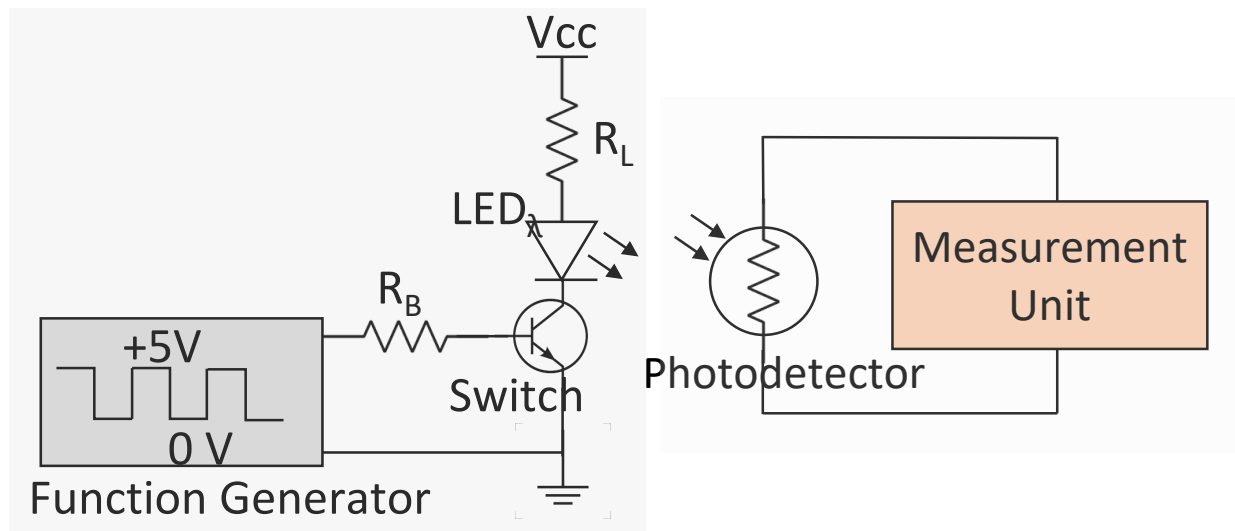


Figure 5-3. The measurement system used to characterize the performance of SnS_2/PbS QDs photodetectors

Frequency response of the photodetectors was obtained by using Stanford Research Systems lock-in amplifier (Model no. SR830) with the reference input connected to the same waveform that is also driving the LED circuit.

5.4. Results and Discussion

5.4.1. SnS_2 Photodetector

SnS_2 photodetectors without any PbS QDs were first fabricated on SiO_2/Si to prove that the SnS_2 nanoflakes were indeed connected to each other and could make a photoconducting channel on their own. It was observed that simply varying growth duration was enough to control the properties of the SnS_2 channel. With longer growth times, longer nanoflakes with larger dark current and larger photocurrent were obtained. This was because dark conductivity and light absorption are directly related to the thickness of the channel. In order to keep the dark current to a minimum, the two types of SnS_2 with growth times of 2 and 5 min were chosen and compared.

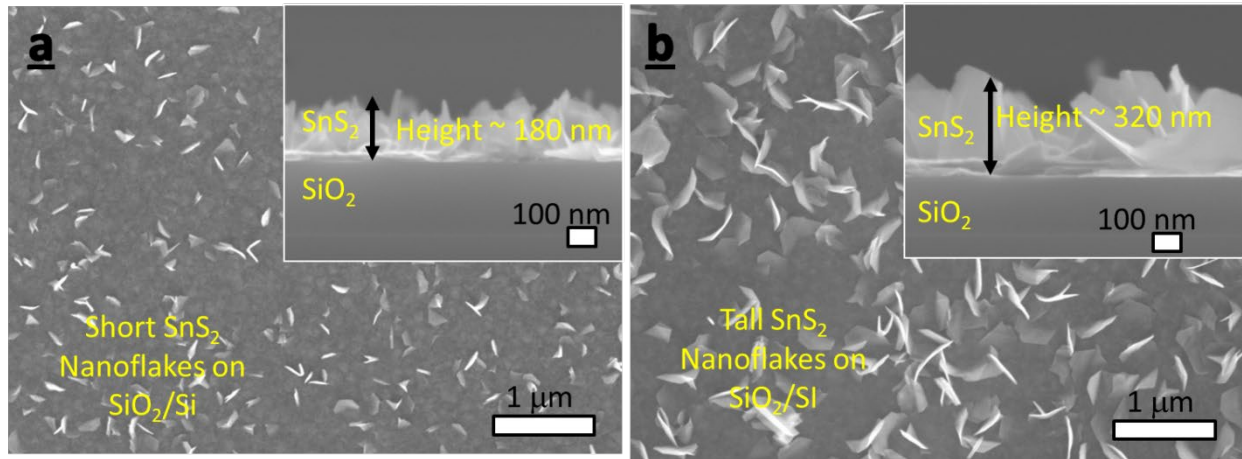


Figure 5-4. SEM images of (a) short SnS₂ nanoflakes grown for 2 min, and (b) tall SnS₂ nanoflakes grown for 5 min on SiO₂/Si substrates

As shown in Figure 5-4, the SnS₂ thin film consists of horizontal layers as well as vertical nanoflakes, consistent with the growth mechanism discussed in Chapter 3. The cross section SEM images in the insets show that the short and tall SnS₂ nanoflakes have a height of about 180nm and 320nm respectively. It can also be seen that the thickness of horizontal layers is greater in the case of tall SnS₂ sample than in the short SnS₂ sample, which is consistent with the I-V characteristics of photodetectors based on these samples (Figure 5-5a).

Given that the work function of SnS₂ and Au are ~4.6 eV and ~5.1 eV respectively, the SnS₂/Au junction is expected to be Schottky.^[98] However, in the -10 to 10V bias range, the Schottky behavior of this junction is not obvious in the I-V characteristics. This could mean that the SnS₂/Au junction is only slightly Schottky, and the barrier height may be lower than other reported cases due to excellent contact between SnS₂ and Au formed during the synthesis. A layer of Ti metal is often used to improve adhesion of top Au contacts; however, it was not necessary in this case due to annealing of the bottom Au contacts during SnS₂ growth by CSS.

As expected, both tall and short SnS₂ nanoflakes absorb 525nm light, and produce photocurrents of ~4 nA and ~0.5 nA respectively with 5V bias (Figure 5-5b). Another important observation is that the tall SnS₂ device has more noise than the short SnS₂ one, consistent with other reports in the literature that multi-grain photodetectors have higher noise level.^[191-193] A thorough noise spectrum analysis is required to further solidify this observation in our photodetectors.

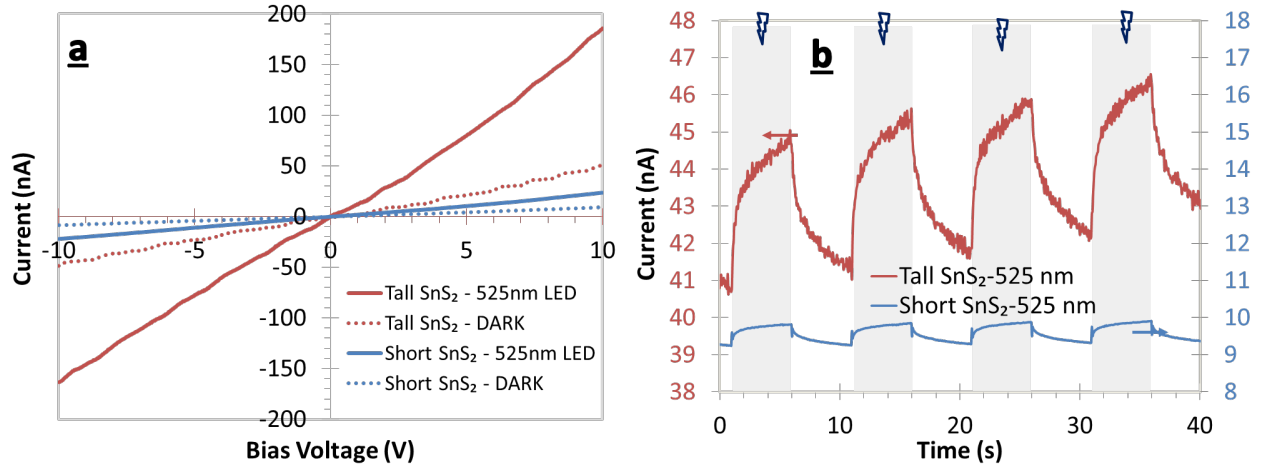


Figure 5-5. (a) I-V characteristics of SnS₂ photodetectors and (b) transient photoresponse with pulsed 525 nm LED, 155 $\mu\text{W}/\text{cm}^2$ and 5V bias

The transient current measurement of the SnS₂ photodetectors also shows that the response time is in the order of several seconds. This is similar to the response times of other 2D metal dichalcogenides in the literature.^[110, 194-197] In some cases, the slow response time in SnS₂ has been attributed to the long-lived charge trapping processes in atmospheric adsorbates such as water and oxygen molecules that bind to the surface of SnS₂ and withdraw electrons from the channel.^[196] This was verified in our own experiment where an un-encapsulated photodetector in vacuum showed superior photocurrent and response time to that tested in ambient air (Figure 5-6). It can also be observed that the dark current of the photodetector increases in vacuum, which is due to the lack of atmospheric adsorbates that remove electrons from the channel. In order to promote desorption of the adsorbates, the device was illuminated with 300 Watt Xenon lamp for 30 minutes under vacuum. When the device was brought back to the ambient atmosphere, the photoresponse returned to the original, implying reversibility of the atmospheric adsorbates.

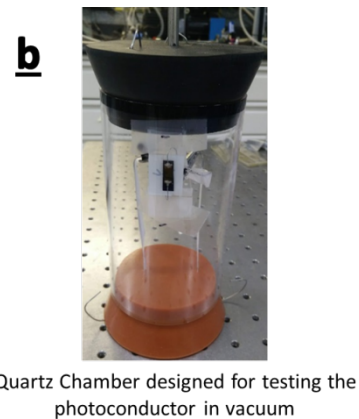
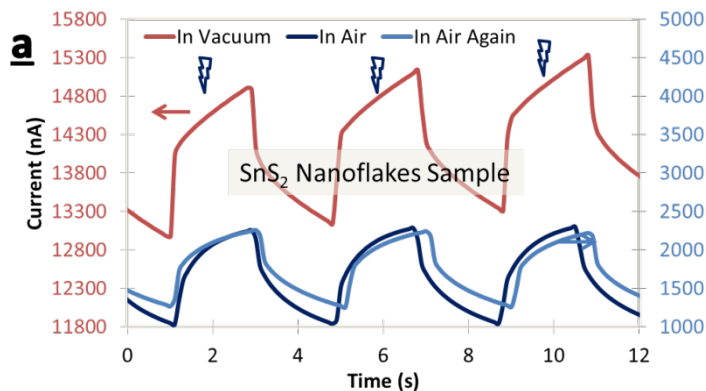


Figure 5-6. (a) Transient current measurements of SnS₂ photodetector under Xenon Lamp (100 mW/cm²) performed in air followed by vacuum, which is then followed by air again. Bias voltage = 5V. The image in (b) is a photo of the quartz chamber used to test the devices in vacuum

Even though pure SnS₂ nanoflakes would not absorb 780 nm light, our SnS₂ photodetectors do weakly absorb that wavelength indicating the presence of some defects. The I-V and transient characterization of tall and short SnS₂ nanoflake photodetectors in 780 nm light is shown in Figure 5-7.

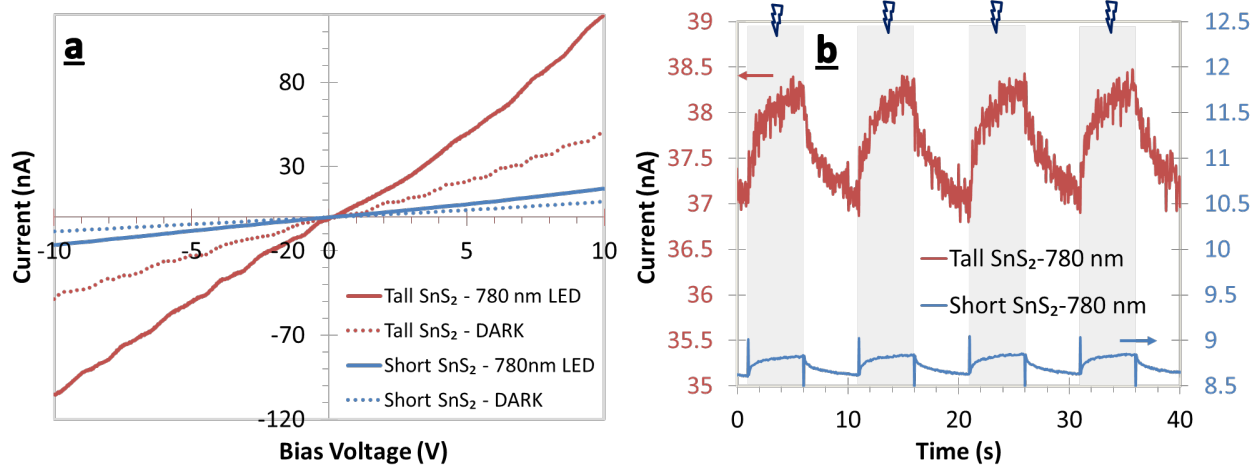


Figure 5-7. (a) I-V characteristics of the SnS₂ photodetector and (b) its transient photoresponse with pulsed 780 nm LED, 350 μW/cm² and 5V bias

Since the photocurrent of a photodetector is dependent on the amount of light, a better measure of the performance of a photodetector is responsivity. Responsivity is calculated by dividing the photocurrent by incident light power. Figure 5-8 shows both photocurrent and responsivity of

SnS₂ only devices illuminated by 525nm and 780nm LED. The responsivity with 780nm light is about 10 times lower than that with 525nm light due to weak absorption.

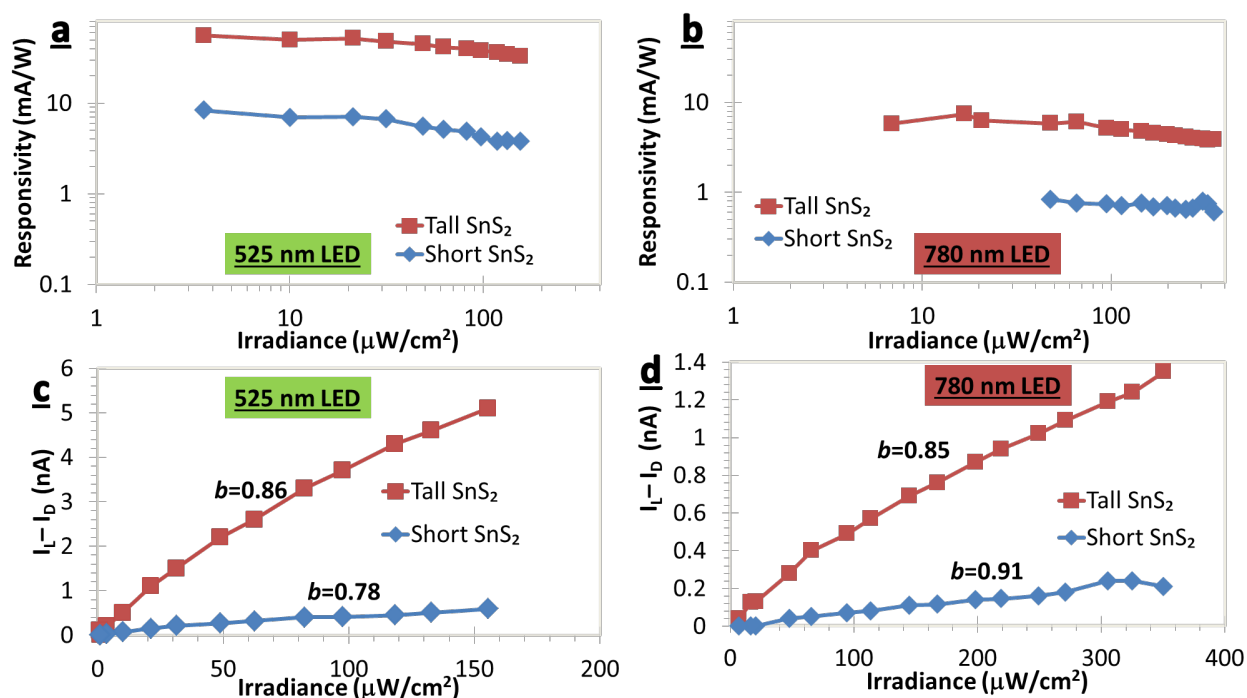


Figure 5-8. Responsivity (a and b) and Photocurrent (c and d) of SnS₂ photodetectors illuminated with 525nm (a and c) and 780nm LED (b and d)

In general, the responsivity of photodetectors decreases with increasing light intensity due to saturation of sensitizing traps that contribute to the photogain.^[98] In MoS₂ photodetectors, it has also been reported that accelerated bimolecular/radiative recombination between free holes and electrons under high-power illumination lowers the responsivity of the device.^[106, 198, 199]

The nonlinear relationship between light intensity (P) and photocurrent (I_{ph}) can be captured by the power law $I_{ph} = a \cdot P^b$. In our SnS₂ photodetectors, the b parameter is less than 1, indicating the presence of trap mediated recombination of the photoexcited carriers.^[200]

Influence of Synthesis Parameters on SnS₂ Photodetector

In order to synthesize SnS₂ nanoflakes for photodetector application, the growth using CSS had to be modified slightly. The first modification was in the growth duration. In general, longer growth durations led to a thick horizontal layer of SnS₂ as well as taller nanoflakes. Consequently, the photodetectors based on this SnS₂ had large dark currents as well as large

photocurrents, resulting in low on-off ratios. In addition, the response times of these photodetectors were in the order of several tens of seconds, which is undesirable. The tall nanoflakes in photodetectors also tend to increase the noise level, which results in small signal-to-noise ratios. Hence, the growth durations were limited to 2 and 5 min for SnS₂ nanoflakes based photodetectors.

The source-substrate distance in these syntheses was kept at 10mm as it was easier to keep the substrate at the high vapor concentration region. In general, the growth rate of SnS₂ on SiO₂ was lower than that on FTO due to the relatively flat surface and lack of favorable nucleation sites. Having the substrate close to the source as well as defining a deposition window on the SiO₂ substrate using aluminum foil helped make the growth more efficient.

Unlike in the case of SnS₂ nanoflakes on FTO, the horizontal growth on SiO₂ ensured good connection between the SnS₂ nanoflakes and determined the mobility of the channel. Similarly, vertical growth ensured that more light was absorbed. However, the nanoflake structure was also the reason for slow response as the photoexcited charges were too far from the high-drift region between the gold contacts. In other words, nanoflake morphology was responsible for not only high responsivity but also slow speed of photodetectors.

5.4.2. PbS QDs Photodetector

Before fabricating SnS₂/PbS heterostructure photodetectors, devices were made using only PbS QDs for comparison. The layer by layer method described in the Experimental Methods section was used to form a thick film of PbS QDs on Au contacts with 40μm channel length. At the rate of ~5.5nm per layer, the thin film obtained after 30 layers of PbS QDs was about 170 nm thick (Figure 5-9). The performance of the PbS QDs based photodetectors is discussed in the next section.

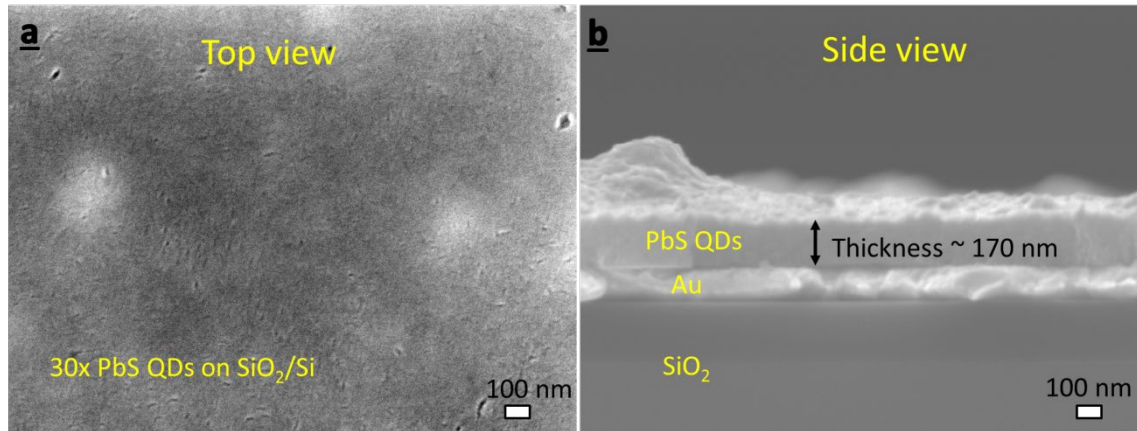


Figure 5-9. (a) Top and (b) side view SEM images of photodetectors made of 30 layers of PbS QDs on SiO₂/Si. The image in (b) shows the region where Au makes contact with the PbS QDs film

5.4.3. SnS₂ Nanoflakes/PbS QDs Heterostructure Photodetector

PbS QDs were coated onto SnS₂ nanoflakes using the layer by layer method described above. Two types of SnS₂ samples (i.e. short and tall) were used to form the channel. According to Figure 5-10, both the short and tall nanoflakes are completely coated in PbS QDs and also form a continuous film of PbS QDs at the bottom. However, the main channel is formed by SnS₂ because it is in direct contact with the Au while the PbS film is not. Some researchers have pointed out that even when Au contacts touch both SnS₂ and PbS films, the main channel for conduction would still be formed by SnS₂ because the mobility of SnS₂ is a few orders of magnitude higher than that of the PbS QDs.^[106] According to Carey et. al., the mobility of PbS QDs similar to the ones used in this work was in the range of 10^{-4} to 10^{-1} cm²/Vs.^[184-186] In contrast, the Hall effect mobility of SnS₂ nanoflake thin film synthesized in this project was measured to be ~ 2 cm²/Vs, which is at least an order of magnitude higher than that of PbS QDs. It should be noted that this Hall effect mobility underestimates the intrinsic mobility measured in Chapter 4 by TRTS. This is because this measurement was carried out with Van der Pauw method where the metal contacts were ~ 8 mm apart. Consequently, the undesirable effect of grain boundaries was included in the measurement.

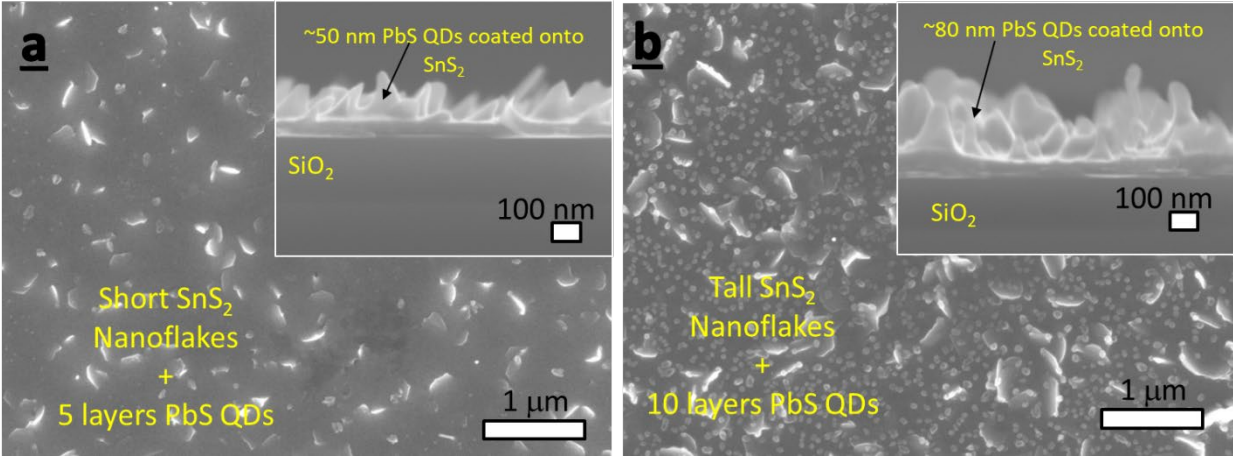


Figure 5-10. SEM images of PbS QDs coated (a) short nanoflakes and (b) tall nanoflakes used to make the photodetector. The insets show the cross-section SEM of the device consisting of

In order to understand the role of SnS₂ in the SnS₂/PbS heterostructure, 10 layers of PbS QDs were coated onto tall SnS₂ and compared to devices made of only PbS QDs. Figure 5-11 shows that while SnS₂/PbS heterostructure devices have higher dark currents, they also have much higher photocurrents. Furthermore, PbS QDs make ohmic contact with Au, which is also evident from the linear I-V curve in Figure 5-11b.

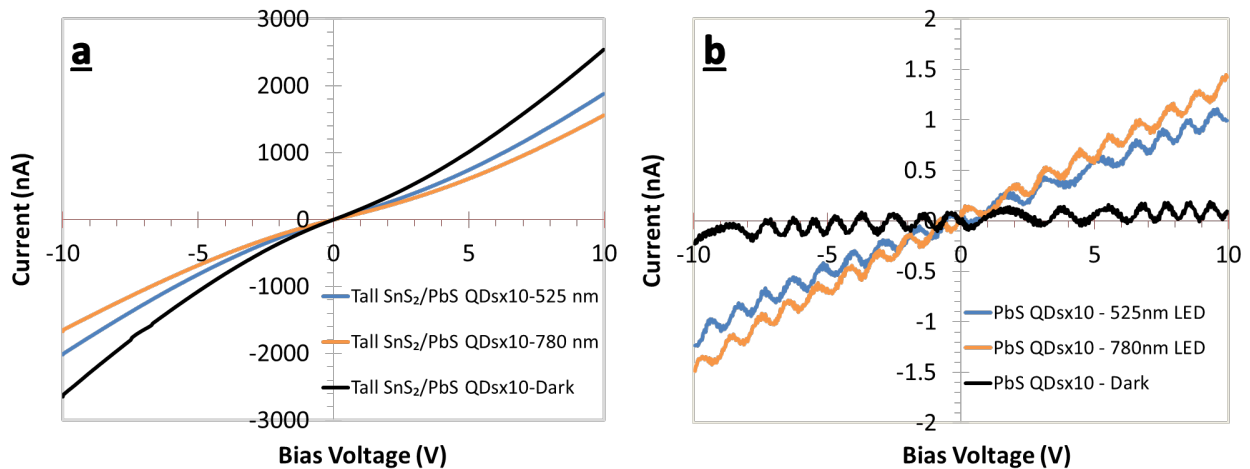


Figure 5-11. I-V characterization of (a) tall SnS₂/PbS QDs heterostructure photodetector and (b) PbS QDs photodetector. The intensity of 525nm and 780nm light were 155 μW/cm² and 350 μW/cm² respectively. The wavy pattern of the I-V curve in (b) was due to the inadequate bandwidth of the potentiostat used for the measurement.

Figure 5-12 shows the responsivity of the two types of SnS₂/PbS heterostructures along with PbS-only devices at various light intensities. As discussed earlier, the highest responsivity of

these devices is obtained at the lowest light intensity. It can be discerned from the figure that the responsivity of tall SnS₂/PbS QDs device is about 2 orders of magnitude higher than that of PbS QDs only device at the same illumination power. With 3.6 μW/cm² 525nm light, bare tall SnS₂ device yielded responsivity of 0.055 A/W and PbS only device yielded responsivity of 0.013 A/W. However, their heterostructure device yielded the responsivity of 3.05 A/W, which is much higher than either of the materials on their own. This is a clear demonstration of the synergistic effect of high mobility SnS₂ and excellent light absorber PbS QDs in photodetectors.

The same trend of responsivity versus irradiance can be seen with 780nm light in Figure 5-12b.

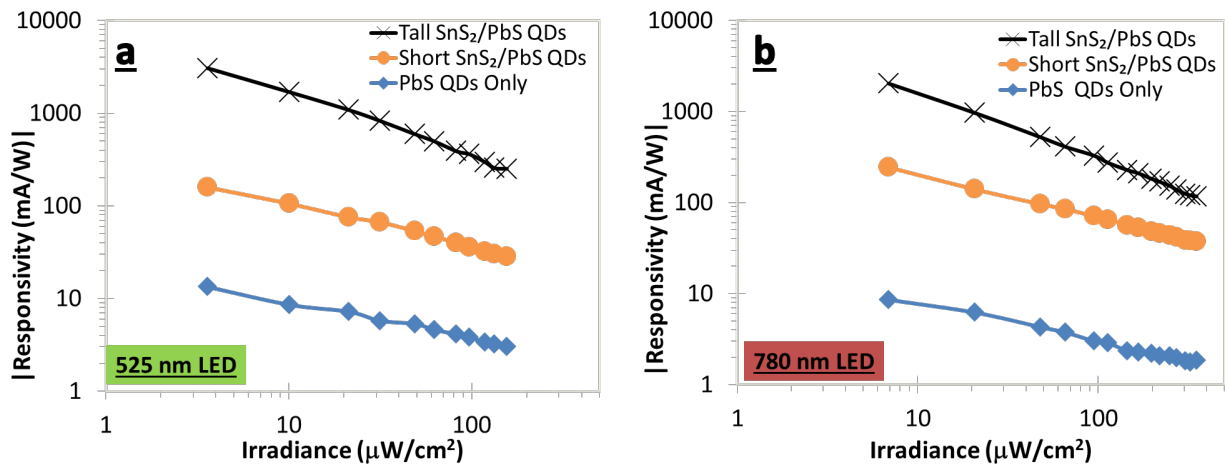


Figure 5-12. Absolute responsivities of three types of devices with 10 layers of PbS QDs as a function of irradiance levels of (a) 525nm and (b) 780nm light. The chopping frequency was set to 0.1Hz and bias voltage was 5V.

In terms of external quantum efficiency, the trend is similar because external quantum efficiency (*EQE*) is proportional to responsivity (*R*), and is given by the relationship, $EQE = \frac{h\nu}{e} * R$, where *h* is Planck's constant, *ν* is frequency of LED light and *e* is elementary charge.^[200] The highest EQE of 721 % was obtained with tall SnS₂ coated with 10 layers of PbS QDs at the lowest illumination of 3.6 μW/cm² 525nm light (Figure 5-13). Since the intensity of absorbed light is always equal to or less than that of incident light (i.e. IQE ≥ EQE), this corresponds to IQE of at least 721%. Similarly, since photogain follows the definition of IQE, this corresponds to gain of at least 7.2.

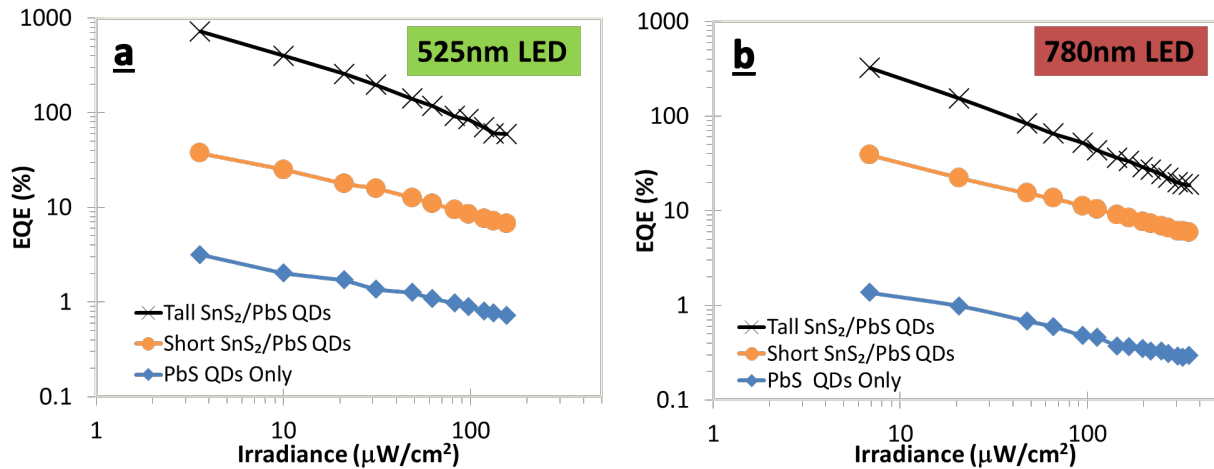


Figure 5-13. External quantum efficiency of three types of devices with 10 layers of PbS QDs as a function of irradiance levels of (a) 525nm and (b) 780nm light. The chopping frequency was set to 0.1Hz and bias voltage=5V.

In comparing the performance of tall SnS₂/PbS with PbS only devices, it is important to ensure that the light absorption by the devices is not influencing the conclusion. Since the illumination area of a photodetector is only 40 μm x 5mm, separate larger samples were made on a glass substrate to measure the absorption profile using an integrating sphere. As shown in Figure 5-14, the light harvesting efficiency (LHE) of 10 layers of PbS QDs is similar to that of tall SnS₂ with 10 layers of PbS QDs at both 525 nm and 780nm. Any small difference due to measurement uncertainty is not likely to produce 2 orders of magnitude difference in responsivity. This suggests that the responsivity enhancement in the heterostructure photodetectors is not due to improved light absorption.

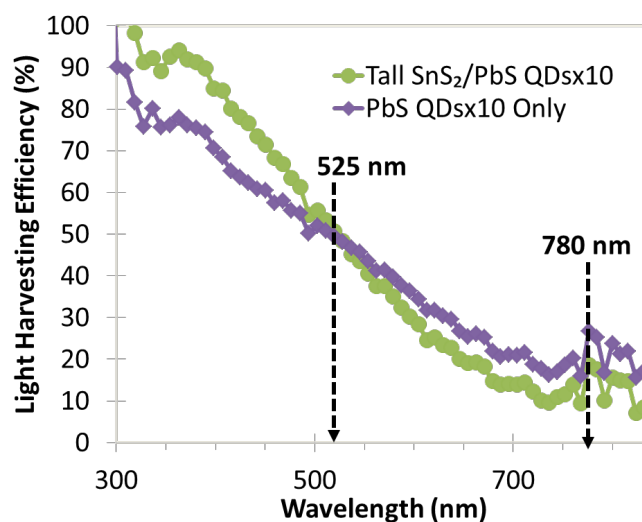


Figure 5-14. Light harvesting efficiency of photodetectors with only 10 layers PbS QDs compared to that of tall SnS₂ nanoflakes with 10 layers of PbS QDs

5.4.4. Negative Photoconductivity

One unusual aspect of tall SnS₂/PbS QDs photodetectors in our project is that the current decreases with light exposure (Figure 5-15). This is unlike the behavior of SnS₂ only or PbS only devices and is referred to as negative photoconductivity (NPC). Even with negative photoconductivity, magnitude of the photocurrent obtained from the heterostructure devices is much larger than that from the PbS QDs only or SnS₂ only devices. Furthermore, the photoconductivity seems to stay negative for both 525nm and 780nm LED. Another important observation is that the fall time (LED-on) is smaller than the rise time (LED-off) implying that two separate phenomena may be responsible for this behavior, which will be discussed in the next section.

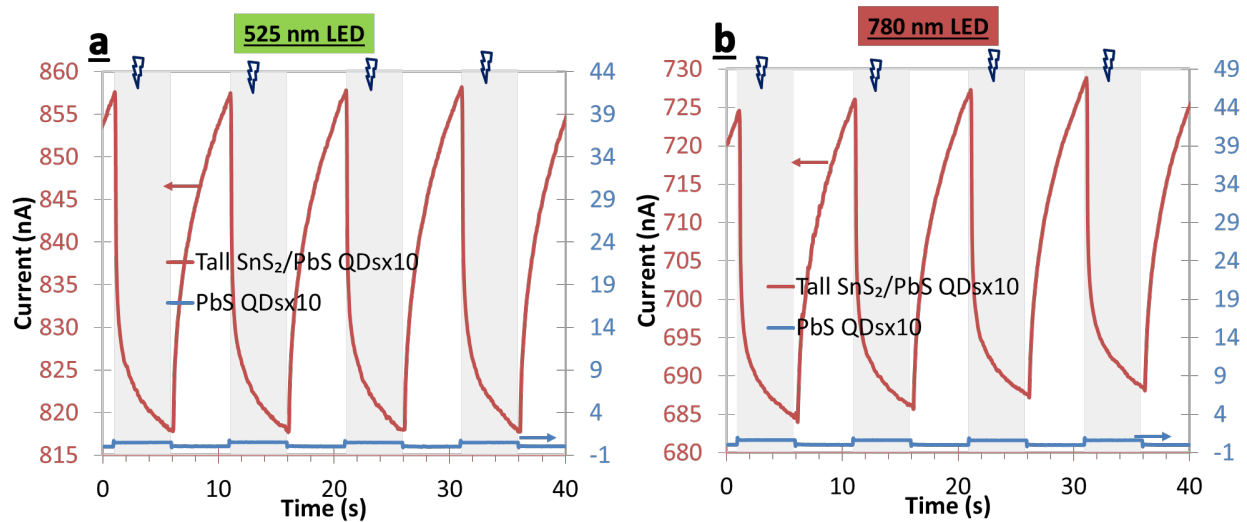


Figure 5-15. Transient current measurement of a photodetector made of tall SnS₂ with 10 layers of PbS QDs compared to that of a photodetector made of only 10 layers of PbS QDs, illuminated with (a) 525nm LED ($155\mu\text{W}/\text{cm}^2$) and (b) 780nm LED ($350\mu\text{W}/\text{cm}^2$)

The origin of NPC is often very difficult to understand and it almost always involves the interaction of multiple factors. In this project, tall SnS₂/PbS QDs exhibit NPC but short SnS₂/PbS QDs exhibit positive photoconductivity (PPC), which makes it even harder to identify the mechanism.

There have been a few cases of NPC reported in the literature. In one case, the NPC in MoS₂/PbS photodetectors was believed to be due to photo-induced changes in mobility caused by increased charge scattering by the positive photo-charged PbS QDs.^[106] This mechanism was verified by

sweeping gate voltages and measuring field effect mobility in a phototransistor configuration under illumination. In another case, Han et.al. attributed NPC in their InAs nanowires to gas adsorption and photogating by native oxide layer on the surface.^[201] In order to test if the atmospheric molecules were responsible for NPC in our devices, a layer of polymethyl methacrylate (PMMA) was spin coated on top of SnS₂/PbS QDs. This method was suggested by a previous study as PMMA encapsulation can suppress the effects of atmospheric molecules.^[202] However, this did not change the nature of the photocurrent in our heterostructures (Figure 5-16). The magnitude of the photocurrent was decreased with PMMA coating due to decreased light absorption; however, the negative photoconductivity was prevalent with both 525nm and 780nm light.

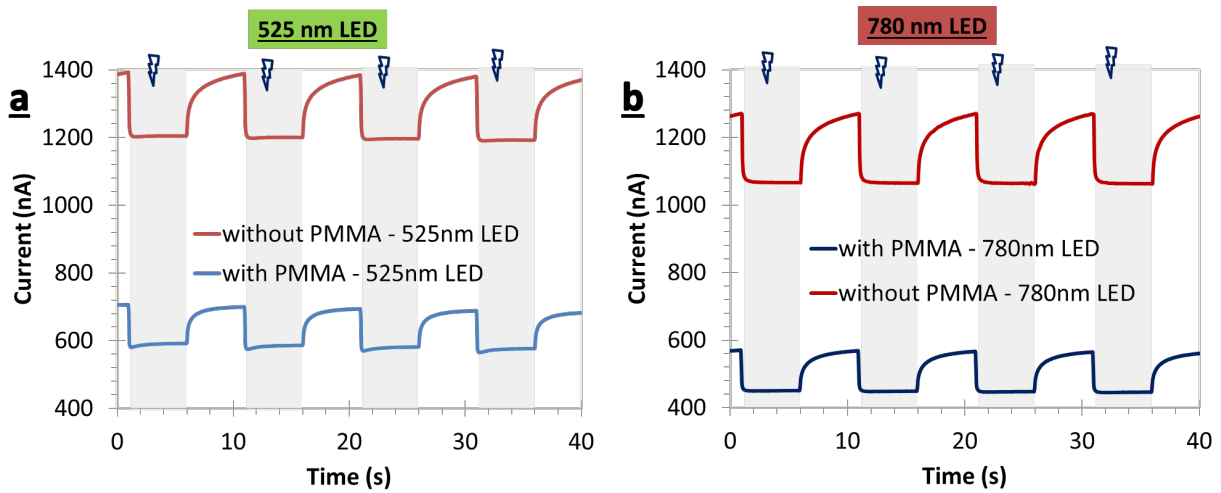


Figure 5-16. Transient current response of photodetectors with tall SnS₂ and 10 layers of PbS QDs obtained under (a) 525nm and (b) 780nm light before and after PMMA encapsulation

5.4.5. Photoconductivity Mechanism

A possible photoconduction mechanism is proposed based on the results so far. Firstly, SnS₂, which acts as the channel, forms a Schottky junction with Au (Figure 5-17).

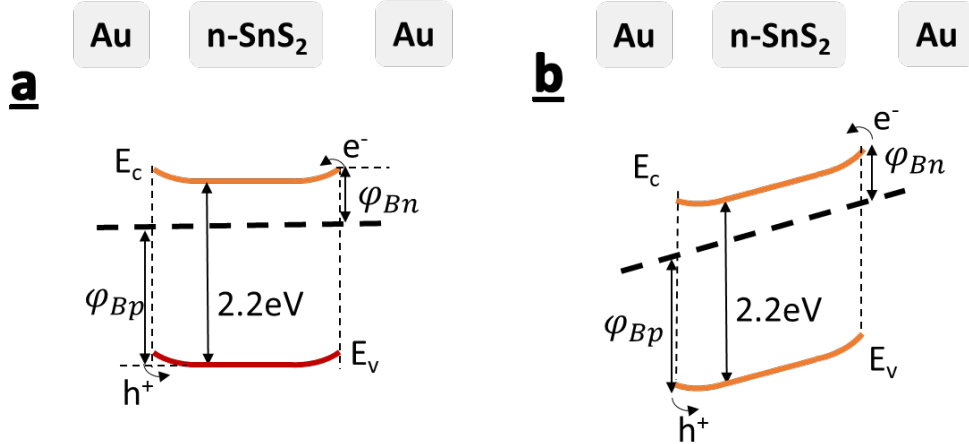


Figure 5-17. Band diagram of SnS₂/Au Schottky junction (a) with zero bias and (b) with non-zero bias

Current through the Schottky junction can be described by the thermionic emission model. So, the dark current density (J_d) under equilibrium in SnS₂ is given by the sum of electron (J_n) and hole currents (J_p). The following was adapted from the report by Gao et.al.^[98]

$$\begin{aligned}
 J_d &= J_n + J_p \\
 &= A_n^* T^2 \exp\left(-\frac{e\phi_{Bn}}{k_B T}\right) \left[\exp\left(\frac{eV_{ds}}{k_B T}\right) - 1\right] + A_p^* T^2 \exp\left(-\frac{e\phi_{Bp}}{k_B T}\right) \left[\exp\left(\frac{eV_{ds}}{k_B T}\right) - 1\right] \quad (\text{Eq5-1})
 \end{aligned}$$

where,

A_n^* → Effective electron Richard's constant for electrons,

A_p^* → Effective Richard's constant for holes,

k_B → Boltzmann's constant,

T → Absolute temperature,

e → Elementary charge constant,

ϕ_{Bn} → Electron barrier height between SnS₂ and Au,

ϕ_{Bp} → Hole barrier height between SnS₂ and Au, and

V_{ds} → External bias between source and drain

Similarly, carrier density of electrons (n) and holes (p) are related to the quasi Fermi levels (E_{Fn} and E_{Fp}) by the following relationship.

$$n = N_c \exp\left(-\frac{E_c - E_{Fn}}{k_B T}\right) \quad (\text{Eq 5-2})$$

$$p = N_v \exp\left(-\frac{E_{Fp} - E_v}{k_B T}\right) \quad (\text{Eq 5-3})$$

where,

$N_c \rightarrow$ Effective density of states at the conduction band (tabulated),

$N_v \rightarrow$ Effective density of states at the valence band (tabulated),

$E_c \rightarrow$ Conduction band energy,

$E_v \rightarrow$ Valence band energy,

$E_{Fn} \rightarrow$ Quasi Fermi level of electrons

$E_{Fp} \rightarrow$ Quasi Fermi level of holes

In equilibrium, $E_{Fn} = E_{Fp} = E_F$. Under illumination/non-equilibrium, the carrier density of electrons (n') and holes (p') are related to the quasi Fermi levels (E'_{Fn} and E'_{Fp}) by the following relationship.

$$n' = N_c \exp\left(-\frac{E_c - E'_{Fn}}{k_B T}\right) \quad (\text{Eq 5-4})$$

$$p' = N_v \exp\left(-\frac{E'_{Fp} - E_v}{k_B T}\right) \quad (\text{Eq 5-5})$$

Taking \ln on both sides of Equations 5-2- to 5-5.

$$E_c - E_{Fn} = k_B T \ln\left(\frac{N_c}{n}\right) \quad (\text{Eq 5-2b})$$

$$E_{Fp} - E_v = k_B T \ln\left(\frac{N_v}{p}\right) \quad (\text{Eq 5-3b})$$

$$E_c - E'_{Fn} = k_B T \ln\left(\frac{N_c}{n'}\right) \quad (\text{Eq 5-4b})$$

$$E'_{Fp} - E_v = k_B T \ln\left(\frac{N_v}{p'}\right) \quad (\text{Eq 5-5b})$$

The variation in barrier heights ($\Delta\phi_{Bn}$ and $\Delta\phi_{Bp}$) due to the non-equilibrium condition is determined by:

$$\Delta\phi_{Bn} = \frac{1}{e}(E'_{Fn} - E_{Fn})$$

$$\begin{aligned}
&= \frac{k_B T}{e} \left(\ln \left(\frac{N_c}{n} \right) - \ln \left(\frac{N_c}{n'} \right) \right) \\
&= \frac{k_B T}{e} \ln \left(\frac{n'}{n} \right)
\end{aligned} \tag{Eq 5-6}$$

$$\begin{aligned}
\Delta\phi_{Bp} &= \frac{1}{e} (E'_{Fp} - E_{Fp}) \\
&= \frac{k_B T}{e} \left(\ln \left(\frac{N_v}{p'} \right) - \ln \left(\frac{N_v}{p} \right) \right) \\
&= \frac{k_B T}{e} \ln \left(\frac{p}{p'} \right)
\end{aligned} \tag{Eq 5-7}$$

Using Equations (5-6) and (5-7), the new current density due to non-equilibrium electrons and holes is given by:

$$\begin{aligned}
J' &= J'_n + J'_p \\
&= \\
&A_n^* T^2 \exp \left(-\frac{e(\phi_{Bn} + \Delta\phi_{Bn})}{k_B T} \right) \left[\exp \left(\frac{eV_{ds}}{k_B T} \right) - 1 \right] + A_p^* T^2 \exp \left(-\frac{e(\phi_{Bp} + \Delta\phi_{Bp})}{k_B T} \right) \left[\exp \left(\frac{eV_{ds}}{k_B T} \right) - 1 \right] \\
&= \\
&A_n^* T^2 \exp \left(-\frac{e\phi_{Bn}}{k_B T} \right) \exp \left(-\frac{e\Delta\phi_{Bn}}{k_B T} \right) \left[\exp \left(\frac{eV_{ds}}{k_B T} \right) - 1 \right] + \\
&A_p^* T^2 \exp \left(-\frac{e\phi_{Bp}}{k_B T} \right) \exp \left(-\frac{e\Delta\phi_{Bp}}{k_B T} \right) \left[\exp \left(\frac{eV_{ds}}{k_B T} \right) - 1 \right]
\end{aligned}$$

So, in terms of the barrier height variation, the new current density is given by:

$$J' = J_n \exp \left(-\frac{e\Delta\phi_{Bn}}{k_B T} \right) + J_p \exp \left(-\frac{e\Delta\phi_{Bp}}{k_B T} \right) \tag{Eq 5-8}$$

Substituting from Equation (5-6) and (5-7), one can obtain:

$$J' = \frac{n}{n'} J_n + \frac{p'}{p} J_p$$

The change in current (ΔJ) is given by

$$\begin{aligned}
\Delta J &= J' - J_d \\
&= \frac{n}{n'} J_n + \frac{p'}{p} J_p - (J_n + J_p) \\
&= \left(\frac{n}{n'} - 1 \right) J_n + \left(\frac{p'}{p} - 1 \right) J_p
\end{aligned} \tag{Eq 5-9}$$

Equation (5-8) and (5-9) will be useful in explaining the photocurrent in our photodetectors.

Scenario: SnS_2 is coated with some PbS QDs

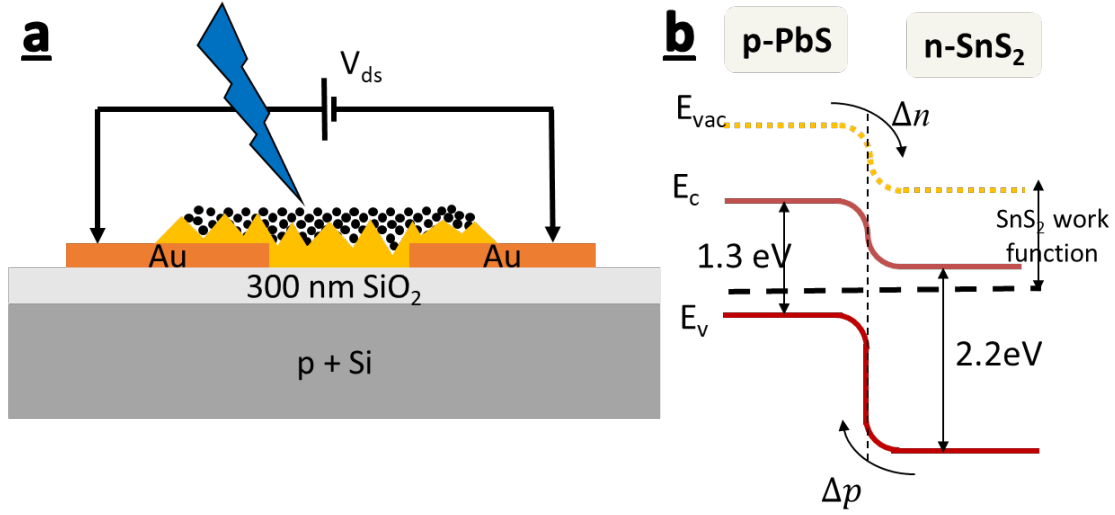


Figure 5-18. (a) Schematic of the heterostructure consisting of SnS_2 nanoflakes and PbS QDs and (b) Band diagram of the p-n junction formed between p-type PbS QDs and n-type SnS_2 nanoflakes^[98]

When p-type PbS QDs are coated onto n-type SnS_2 (Figure 5-18a), a depletion region is formed at their interface. This is represented in the band diagram in Figure 5-18b. When the heterostructure photodetector is illuminated, the built-in electric field at their interface helps inject photogenerated minority carrier electrons from PbS QDs to SnS_2 . At the same time, the photoexcited minority holes in SnS_2 are repelled by the photoinduced positively charged PbS QDs.

As discussed earlier, SnS_2 acts as the main channel while PbS QDs inject electrons into it. Under external electric field, the electrons either photogenerated in SnS_2 or transferred from PbS QDs can circulate through the SnS_2 channel to the Au contacts. Hence, the external photocurrent measured from these photodetectors can be modeled using Equations (5-8) and (5-9).

Let n_1 and p_1 be photogenerated electrons and holes respectively in SnS_2 . Let Δn be the concentration of electrons injected from PbS QDs into SnS_2 and Δp be concentration of holes injected from SnS_2 to PbS. $\Delta p \sim 0$ due to repulsion by the photoinduced positively charged PbS ions.^[98] Then:

$$n' = n + n_1 + \Delta n$$

$$p' = p + p_1 - \Delta p$$

Using Equation (5-9),

$$\begin{aligned}\Delta J &= \left(\frac{n}{n+n_1+\Delta n} - 1 \right) J_n + \left(\frac{p+p_1-\Delta p}{p} - 1 \right) J_p \\ &= -\frac{n_1+\Delta n}{n+n_1+\Delta n} J_n + \frac{p_1}{p} J_p\end{aligned}$$

With low light injection assumption ($n \gg n_1, \Delta n$) and the fact that the number of photogenerated holes always equal the number of photogenerated electrons ($n_1 = p_1$),

$$\Delta J_{PbS} = -\left(\frac{n_1+\Delta n}{n} \right) J_n + \left(\frac{n_1}{p} \right) J_p \quad (\text{Eq 5-10})$$

According to this relation, the photocurrent is dictated by the magnitudes of the negative and positive terms. Since $\varphi_{Bn} = \varphi_{Au} - \chi_{SnS_2} \sim 5.1 - 4.4 = 0.7eV$ and $\varphi_{Bp} = E_g - \varphi_{Au} + \chi_{SnS_2} \sim 2.2 - 5.1 + 4.4 = 1.5eV$, $J_n \sim J_p^2$. Similarly, $n > p$ or $n \gg p$ because SnS₂ is an n-type semiconductor. Although exact estimation of photocurrent using this equation is very difficult due to too many unknown parameters, one can make some conclusions with some assumptions.

The negative term is generally small due to a large value of n , however, when enough PbS QDs are added, Δn increases as a result of significant light absorption in PbS QDs which injects more electrons into SnS₂. Meanwhile, $n_1 = p_1$ decrease significantly due to less light reaching SnS₂. Consequently, the negative term dominates the overall photocurrent, as seen in the negative photoconductivity of our heterostructure devices. On the contrary, if the light intensity is increased such that the light absorbed by SnS₂ channel is non-negligible, the positive term dominates the overall photocurrent.

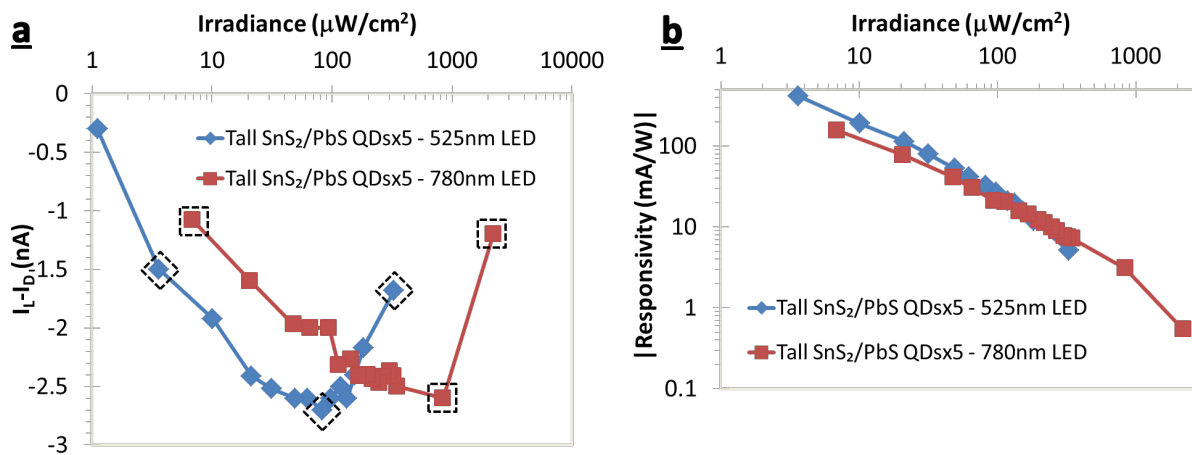


Figure 5-19. (a) Photocurrent and (b) responsivity of tall SnS_2 with 5 layers of PbS QDs at various illumination intensities. The dotted square and diamond symbols represent the photo responses which are plotted in the next figure.

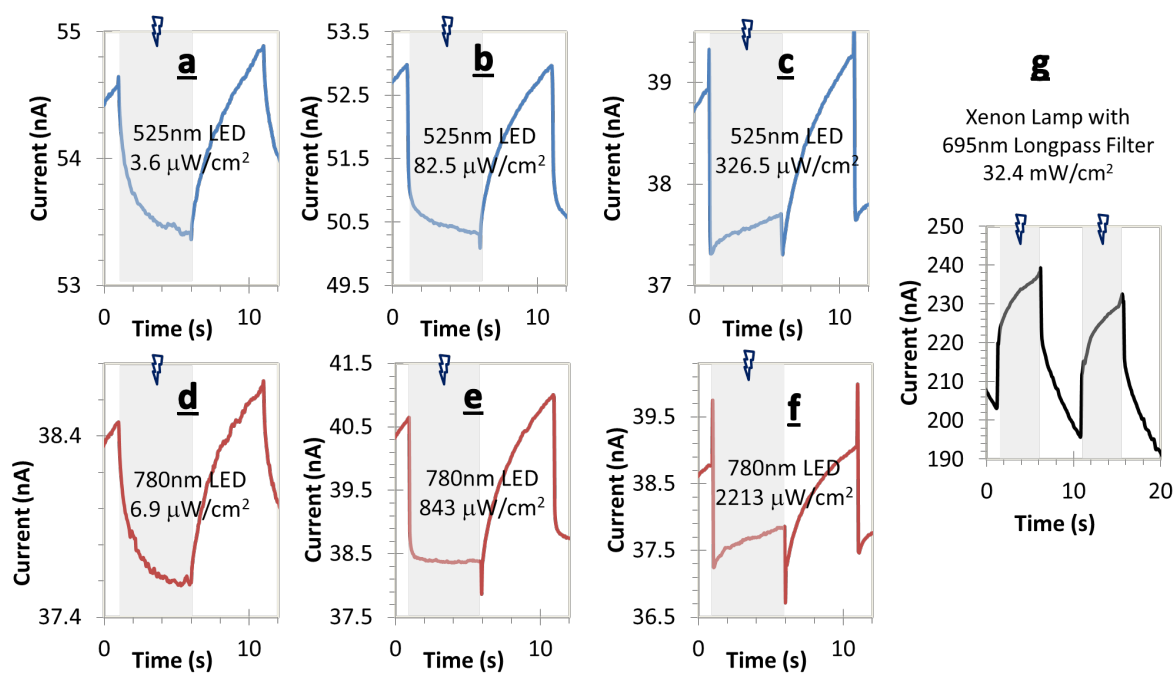


Figure 5-20. Transient response of photodetectors made of tall SnS_2 with 5 layers of PbS QDs at various illumination intensities

In order to further explore the nature of photoconductivity, tall SnS_2 nanoflakes with only 5 layers of PbS QDs were illuminated with various intensities of light (Figure 5-19). With both 525nm and 780nm light, as the light intensity is increased, negative photocurrent reaches a maximum magnitude after which, it starts to decrease and eventually turns into positive

photocurrent. However, the absolute responsivity continues to decrease even though the photocurrent switches signs (Figure 5-19b). As shown in Figure 5-20a-g, the photocurrent with low intensity LED lights (3.6 to $2213 \mu\text{W}/\text{cm}^2$) is negative while that with high intensity filtered light from Xenon lamp (Longpass 695nm filter, $32.4\text{mW}/\text{cm}^2$) is positive.

5.4.6. Heterostructure Photodetector with Several Layers of PbS QDs

Additional PbS QDs (up to 30 layers) were coated onto the SnS_2/PbS QDs photodetectors and characterized in order to understand the negative photoconductivity observed in the heterostructure photodetectors. As shown in Figure 5-21, when PbS QDs are added to the SnS_2 film, the dark current increases significantly at first. This is because the SnS_2 surface gets n-doped by EDT, which is used for ligand exchange. Similar observation was made by Kufer et.al. in MoS_2/PbS photodetectors.^[106] Another consequence of n-doping of SnS_2 is that its junction with Au becomes more Schottky, which is reflected in the clear non-linear shape of the I-V curve in Figure 5-11. The subsequent deposition of p-type PbS QDs turns the SnS_2 film again less n-type doped due to the reduction in number of free electrons by formation of the heterojunction between the n-type SnS_2 layer and the p-type PbS QDs film.^[106] However, this SnS_2 is still more n-type than the original SnS_2 evident from the nonlinear I-V curve of the heterostructure with 30 layers of PbS QDs (Figure B-1, Appendix B).

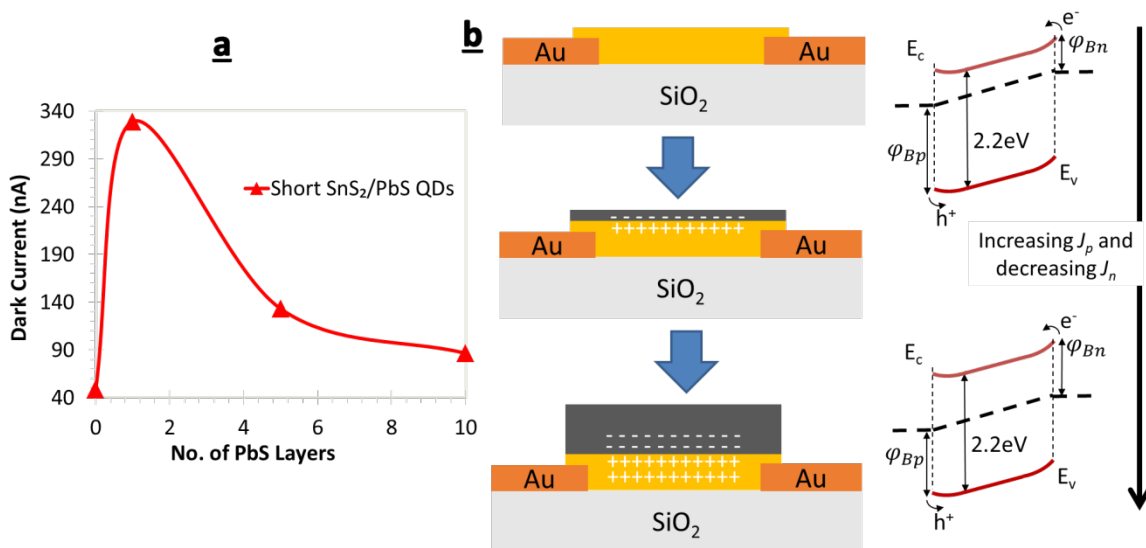


Figure 5-21. (a) Dark current of the short SnS_2/PbS QDs photodetector as a function of no. of layers of PbS QDs; (b) Schematic representation of the depletion layer formation at SnS_2/PbS interface as more PbS QDs are added

In terms of photocurrent, the tall SnS₂/PbS QDs heterostructure device with up to 20 layers of PbS QDs exhibits negative photocurrent when illuminated with 780nm light (Figure 5-22a). With the additional 10 layers of PbS QDs, the device starts to exhibit positive photoconductivity. This can also be understood using Equation 5-10, which was derived earlier.

$$\Delta J_{PbS} = -\left(\frac{n_1 + \Delta n}{n}\right)J_n + \left(\frac{n_1}{p}\right)J_p \quad (\text{Eq 5-10})$$

As more PbS QDs are added to the device, more of the SnS₂ channel gets depleted, an effect similar to applying sub-threshold gate voltage ($V_{gate} < V_{th}$) in a phototransistor where the Fermi level is shifted down.^[203-206] Consequently, the electron barrier height increases and the contribution of electrons to the dark current (J_n) decreases, even though the total dark current doesn't decrease significantly. This results in the positive term in Equation (5-10) dominating the photocurrent. However, this photocurrent is not as high as the negative photocurrent obtained with 10 layers of PbS QDs.

It can also be seen from the transient current measurements (Figure 5-22c-f) that when 10 layers of PbS QDs are added, the time constant related to LED-on (fall time ~ 1.9 s) is smaller than that related to LED-off (rise time ~ 3.7 s). This is because the photoexcited electrons from PbS QDs are injected into SnS₂ under the built-in electric field of the p-n junction at their interface, which leads to a slightly faster response when the device is illuminated. However, when the light is removed abruptly, the photoexcited carriers may still be trapped in SnS₂ defect sites, and escape slowly to the contacts, leading to a longer time constant.^[207]

With 20 layers of PbS QDs, one can see that when the LED is turned off, the current decreases sharply at first, which is then followed by slow increase. This sharp decrease is associated with the abrupt cut in photogenerated electrons from PbS QDs. However, due to very small time constant in comparison to the other phenomena in SnS₂, this only appears as a spike while the slow response of SnS₂ dominates the rest of the response. On the contrary, when 30 layers of PbS QDs are added, the fast component dominates both the rise and fall responses, leading to overall positive photocurrent. Remnant of the slow response can still be seen in the off state. This shift in the photoresponse mechanisms can be due to widened depletion region that penetrates more into SnS₂ channel as a result of adding more PbS QDs (Figure 5-21b).

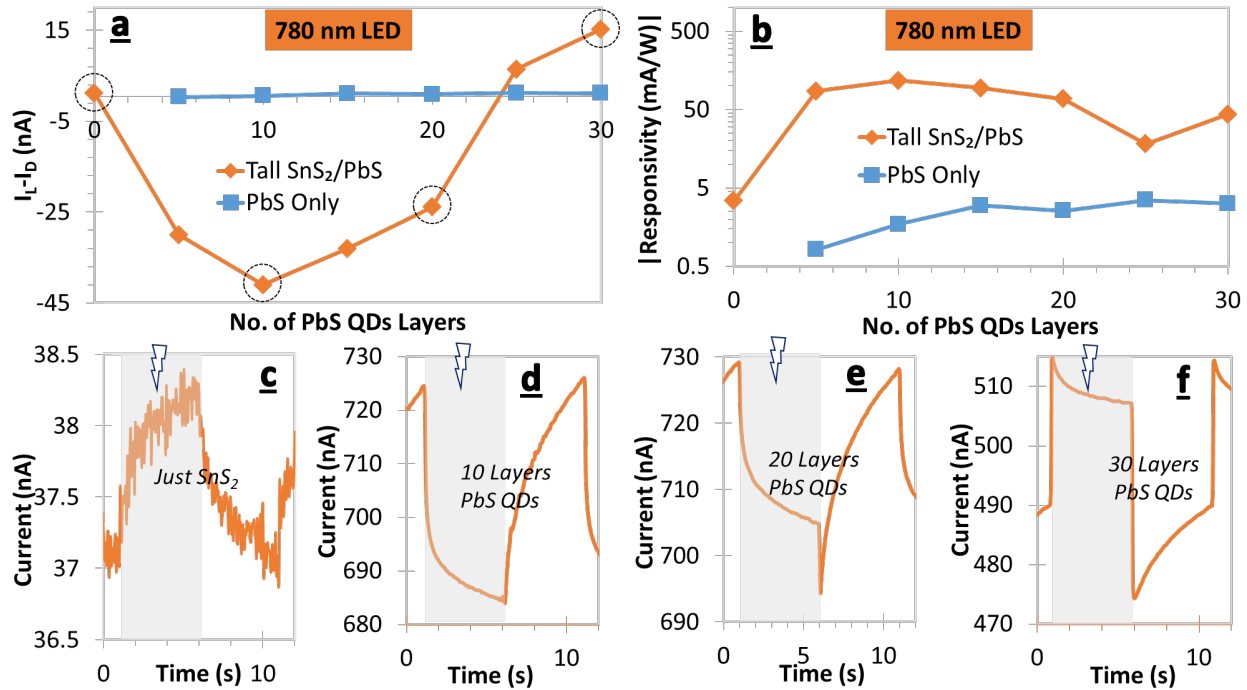


Figure 5-22. Photocurrent (a) and responsivity (b) obtained from the tall SnS₂/PbS QDs device with varying number of PbS layers; Transient current response of the device (c-f) with just SnS₂ as well as with 10, 20 and 30 layers of PbS QDs, Bias voltage = 5V and $\lambda=780\text{nm}$. The corresponding Figure B-2 with 525nm is in Appendix B.

In order to further explore this photoresponse, the 2min grown short SnS₂ was coated with multiple layers of PbS QDs in the same way as above. According to Figure 5-23, only 5 layers of PbS QDs were sufficient to obtain positive photoconductivity, after which any additional PbS only lowered the performance. It should be pointed out that short SnS₂ with only 5 layers of PbS QDs (Figure 5-23d) has a very similar transient response as tall SnS₂ with 30 layers of PbS QDs (Figure 5-22f). The responsivity obtained with short SnS₂/PbS QDs is only about one order of magnitude higher than PbS only devices, however, the response times are much smaller than tall SnS₂/PbS devices. This tradeoff between responsivity and response times has been well known in the literature.^[101, 103, 187, 208-210]

Photodetector performances with the one of the best responsivities and one of the best response times are shown in Table 5-1. The sample with the high responsivity of 2.03 A/W under 780nm light also has long response times. On the contrary, the sample with the fast response time of 12 ms only has the responsivity of 0.243 A/W. These values are plotted in Figure 5-24 and have similar performances as many photodetectors based on other 2D materials.

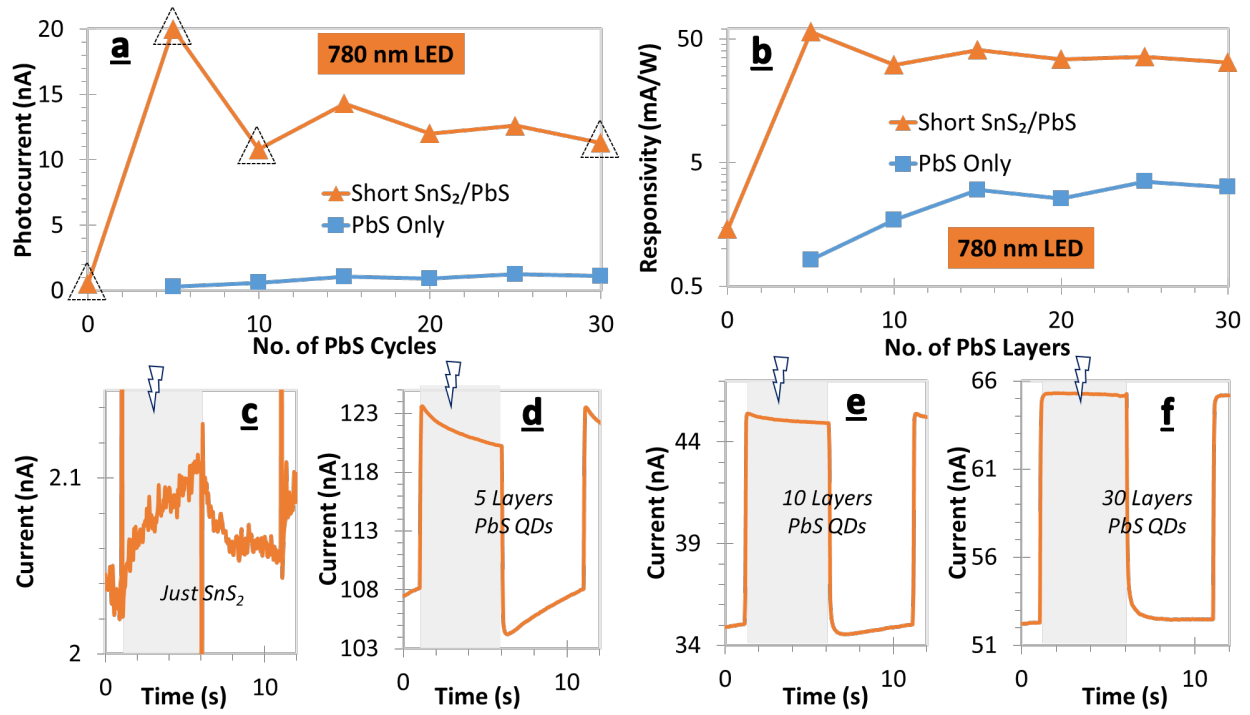


Figure 5-23. Photocurrent (a) and responsivity (b) obtained from the short SnS₂/PbS QDs device with varying number of PbS layers; Transient current response of the device (c-f) with just SnS₂ as well as with 5, 10 and 30 layers of PbS QDs, Bias voltage = 5V, $\lambda=780\text{nm}$. The corresponding Figure B-3 with 525nm is in Appendix B.

Table 5-1. Responsivity and response time of two representative samples under 780nm illumination, $6.9 \mu\text{W}/\text{cm}^2$ and 5V bias

Sample	Responsivity	Response time
Tall SnS ₂ nanoflakes + 10 layers PbS QDs	2030 mA/W	1.9s (on), 3.7s (off)
Short SnS ₂ nanoflakes + 5 layers PbS QDs	243 mA/W	12ms (on), 64ms (off)

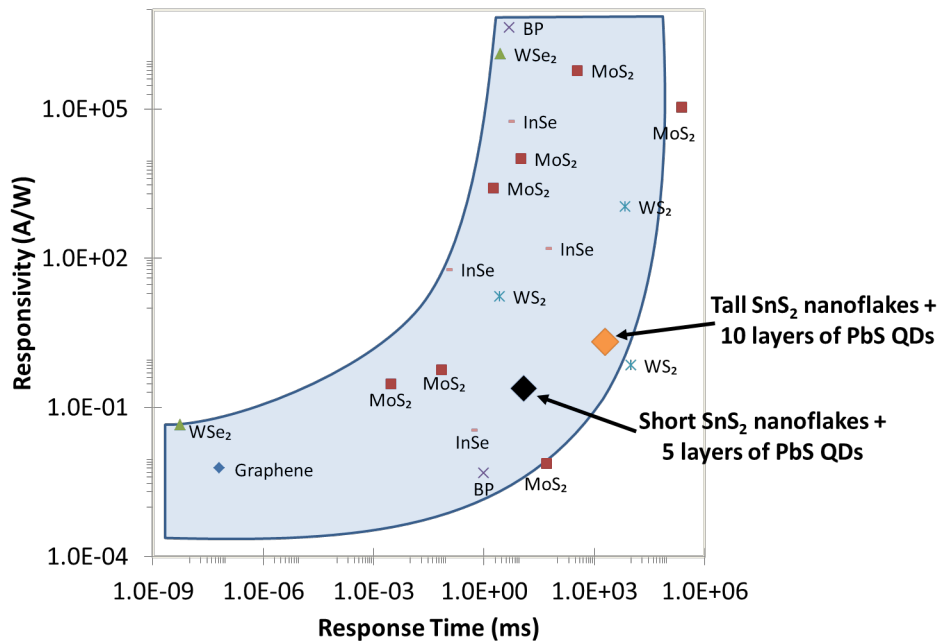


Figure 5-24. Responsivity and response time of the two best SnS₂/PbS heterostructure photodetectors in comparison to other photodetectors based on different 2D materials. The empty space in the top left corner shows the lack of photodetectors with both fast speed and high responsivity. Adapted from ^[103]

5.4.7. Response Time and Frequency Response

Response time is an important figure of merit for photodetectors as it determines the speed of sensors. Hence, the response times (time constant) of our SnS₂/PbS heterostructure devices were measured. According to Figure 5-25, the rise times (LED-on) and fall times (LED-off) of devices with tall SnS₂ and 30 layers of PbS QDs were similar respectively to the rise and fall times of devices made of 30 layers of PbS QDs. This suggests that the heterostructure devices retain the response times of PbS QDs while also increasing the responsivity by order of magnitudes.

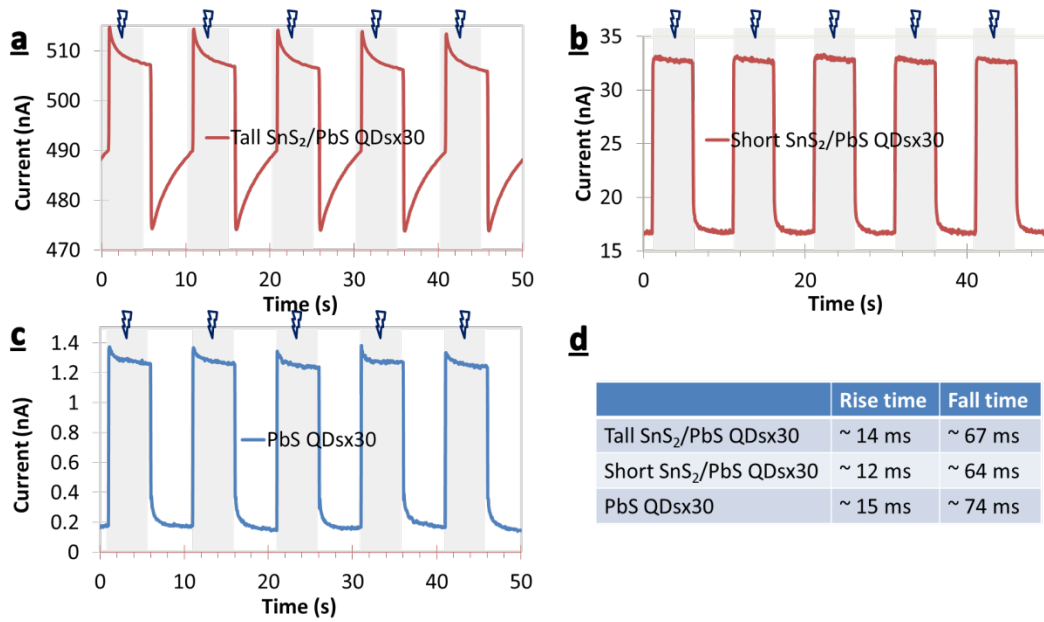


Figure 5-25. Transient current response of (a) tall SnS₂ with 30 layers of PbS QDs; (b) short SnS₂ with 30 layers of PbS QDs; and (c) only 30 layers of PbS QDs. (d) Summary of the rise and fall times of the three devices when illuminated with 780nm LED

Figure 5-26a shows the frequency domain response of the heterostructure photodetector obtained by measuring the photocurrent at various LED frequencies. The -3dB frequency, which is defined as the frequency at which the photocurrent drops to half of the initial value was ~40 Hz for 780nm and ~100Hz for 525nm illumination. According to Figure 5-26b, the -3dB frequencies of the heterostructure devices are slightly greater than that of PbS QDs only device. This shows that the frequency response of PbS QDs is not compromised by the formation of heterostructure with SnS₂ nanoflakes.

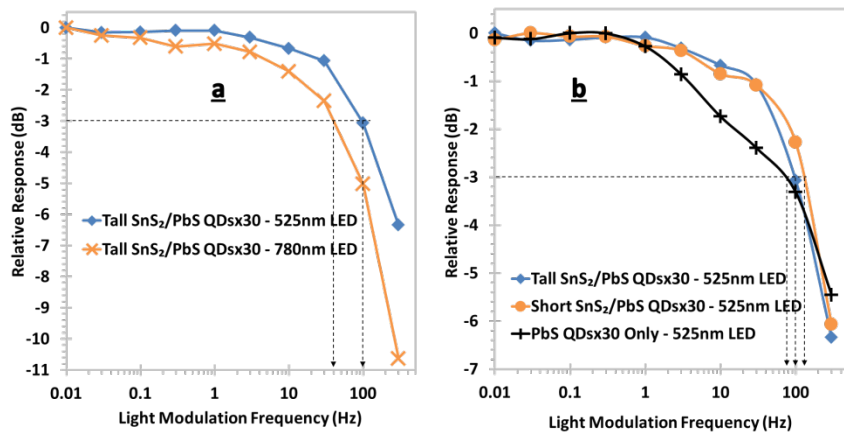


Figure 5-26. Frequency response of PbS only and SnS₂/PbS heterostructure devices. (a) tall SnS₂ with 30 layers PbS QDs under 525nm and 780nm illumination; and (b) all three devices under 525nm illumination

5.5. Conclusion

In this project, SnS₂ nanoflakes/PbS QDs heterostructure photodetectors were fabricated using only scalable methods. The champion heterostructure device yielded responsivity of 3.05 A/W, almost two orders of magnitude higher than 0.055 A/W obtained from SnS₂ only device and 0.013 A/W obtained from PbS QDs only device under the same test conditions (525nm LED, 3.6 μ W/cm², 5V bias).

Both positive and negative photoconductivity were obtained by tuning the growth of SnS₂ nanoflakes and the amount of PbS QDs. Negative photoconductivity with the highest responsivity was obtained from the device with tall SnS₂ nanoflakes and 10 layers of PbS QDs whereas positive photoconductivity with the shortest response time was obtained from the device with short SnS₂ nanoflakes and 5 layers of PbS QDs. The horizontal growth of SnS₂ was believed to be responsible for enhanced mobility of SnS₂ channel and vertical growth was responsible for enhanced absorption. For the fastest response speed, a thinner and continuous horizontal layer of SnS₂ was desired, which could be obtained by using shorter growth durations and low supersaturation of SnS₂ vapor. However, for the highest responsivity, thicker and taller SnS₂ nanoflakes as well as a thicker layer of PbS QDs were desired. The taller nanoflakes could be produced simply by increasing growth duration and increasing supersaturation of SnS₂ vapor. This work demonstrates that heterostructure photodetectors with characteristics superior to either of the constituents can be constructed from SnS₂ nanoflakes and PbS QDs.

Chapter 6: Conclusion and Future Recommendations

6.1. Summary and Conclusion

This dissertation was undertaken to investigate various characteristics and syntheses of 2D metal dichalcogenides, with a focus on tin disulfide (SnS_2), for applications in photoelectrochemical water splitting and photodetectors. SnS_2 is an emerging material with very promising properties but it is not well understood, hence this dissertation will be valuable in shedding light upon various unknown aspects of SnS_2 .

In Chapter 3, a CSS system was custom designed and built to synthesize pure and highly crystalline vertically aligned nanoflakes of SnS_2 on various substrates. The system allowed independent control of growth time, source temperature, substrate temperature as well as source-substrate distance. The optimized SnS_2 nanoflakes on glass/FTO substrates showed excellent optoelectronic and electrochemical properties. They exhibited high intrinsic carrier mobility ($330 \text{ cm}^2\text{V}^{-1}\text{s}^{-1}$) and long photoexcited carrier lifetimes (1.3 ns), which resulted in large diffusion lengths of $\sim 1 \text{ }\mu\text{m}$.

The nanoflakes grown on glass/FTO were applied to photoelectrochemical water oxidation in Chapter 4 to produce the highest performing SnS_2 photoanodes in the literature. These photoanodes yielded photocurrents as high as 4.5 mAcm^{-2} in aqueous phosphate buffer with $1 \text{ M Na}_2\text{SO}_3$ and 2.6 mAcm^{-2} in aqueous $0.5 \text{ M Na}_2\text{SO}_4$, both at $1.23 \text{ V}_{\text{RHE}}$ under simulated AM1.5G sunlight. Using various characterizations, and nanoparticle deposition, the origin of this high photocurrent was shown to be the combination of excellent optoelectronic properties, unique stepped morphology that exposed multiple edge sites in every nanoflake, and the optimized nanoflake height ($\sim 1.5 \text{ }\mu\text{m}$) that balanced light absorption and charge transport.

In a second application described in Chapter 5, the growth of SnS_2 nanoflakes was slightly modified to produce a continuous film on non-conductive SiO_2 substrates, and used to enhance the performance of PbS photodetectors. The SnS_2/PbS heterostructure photodetectors yielded the highest responsivity of 3.05 A/W , almost two orders of magnitude higher than 0.055 A/W obtained from SnS_2 only device and 0.013 A/W obtained from PbS only device under the same test conditions.

The following list summarizes some of the original contributions of this dissertation to the field of nanomaterials and nanotechnology.

- Development of a CSS system for scalable synthesis of SnS₂ nanoflakes at a low cost
- Demonstration of the tunability of the CSS system and the effects each synthesis parameter has on the characteristics of the final product, SnS₂ nanoflakes
- Evidence of the enhanced activity of SnS₂ nanoflakes for water splitting due to the unique stepped morphology and excellent material properties
- Engineering of the heterostructure consisting of SnS₂ nanoflakes and PbS QDs to obtain 2 orders of magnitude enhancement in photodetector performance
- Development of a physical model to describe the behavior of the SnS₂ nanoflakes/PbS QDs heterostructure photodetectors

6.2. Future Recommendations

Close Space Sublimation System

One aspect that the CSS system that can be addressed in the future revisions is the control over the water coolant temperature. In the current system, the coolant through the substrate holder has an undesirable effect of cooling the source, which makes it harder to independently control source temperature. So, a possible way this can be improved is by maintaining a consistent temperature of the incoming coolant by using a feedback controlled chiller or a heater.

If the CSS system is to be used to synthesize materials that are easily degraded in the ambient atmosphere, inert gas flow lines can be added to the silicone stopper to allow refilling the chamber with inert gas before removing the sample.

Vertical SnS₂ Nanoflakes for Photoanodes

In Chapter 4, it was shown that the optimized SnS₂ nanoflakes had an intrinsically high ability to capture solar energy and catalyze electrochemical reactions; however, they were also susceptible to degradation in the harsh electrochemical environment of water splitting. One way to maximize the performance from SnS₂ nanoflakes is by avoiding this degradation and utilizing them in solar energy conversion applications that contain iodide/triiodide redox couples. For example, one could design a liquid-junction solar cell using SnS₂ photoelectrodes similar to dye-sensitized solar cells that generate photocurrent by cycling between the two oxidation states of iodine.

Another possible solution to the degradation problem is to engineer appropriate coatings that can passivate SnS₂ nanoflakes and catalyze the water oxidation without interfering with the transport of holes from SnS₂ to the electrolyte. This may require utilizing co-catalyst nanoparticles such as TiO₂ and CdS or organic ligands such as 1,2-benzenedithiol that bind selectively to the sites of degradation.

SnS₂/PbS QDs Photodetectors

In Chapter 5, the SnS₂ nanoflakes/PbS QDs heterostructure photodetector was shown to enhance the responsivity of PbS-only photodetector by 2 orders of magnitude. This was a significant result by itself; however, the values of responsivities were lower than some reports in the literature. A few changes to the device structure can help bring these figures of merit on a par with these reports.

A simple way to improve the responsivity of photodetectors is to use a shorter channel length.^[211] In this dissertation, 40µm channel length was used in order to keep the photolithography simple and focus on the fundamental aspects of a heterostructure. However, the performance can be further enhanced by decreasing the channel length to ~1µm, which is close to the diffusion length of photoexcited carriers, using a slightly more advanced photolithography system.

Alternatively, small channel length (~300-1000nm) in photodetectors can be achieved by fabricating them in a vertical fashion (i.e. with vertical SnS₂ nanoflakes sandwiched between top and bottom contacts). This would allow the charge carriers to move only along the basal planes and make the most out of high mobility in SnS₂ basal planes.^[212] It should be noted that this architecture requires one of the contacts to be transparent and the area of the contacts need to be decreased to minimize high capacitance, which tends to decrease the response speed.

It is well known that monolayers of 2D materials have the highest mobility, hence in the future; synthesizing monolayer SnS₂ using CSS can be investigated. One of the ways to achieve this is by using seed layers that force the heterogeneous nucleation to occur at the middle of the channel and lowering the supersaturation so that horizontal growth is favored.^[213]

PbS QDs make exciting photodetectors but their behavior is often determined by their capping ligands. In Chapter 5, oleic acid ligands were exchanged with the commonly-used EDT ligands,

however, EDT is known to introduce traps and defects, which can lower minority carrier lifetime and decrease photogain.^[214] It was also observed in Chapter 5 that EDT ligands significantly increased the dark current of SnS₂ channel, resulting in low on-off ratios. Hence, other alternative ligands such as thiols [1,3-benzenedithiol (BDT), 3-mercaptopropionic acid (MPA)], a primary amine [1,2-ethylenediamine (EDA)], ammonium thiocyanate (SCN), and halides [tetrabutylammonium iodide (TBAI)], which can passivate PbS QDs better without doping SnS₂ can be explored in future devices.^[214] Yet another way to enhance the performance is to use different quantum dots based on alloys of Pb and other metal sulfides.

The scalability of SnS₂/PbS heterostructures can be further explored by preparing printable inks that contain exfoliated SnS₂ nanoflakes obtained by LPE and colloidal PbS QDs. These inks can then be used with graphene inks (for contacts) to print flexible and stretchable photodetectors for many applications.

Publications to Date and Planned Publications

Publications to Date

1. **B. Giri**, M. Masroor, T. Yan, K. Kushnir, A. D. Carl, C. Doiron, H. Zhang, Y. Zhao, A. McClelland, G. A. Tompsett, D. Wang, R. L. Grimm, L. V. Titova, P. M. Rao, “Balancing Light Absorption and Charge Transport in Vertical SnS₂ Nanoflake Photoanodes with Stepped Layers and Large Intrinsic Mobility”, *Advanced Energy Materials* 2019, 9, 1901236. (Impact Factor: 24.88 (2018) Total citations to date: 6, DOI: [10.1002/aenm.201901236](https://doi.org/10.1002/aenm.201901236))
2. C. Ye, Y. Yang, J. Zhang, L. Zhou, T. Yan, **B. Giri**, S. P. Salgado, H. Feng, A. Shah, A. Giaya, P. M. Rao, “Superhydrophobic behavior of polymer-coated nanowire-arrays as a function of interfacial affinity and etching”, *Materials Research Express*, 2019. (Impact factor: 1.449 (2018))
3. K. Kushnir, K. Chen, L. Zhou, **B. Giri**, R. L. Grimm, P. M. Rao, and L. V. Titova: “Dynamics of Photoexcited Carriers in Polycrystalline PbS and at PbS/ZnO Heterojunctions: Influence of Grain Boundaries and Interfaces”, *The Journal of Physical Chemistry C*, 2018, 122, (22), pp. 11682-11688 (Impact factor: 4.3 (2018))
4. L. Zhou, C. Zhao, **B. Giri**, P. Allen, X. Xu, H. Joshi, Y. Fan, L. V. Titova and P. M. Rao, "High Light Absorption and Charge Separation Efficiency at Low Applied Voltage from Sb-Doped SnO₂/BiVO₄ Core/Shell Nanorod Array Photoanodes", *Nano Letters*, 16 (6), 3463–3474, 2016. (Impact Factor: 12.080 (2017). Total citations to date: 100)

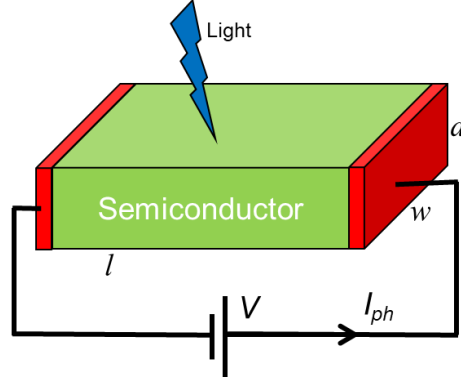
Manuscripts under Preparation

1. **B. Giri**, M. Masroor, N. R. Pratt, S. Liu, T. Shi, K. Kushnir, L. V. Titova and P. M. Rao, “Highly-Efficient Vertical SnS₂ Nanoflake Photodetectors Decorated with PbS Quantum Dots,” *Tentative*, 2020.
2. **B. Giri & J. Jacobs**, H. Zhang, D. Wang and P. M. Rao, “Synthesis of Vertical MoS₂ nanoflakes for Hydrogen Evolution Reaction,” *Tentative*, 2020.
3. **B. Giri & S. Liu**, E. M. Brack, C. P. Drew and P. M. Rao, “Decontamination of Wastewater Using Nanostructured BiVO₄ Photoelectrodes ,” *Tentative*, 2020.

Appendix A

Derivation of expression for photoconductive gain, G

Consider a n-type semiconductor slab of length l , width w and depth d is illuminated with light of wavelength λ .



The **volumetric photo-generation rate (g_{ph})** is defined in terms of internal quantum efficiency (η_i), illuminated area (A), and incident photon flux (Φ_{ph}) as:

$$g_{ph} = \frac{\eta_i * A * \Phi_{ph}}{Volume} = \frac{\eta_i * (l * w) * \Phi_{ph}}{(l * w * d)}$$

Let I be total intensity (W/m^2) of the incident light, then g_{ph} can be expressed in terms of wavelength λ and speed of light c as:

$$g_{ph} = \frac{\eta_i * \left(\frac{I}{h * \nu}\right)}{d} = \frac{\eta_i * I * \lambda}{h * c * d} \quad (A-1)$$

Similarly, **photocurrent density J_{ph}** of the photoconductor can be defined as the sum of electron current J_n and hole current density J_p :

$$J_{ph} = J_n + J_p = e * \mu_n * \Delta n * E + e * \mu_p * \Delta p * E = eE * (\mu_n * \Delta n + \mu_p * \Delta p)$$

where, e is elementary charge, E is electric field, Δn is the density of photoexcited electrons and Δp is the density of photoexcited holes. Since $\Delta n = \Delta p$, and at steady state illumination and uniform photogeneration, $\Delta n = g_{ph} * \tau_{minority}$, J_{ph} can be rewritten as:

$$J_{ph} = e * E * \Delta n (\mu_n + \mu_p) = e * E * (g_{ph} * \tau_{minority}) (\mu_n + \mu_p) \quad (A-2)$$

Now, since **photoconductive gain, G** is defined as:

$$G = \frac{\text{rate of electron flow in external circuit}}{\text{rate of electron generation by light absorption}}$$

where, rate of current flow in external circuit = $\frac{I_{ph}}{e} = \frac{w*d*J_{ph}}{e} = \frac{w*d*(e*E*g_{ph}*\tau_{minority}(\mu_n+\mu_p))}{e}$
using Equation (A-2). Similarly, rate of electron generation by light absorption = $l * w * d * g_{ph}$. Hence,

$$G = \frac{\frac{w*d*(e*E*g_{ph}*\tau_{minority}(\mu_n+\mu_p))}{e}}{l*w*d*g_{ph}}$$

$$\text{Therefore, } G = \frac{\tau_{minority}(\mu_n+\mu_p)E}{l} \quad (\text{A-3})$$

In order to further simplify Equation (A-3), one can use the concept of electron and hole transit times t_e and t_h respectively. Transit time is the time it takes for the charge to cross the semiconductor length l .

$$t_e = \frac{l}{\mu_n E} \rightarrow l = t_e \mu_n E$$

$$t_h = \frac{l}{\mu_p E}$$

Since the majority electrons determine the current through the photoconductor, the expression for electron transit time can be used to obtain Equation A-4.

$$G = \frac{\tau_{minority}(\mu_n+\mu_p)E}{l} = \frac{\tau_{minority}(\mu_n+\mu_p)E}{t_e \mu_n E}$$

$$\text{Therefore, } G = \frac{\tau_{minority}}{t_e} \left(1 + \frac{\mu_p}{\mu_n} \right) \quad (\text{A-4})$$

This implies that the photoconductive gain of a photoconductor depends on the electron transit time. A smaller electron transit time leads to a higher gain.

Detailed recipe for photolithography of gold contacts:

1. Prepare the SiO₂/Si wafer
 - a. Clean and dry the substrate
 - b. Heat on hot plate at 130°C for 10 min
 - c. Cool to room temperature
2. Spin coating the photoresist
 - a. Drop enough photoresist to cover the entire wafer/substrate
 - b. Program settings:
 - i. First step: 500rpm, 100rpms, 10s
 - ii. Second step: 5000rpm, 1000rpms, 30s
3. Softbake
 - a. Heat on hot plate at 65°C for 2min
 - b. Heat on hot plate at 96°C for 3min
 - c. Heat on hot plate at 65°C for 2min (to cool slowly)
 - d. Cool to room temperature
4. UV Expose Energy - 175 mJ/cm²
 - a. Expose the photoresist through the mask with appropriate setting, making sure the energy dosage is 175 mJ/cm²
 - b. Since this is contact lithography, place the mask right on top of the wafer with the printed side of the mask closest to the photoresist
5. Post-exposure Bake
 - a. Heat on hot plate at 65°C for 1min
 - b. Heat on hot plate at 95°C for 3min
 - c. Cool to room temperature
6. Develop (by immersion)
 - a. Immerse the exposed wafer in the developer solution for about 5 minutes with gentle shaking
 - b. After 5 minutes, rinse the wafer on the front and the back with the developer solution
 - c. Then rinse with IPA to remove the developer
 - d. If you are not convinced that the wafer is fully developed, immerse in the developer for additional time

- e. Finally dry gently with N₂ gas
7. Thermal evaporation of Au
- a. Place the wafers with the developed patterns in the vacuum chamber and ensure they are not exposed to light during the wait
 - b. Thermally evaporate about 80nm thick gold
 - c. Immerse the wafer with thermally evaporated Au in an acetone bath in the dark for about 6 hrs or longer if necessary
 - d. At the end, all the SU-8 will peel-off and gently remove the peeled-off pieces and check the continuity of Au pads

Recipe for coating SnS₂ nanoflakes with PbS QDs

Table A-1. The steps involved in each layer of PbS QDs

Step	Description
1	Drop 40ul of 2% EDT (in MeCN) onto the SnS ₂ nanoflakes device → Spin dry (@2500rpm, 1000rpms, 10s)
2	Drop 8ul of 5mg/ml PbS QDs (in Toluene)→Wait 30s → Spin dry (@2500rpm, 1000rpms, 10s)
3	Drop 20ul of 2% EDT → Wait 30s → Spin dry (@2500rpm, 1000rpms, 10s)
4	Drop 40ul of clean acetonitrile → Spin dry (@2500rpm, 1000rpms, 10s)
5	Drop 40ul of clean toluene → Spin dry (@2500rpm, 1000rpms, 10s)

The first step was necessary to prepare the surface to accept PbS QDs. Since EDT molecule consists of two thiol (S-H) groups, one thiol group is expected to anchor to the SnS₂ nanoflakes and the other thiol group is expected to anchor to the PbS QDs. The treatment of PbS QDs with EDT in step 3 is expected to perform complete ligand exchange. In steps 4 and 5, the device is rinsed with acetonitrile and toluene respectively in order to get rid of unreacted EDT molecules and disconnected oleic acid molecules respectively. The devices were tested after every 5 layers of PbS QDs. Prior to the test, the sample was further dried on hot plate at 90 °C for 10min.

Appendix B

Additional Figures:

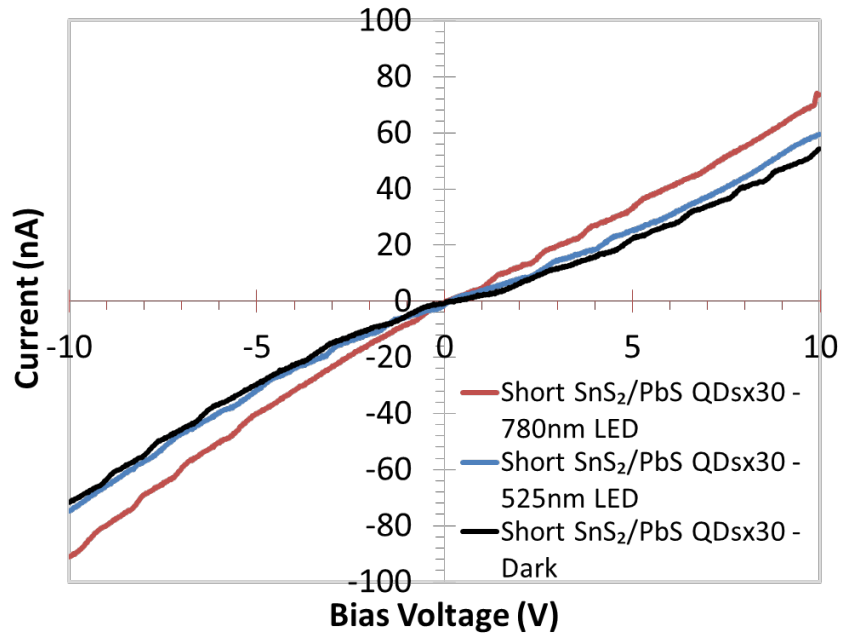


Figure B-1. Current-Voltage characteristic of short SnS_2 nanoflakes with 30 layers of PbS QDs. The nonlinear shape shows that the junction between SnS_2 and Au is Schottky

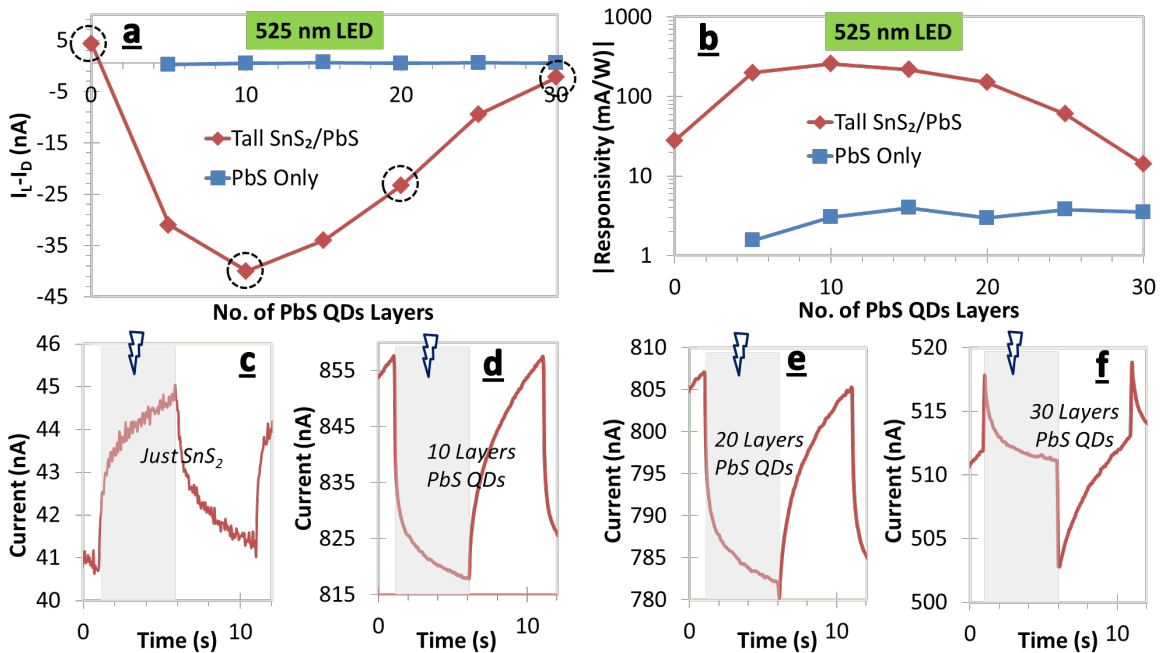


Figure B-2. Photocurrent (a) and responsivity (b) obtained from the tall SnS_2/PbS QDs device with varying number of PbS layers; Transient current response of the device (c-f) with just SnS_2 as well as with 10, 20 and 30 layers of PbS QDs, Bias voltage = 5V and $\lambda=525\text{nm}$. The corresponding response with 780nm is in the main text.

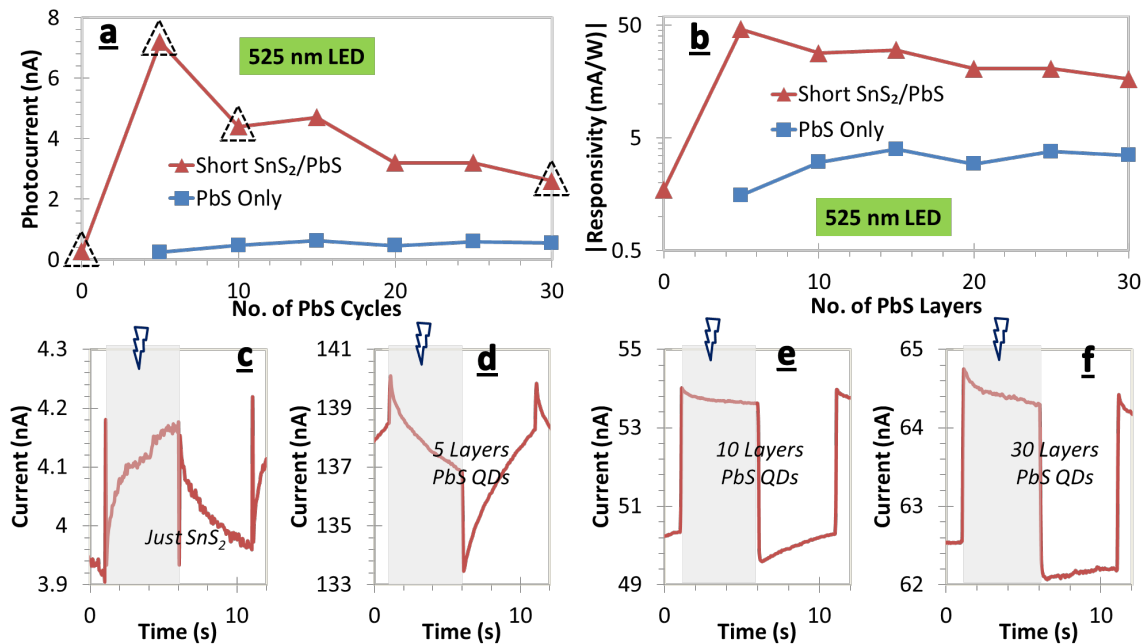


Figure B-3. Photocurrent (a) and responsivity (b) obtained from the short SnS₂/PbS QDs device with varying number of PbS layers; Transient current response of the device (c-f) with just SnS₂ as well as with 5, 10 and 30 layers of PbS QDs, Bias voltage = 5V and $\lambda=525\text{nm}$. The corresponding response with 780nm is in the main text.

References

- [1] P. Friedlingstein, M. W. Jones, M. O'Sullivan, R. M. Andrew, J. Hauck, G. P. Peters, *et al.*, "Global Carbon Budget 2019," *Earth System Science Data*, vol. 11, pp. 1783-1838, Dec 4 2019.
- [2] N. Jones. (2017, How the World Passed a Carbon Threshold and Why It Matters. Available: <https://e360.yale.edu/features/how-the-world-passed-a-carbon-threshold-400ppm-and-why-it-matters>
- [3] EIA. ANNUAL ENERGY OUTLOOK 2020 with projections to 2050 [Online]. Available: <https://www.eia.gov/outlooks/aeo/index.php>
- [4] R. Harris. (2012, Could Cheap Gas Slow Growth of Renewable Energy? Available: <https://www.npr.org/2012/02/02/146297284/could-cheap-gas-slow-growth-of-renewable-energy>
- [5] D. o. Energy. (2017, SunShot 2030 - New Solar Opportunities for a New Decade. Available: <https://www.energy.gov/eere/solar/sunshot-2030>
- [6] G. Thomas, "Overview of storage development DOE hydrogen program," 2000.
- [7] G. V. Research. (2020, Hydrogen Generation Market Size, Share | Global Industry Report, 2020-2027. Available: <https://www.grandviewresearch.com/industry-analysis/hydrogen-generation-market>
- [8] M. R. Firm. (2018, Hydrogen Generation Market. Available: <https://www.marketsandmarkets.com/Market-Reports/hydrogen-generation-market-494.html>
- [9] K. Alexander, "Technology roadmap: hydrogen and fuel cells," Technical report, International Energy Agency 2015.
- [10] F. C. T. Office. (2020, Hydrogen Production Pathways. Available: <https://www.energy.gov/eere/fuelcells/hydrogen-production-pathways>
- [11] R. Moliner, M. J. Lazaro, and I. Suelves, "Analysis of the strategies for bridging the gap towards the Hydrogen Economy," *International Journal of Hydrogen Energy*, vol. 41, pp. 19500-19508, Nov 16 2016.
- [12] Z. Chen, H. N. Dinh, and E. Miller, *Photoelectrochemical water splitting : standards, experimental methods, and protocols*. New York: Springer, 2013.
- [13] S. J. Sweeney and J. Mukherjee, "Optoelectronic Devices and Materials," in *Springer Handbook of Electronic and Photonic Materials*, S. Kasap and P. Capper, Eds., ed Cham: Springer International Publishing, 2017, pp. 1-1.
- [14] S. Mokkaapati and C. Jagadish, "III-V compound SC for optoelectronic devices," *Materials Today*, vol. 12, pp. 22-32, Apr 2009.
- [15] B. Giri, M. Masroor, T. Yan, K. Kushnir, A. D. Carl, C. Doiron, *et al.*, "Balancing Light Absorption and Charge Transport in Vertical SnS₂ Nanoflake Photoanodes with Stepped Layers and Large Intrinsic Mobility," *Advanced Energy Materials*, vol. 9, p. 1901236, 2019.
- [16] K. S. Novoselov, A. K. Geim, S. V. Morozov, D. Jiang, Y. Zhang, S. V. Dubonos, *et al.*, "Electric field effect in atomically thin carbon films," *Science*, vol. 306, pp. 666-669, Oct 22 2004.
- [17] C. H. Gong, Y. X. Zhang, W. Chen, J. W. Chu, T. Y. Lei, J. R. Pu, *et al.*, "Electronic and Optoelectronic Applications Based on 2D Novel Anisotropic Transition Metal Dichalcogenides," *Advanced Science*, vol. 4, Dec 2017.
- [18] Abid, P. Sehwat, S. S. Islam, P. Mishra, and S. Ahmad, "Reduced graphene oxide (rGO) based wideband optical sensor and the role of Temperature, Defect States and Quantum Efficiency," *Scientific Reports*, vol. 8, Feb 23 2018.
- [19] M. Coros, F. Pogacean, L. Magerusan, C. Socaci, and S. Pruneanu, "A brief overview on synthesis and applications of graphene and graphene-based nanomaterials," *Frontiers of Materials Science*, vol. 13, pp. 23-32, Mar 2019.
- [20] N. A. A. Ghany, S. A. Elsherif, and H. T. Handal, "Revolution of Graphene for different applications: State-of-the-art," *Surfaces and Interfaces*, vol. 9, pp. 93-106, Dec 2017.
- [21] R. F. Service, "Beyond Graphene," *Science*, vol. 348, pp. 490-492, May 1 2015.
- [22] F. Schwierz, "Graphene transistors," *Nature Nanotechnology*, vol. 5, pp. 487-496, Jul 2010.
- [23] S. G. Patil and R. H. Tredgold, "Electrical and Photoconductive Properties of SnS₂ Crystals," *Journal of Physics D-Applied Physics*, vol. 4, pp. 718-&, 1971.
- [24] A. Katty, B. Fotouhi, and O. Gorochoy, "Photoelectrochemical Study of SnS₂ in Aqueous-Solution," *Journal of the Electrochemical Society*, vol. 131, pp. 2806-2810, 1984.
- [25] L. Sharp, D. Soltz, and B. A. Parkinson, "Growth and characterization of tin disulfide single crystals," *Crystal Growth & Design*, vol. 6, pp. 1523-1527, Jun 2006.

- [26] B. Thangaraju and P. Kaliannan, "Spray pyrolytic deposition and characterization of SnS and SnS₂ thin films," *Journal of Physics D-Applied Physics*, vol. 33, pp. 1054-1059, May 7 2000.
- [27] C. W. Shi, P. F. Yang, M. Yao, X. Y. Dai, and Z. Chen, "Preparation of SnS₂ thin films by close-spaced sublimation at different source temperatures," *Thin Solid Films*, vol. 534, pp. 28-31, May 1 2013.
- [28] T. Shibata, Y. Muranushi, T. Miura, and T. Kishi, "Electrical Characterization of 2h-SnS₂ Single-Crystals Synthesized by the Low-Temperature Chemical Vapor Transport Method," *Journal of Physics and Chemistry of Solids*, vol. 52, pp. 551-553, 1991.
- [29] Y. Huang, E. Sutter, J. T. Sadowski, M. Cotlet, O. L. A. Monti, D. A. Racke, *et al.*, "Tin Disulfide-An Emerging Layered Metal Dichalcogenide Semiconductor: Materials Properties and Device Characteristics," *Acs Nano*, vol. 8, pp. 10743-10755, Oct 2014.
- [30] A. Shafique, A. Samad, and Y. H. Shin, "Ultra low lattice thermal conductivity and high carrier mobility of monolayer SnS₂ and SnSe₂: a first principles study," *Physical Chemistry Chemical Physics*, vol. 19, pp. 20677-20683, Aug 21 2017.
- [31] B. Ram and A. K. Singh, "Strain-induced indirect-to-direct band-gap transition in bulk SnS₂," *Physical Review B*, vol. 95, Feb 21 2017.
- [32] B. Sainbileg and M. Hayashi, "Possible indirect to direct bandgap transition in SnS₂ via nickel doping," *Chemical Physics*, vol. 522, pp. 59-64, Jun 1 2019.
- [33] Y. F. Sun, H. Cheng, S. Gao, Z. H. Sun, Q. H. Liu, Q. Liu, *et al.*, "Freestanding Tin Disulfide Single-Layers Realizing Efficient Visible-Light Water Splitting," *Angewandte Chemie - International Edition*, vol. 51, pp. 8727-8731, 2012.
- [34] G. X. Su, V. G. Hadjiev, P. E. Loya, J. Zhang, S. D. Lei, S. Maharjan, *et al.*, "Chemical Vapor Deposition of Thin Crystals of Layered Semiconductor SnS₂ for Fast Photodetection Application," *Nano Letters*, vol. 15, pp. 506-513, Jan 2015.
- [35] Z. Y. Qin, K. Xu, H. C. Yue, H. Wang, J. Zhang, C. Ouyang, *et al.*, "Enhanced room-temperature NH₃ gas sensing by 2D SnS₂ with sulfur vacancies synthesized by chemical exfoliation," *Sensors and Actuators B-Chemical*, vol. 262, pp. 771-779, Jun 1 2018.
- [36] Y. H. Kim, D. T. Phan, S. Ahn, K. H. Nam, C. M. Park, and K. J. Jeon, "Two-dimensional SnS₂ materials as high-performance NO₂ sensors with fast response and high sensitivity," *Sensors and Actuators B-Chemical*, vol. 255, pp. 616-621, Feb 2018.
- [37] L. D. Bharatula, M. B. Erande, I. S. Mulla, C. S. Rout, and D. J. Late, "SnS₂ nanoflakes for efficient humidity and alcohol sensing at room temperature," *Rsc Advances*, vol. 6, pp. 105421-105427, 2016.
- [38] Y. X. Li, S. G. Leonardi, A. Bonavita, G. Neri, and W. Wlodarski, "Two-Dimensional (2D) SnS₂-based Oxygen Sensor," *Proceedings of the 30th Anniversary Eurosenors Conference - Eurosenors 2016*, vol. 168, pp. 1102-1105, 2016.
- [39] J. Xia, D. D. Zhu, L. Wang, B. Huang, X. Huang, and X. M. Meng, "Large-Scale Growth of Two-Dimensional SnS₂ Crystals Driven by Screw Dislocations and Application to Photodetectors," *Advanced Functional Materials*, vol. 25, pp. 4255-4261, Jul 15 2015.
- [40] M. Liu, J. Y. Yang, Q. L. Qu, P. W. Zhu, and W. X. Li, "High-quality SnO₂@SnS₂ core-shell heterojunctions: Designed construction, mechanism and photovoltaic applications," *Journal of Power Sources*, vol. 273, pp. 848-856, Jan 1 2015.
- [41] B. A. Parkinson, "Dye sensitization of van der Waals surfaces of tin disulfide photoanodes," *Langmuir*, vol. 4, pp. 967-976, 1988/07/01 1988.
- [42] B. Yang, X. Q. Zuo, H. J. Xiao, L. Zhou, X. Yang, G. Li, *et al.*, "SnS₂ as low-cost counter-electrode materials for dye-sensitized solar cells," *Materials Letters*, vol. 133, pp. 197-199, Oct 15 2014.
- [43] E. Zhao, L. Gao, S. Yang, L. Wang, J. Cao, and T. Ma, "In situ fabrication of 2D SnS₂ nanosheets as a new electron transport layer for perovskite solar cells," *Nano Research*, June 08 2018.
- [44] G. Liu, Y. Qiu, Z. Wang, J. Zhang, X. Chen, M. Dai, *et al.*, "Efficiently Synergistic Hydrogen Evolution Realized by Trace Amount of Pt-Decorated Defect-Rich SnS₂ Nanosheets," *ACS Appl Mater Interfaces*, vol. 9, pp. 37750-37759, Nov 1 2017.
- [45] X. Y. Chia, P. Lazar, Z. Sofer, J. Luxa, and M. Pumera, "Layered SnS versus SnS₂: Valence and Structural implications on Electrochemistry and Clean Energy Electrocatalysis," *Journal of Physical Chemistry C*, vol. 120, pp. 24098-24111, Oct 27 2016.
- [46] K. Wu, C. J. Wu, C. M. Tseng, J. K. Chang, and T. C. Lee, "Structure-mediated electrochemical performance of SnS₂ anode for Li-ion batteries," *Journal of the Taiwan Institute of Chemical Engineers*, vol. 66, pp. 292-300, Sep 2016.

- [47] R. Thangavel, A. S. Pandian, H. V. Ramasamy, and Y. S. Lee, "Rapidly Synthesized, Few-Layered Pseudocapacitive SnS₂ Anode for High-Power Sodium Ion Batteries," *Acs Applied Materials & Interfaces*, vol. 9, pp. 40187-40196, Nov 22 2017.
- [48] L. A. Burton, T. J. Whittles, D. Hesp, W. M. Linhart, J. M. Skelton, B. Hou, *et al.*, "Electronic and optical properties of single crystal SnS₂: an earth-abundant disulfide photocatalyst," *Journal of Materials Chemistry A*, vol. 4, pp. 1312-1318, 2016.
- [49] T. F. Jaramillo, K. P. Jorgensen, J. Bonde, J. H. Nielsen, S. Horch, and I. Chorkendorff, "Identification of active edge sites for electrochemical H₂ evolution from MoS₂ nanocatalysts," *Science*, vol. 317, pp. 100-102, Jul 6 2007.
- [50] C. G. Morales-Guio, L. A. Stern, and X. L. Hu, "Nanostructured hydrotreating catalysts for electrochemical hydrogen evolution," *Chemical Society Reviews*, vol. 43, pp. 6555-6569, Sep 21 2014.
- [51] I. C. Man, H. Y. Su, F. Calle-Vallejo, H. A. Hansen, J. I. Martinez, N. G. Inoglu, *et al.*, "Universality in Oxygen Evolution Electrocatalysis on Oxide Surfaces," *Chemcatchem*, vol. 3, pp. 1159-1165, Jul 2011.
- [52] Z. W. Seh, J. Kibsgaard, C. F. Dickens, I. B. Chorkendorff, J. K. Nørskov, and T. F. Jaramillo, "Combining theory and experiment in electrocatalysis: Insights into materials design," *Science*, vol. 355, Jan 13 2017.
- [53] (2018, Top 10 most expensive metals in the world. Available: <https://www.ecstasycoffee.com/top-10-expensive-metals-world/>)
- [54] C. C. L. McCrory, S. H. Jung, J. C. Peters, and T. F. Jaramillo, "Benchmarking Heterogeneous Electrocatalysts for the Oxygen Evolution Reaction," *Journal of the American Chemical Society*, vol. 135, pp. 16977-16987, Nov 13 2013.
- [55] L. C. Seitz, Z. B. Chen, A. J. Forman, B. A. Pinaud, J. D. Benck, and T. F. Jaramillo, "Modeling Practical Performance Limits of Photoelectrochemical Water Splitting Based on the Current State of Materials Research," *Chemsuschem*, vol. 7, pp. 1372-1385, May 2014.
- [56] J. M. Spurgeon, M. G. Walter, J. F. Zhou, P. A. Kohl, and N. S. Lewis, "Electrical conductivity, ionic conductivity, optical absorption, and gas separation properties of ionically conductive polymer membranes embedded with Si microwire arrays," *Energy & Environmental Science*, vol. 4, pp. 1772-1780, May 2011.
- [57] B. A. Pinaud, J. D. Benck, L. C. Seitz, A. J. Forman, Z. B. Chen, T. G. Deutsch, *et al.*, "Technical and economic feasibility of centralized facilities for solar hydrogen production via photocatalysis and photoelectrochemistry," *Energy & Environmental Science*, vol. 6, pp. 1983-2002, Jul 2013.
- [58] B. D. Alexander, P. J. Kulesza, I. Rutkowska, R. Solarska, and J. Augustynski, "Metal oxide photoanodes for solar hydrogen production," *Journal of Materials Chemistry*, vol. 18, pp. 2298-2303, May 28 2008.
- [59] L. Ji, M. D. McDaniel, S. J. Wang, A. B. Posadas, X. H. Li, H. Y. Huang, *et al.*, "A silicon-based photocathode for water reduction with an epitaxial SrTiO₃ protection layer and a nanostructured catalyst," *Nature Nanotechnology*, vol. 10, pp. 84-90, Jan 2015.
- [60] A. A. Dubale, C. J. Pan, A. G. Tamirat, H. M. Chen, W. N. Su, C. H. Chen, *et al.*, "Heterostructured Cu₂O/CuO decorated with nickel as a highly efficient photocathode for photoelectrochemical water reduction," *Journal of Materials Chemistry A*, vol. 3, pp. 12482-12499, 2015.
- [61] L. Q. Ye, Y. Deng, L. Wang, H. Q. Xie, and F. Y. Su, "Bismuth-Based Photocatalysts for Solar Photocatalytic Carbon Dioxide Conversion," *Chemsuschem*, Jul 24 2019.
- [62] S. Sreeja and K. V. Shetty, "Photocatalytic water disinfection under solar irradiation by Ag@TiO₂ core-shell structured nanoparticles," *Solar Energy*, vol. 157, pp. 236-243, Nov 15 2017.
- [63] J. Benson, M. Li, S. Wang, P. Wang, and P. Papakonstantinou, "Electrocatalytic Hydrogen Evolution Reaction on Edges of a Few Layer Molybdenum Disulfide Nanodots," *ACS Appl Mater Interfaces*, vol. 7, pp. 14113-22, Jul 1 2015.
- [64] J. Kibsgaard and T. F. Jaramillo, "Molybdenum phosphosulfide: an active, acid-stable, earth-abundant catalyst for the hydrogen evolution reaction," *Angew Chem Int Ed Engl*, vol. 53, pp. 14433-7, Dec 22 2014.
- [65] G. Boschloo and A. Hagfeldt, "Characteristics of the Iodide/Triiodide Redox Mediator in Dye-Sensitized Solar Cells," *Accounts of Chemical Research*, vol. 42, pp. 1819-1826, Nov 2009.
- [66] C. R. Jiang, S. J. A. Moniz, A. Q. Wang, T. Zhang, and J. W. Tang, "Photoelectrochemical devices for solar water splitting - materials and challenges," *Chemical Society Reviews*, vol. 46, pp. 4645-4660, Aug 7 2017.
- [67] T. J. Jacobsson, V. Fjallstrom, M. Sahlberg, M. Edoff, and T. Edvinsson, "A monolithic device for solar water splitting based on series interconnected thin film absorbers reaching over 10% solar-to-hydrogen efficiency," *Energy & Environmental Science*, vol. 6, pp. 3676-3683, Dec 2013.

- [68] S. Licht, B. Wang, S. Mukerji, T. Soga, M. Umeno, and H. Tributsch, "Efficient solar water splitting, exemplified by RuO₂-catalyzed AlGaAs/Si photoelectrolysis," *Journal of Physical Chemistry B*, vol. 104, pp. 8920-8924, Sep 28 2000.
- [69] Y. G. Li, Y. L. Li, B. S. Sa, and R. Ahuja, "Review of two-dimensional materials for photocatalytic water splitting from a theoretical perspective," *Catalysis Science & Technology*, vol. 7, pp. 545-559, Feb 7 2017.
- [70] M. Faraji, M. Yousefi, S. Yousefzadeh, M. Zirak, N. Naseri, T. H. Jeon, *et al.*, "Two-dimensional materials in semiconductor photoelectrocatalytic systems for water splitting," *Energy & Environmental Science*, vol. 12, pp. 59-95, Jan 1 2019.
- [71] L. Jia, D. H. Wang, Y. X. Huang, A. W. Xu, and H. Q. Yu, "Highly Durable N-Doped Graphene/CdS Nanocomposites with Enhanced Photocatalytic Hydrogen Evolution from Water under Visible Light Irradiation," *Journal of Physical Chemistry C*, vol. 115, pp. 11466-11473, Jun 16 2011.
- [72] U. Sim, T. Y. Yang, J. Moon, J. An, J. Hwang, J. H. Seo, *et al.*, "N-doped monolayer graphene catalyst on silicon photocathode for hydrogen production," *Energy & Environmental Science*, vol. 6, pp. 3658-3664, Dec 2013.
- [73] F. Yang, V. Kuznetsov, M. Lublow, C. Merschjann, A. Steigert, J. Klaer, *et al.*, "Solar hydrogen evolution using metal-free photocatalytic polymeric carbon nitride/CuInS₂ composites as photocathodes," *Journal of Materials Chemistry A*, vol. 1, pp. 6407-6415, 2013.
- [74] J. D. Benck, T. R. Hellstern, J. Kibsgaard, P. Chakhranont, and T. F. Jaramillo, "Catalyzing the Hydrogen Evolution Reaction (HER) with Molybdenum Sulfide Nanomaterials," *Acs Catalysis*, vol. 4, pp. 3957-3971, Nov 2014.
- [75] U. Maitra, U. Gupta, M. De, R. Datta, A. Govindaraj, and C. N. R. Rao, "Highly Effective Visible-Light-Induced H₂ Generation by Single-Layer 1T-MoS₂ and a Nanocomposite of Few-Layer 2H-MoS₂ with Heavily Nitrogenated Graphene," *Angewandte Chemie-International Edition*, vol. 52, pp. 13057-13061, Dec 2 2013.
- [76] L. F. Wu, A. J. F. van Hoof, N. Y. Dzade, L. Gao, M. I. Richard, H. Friedrich, *et al.*, "Enhancing the electrocatalytic activity of 2H-WS₂ for hydrogen evolution via defect engineering," *Physical Chemistry Chemical Physics*, vol. 21, pp. 6071-6079, Mar 21 2019.
- [77] B. Mahler, V. Hoepfner, K. Liao, and G. A. Ozin, "Colloidal Synthesis of 1T-WS₂ and 2H-WS₂ Nanosheets: Applications for Photocatalytic Hydrogen Evolution," *Journal of the American Chemical Society*, vol. 136, pp. 14121-14127, Oct 8 2014.
- [78] F. M. Pesci, M. S. Sokolikova, C. Grotta, P. C. Sherrell, F. Reale, K. Sharda, *et al.*, "MoS₂/WS₂ Heterojunction for Photoelectrochemical Water Oxidation," *Acs Catalysis*, vol. 7, pp. 4990-4998, Aug 2017.
- [79] G. B. Liu, Z. H. Li, T. Hasan, X. S. Chen, W. Zheng, W. Feng, *et al.*, "Vertically aligned two-dimensional SnS₂ nanosheets with a strong photon capturing capability for efficient photoelectrochemical water splitting," *Journal of Materials Chemistry A*, vol. 5, pp. 1989-1995, Feb 7 2017.
- [80] M. Gong, Y. G. Li, H. L. Wang, Y. Y. Liang, J. Z. Wu, J. G. Zhou, *et al.*, "An Advanced Ni-Fe Layered Double Hydroxide Electrocatalyst for Water Oxidation," *Journal of the American Chemical Society*, vol. 135, pp. 8452-8455, Jun 12 2013.
- [81] L. Lv, Z. X. Yang, K. Chen, C. D. Wang, and Y. J. Xiong, "2D Layered Double Hydroxides for Oxygen Evolution Reaction: From Fundamental Design to Application," *Advanced Energy Materials*, vol. 9, May 2019.
- [82] G. L. Ye, Y. J. Gong, J. H. Lin, B. Li, Y. M. He, S. T. Pantelides, *et al.*, "Defects Engineered Monolayer MoS₂ for Improved Hydrogen Evolution Reaction," *Nano Letters*, vol. 16, pp. 1097-1103, Feb 2016.
- [83] C. Tsai, H. Li, S. Park, J. Park, H. S. Han, J. K. Norskov, *et al.*, "Electrochemical generation of sulfur vacancies in the basal plane of MoS₂ for hydrogen evolution," *Nature Communications*, vol. 8, Apr 21 2017.
- [84] G. Q. Li, D. Zhang, Q. Qiao, Y. F. Yu, D. Peterson, A. Zafar, *et al.*, "All The Catalytic Active Sites of MoS₂ for Hydrogen Evolution," *Journal of the American Chemical Society*, vol. 138, pp. 16632-16638, Dec 28 2016.
- [85] D. Z. Wang, Y. Y. Xie, and Z. Z. Wu, "Amorphous phosphorus-doped MoS₂ catalyst for efficient hydrogen evolution reaction," *Nanotechnology*, vol. 30, May 17 2019.
- [86] Z. Z. Cheng, F. M. Wang, T. A. Shifa, K. L. Liu, Y. Huang, Q. L. Liu, *et al.*, "Carbon dots decorated vertical SnS₂ nanosheets for efficient photocatalytic oxygen evolution," *Applied Physics Letters*, vol. 109, Aug 1 2016.

- [87] J. D. Meindl, Q. Chen, and J. A. Davis, "Limits on silicon nanoelectronics for terascale integration," *Science*, vol. 293, pp. 2044-2049, Sep 14 2001.
- [88] H. Schmidt, S. F. Wang, L. Q. Chu, M. Toh, R. Kumar, W. J. Zhao, *et al.*, "Transport Properties of Monolayer MoS₂ Grown by Chemical Vapor Deposition," *Nano Letters*, vol. 14, pp. 1909-1913, Apr 2014.
- [89] S. Kurabayashia and K. Nagashio, "Transport properties of the top and bottom surfaces in monolayer MoS₂ grown by chemical vapor deposition," *Nanoscale*, vol. 9, pp. 13264-13271, Sep 21 2017.
- [90] J. Wu, H. Li, Z. Y. Yin, H. Li, J. Q. Liu, X. H. Cao, *et al.*, "Layer Thinning and Etching of Mechanically Exfoliated MoS₂ Nanosheets by Thermal Annealing in Air," *Small*, vol. 9, pp. 3314-3319, Oct 11 2013.
- [91] M. Okada, T. Sawazaki, K. Watanabe, T. Taniguch, H. Hibino, H. Shinohara, *et al.*, "Direct Chemical Vapor Deposition Growth of WS₂ Atomic Layers on Hexagonal Boron Nitride," *Acs Nano*, vol. 8, pp. 8273-8277, Aug 2014.
- [92] Y. F. Sun, H. Cheng, S. Gao, Z. H. Sun, Q. H. Liu, Q. Liu, *et al.*, "Freestanding Tin Disulfide Single-Layers Realizing Efficient Visible-Light Water Splitting," *Angewandte Chemie-International Edition*, vol. 51, pp. 8727-8731, 2012.
- [93] Y. H. Chang, W. Zhang, Y. Zhu, Y. Han, J. Pu, J. K. Chang, *et al.*, "Monolayer MoSe₂ Grown by Chemical Vapor Deposition for Fast Photodetection," *Acs Nano*, vol. 8, pp. 8582-8590, Aug 2014.
- [94] B. V. Zeghbrock. (2011, April 15, 2020). Chapter 3: Metal Semiconductor Junctions. Available: https://ecee.colorado.edu/~bart/book/book/chapter3/ch3_4.htm
- [95] G. M. Ali, "Fabrication Of ZnO Based MSM Photodetectors," 2020.
- [96] P. R. Berger, "MSM photodiodes," *IEEE Potentials*, vol. 15, pp. 25-29, 1996.
- [97] T. Nakotte, H. Luo, and J. Pietryga, "PbE (E = S, Se) Colloidal Quantum Dot-Layered 2D Material Hybrid Photodetectors," *Nanomaterials (Basel)*, vol. 10, Jan 19 2020.
- [98] L. Gao, C. Chen, K. Zeng, C. Ge, D. Yang, H. S. Song, *et al.*, "Broadband, sensitive and spectrally distinctive SnS₂ nanosheet/PbS colloidal quantum dot hybrid photodetector," *Light-Science & Applications*, vol. 5, Jul 2016.
- [99] Y. P. Dan, X. Y. Zhao, K. X. Chen, and A. Mesli, "A Photoconductor Intrinsically Has No Gain," *Acs Photonics*, vol. 5, pp. 4111-4116, Oct 2018.
- [100] X. Li, J. E. Carey, J. W. Sickler, M. U. Pralle, C. Palsule, and C. J. Vineis, "Silicon photodiodes with high photoconductive gain at room temperature," *Optics Express*, vol. 20, pp. 5518-5523, Feb 27 2012.
- [101] K. Thakar and S. Lodha, "Optoelectronic and photonic devices based on transition metal dichalcogenides," *Materials Research Express*, vol. 7, Jan 2020.
- [102] A. De Sanctis, J. D. Mehew, M. F. Craciun, and S. Russo, "Graphene-Based Light Sensing: Fabrication, Characterisation, Physical Properties and Performance," *Materials*, vol. 11, Sep 2018.
- [103] J. L. Wang, H. H. Fang, X. D. Wang, X. S. Chen, W. Lu, and W. D. Hu, "Recent Progress on Localized Field Enhanced Two-dimensional Material Photodetectors from Ultraviolet-Visible to Infrared," *Small*, vol. 13, Sep 20 2017.
- [104] M. Buscema, J. O. Island, D. J. Groenendijk, S. I. Blanter, G. A. Steele, H. S. J. van der Zant, *et al.*, "Photocurrent generation with two-dimensional van der Waals semiconductors," *Chemical Society Reviews*, vol. 44, pp. 3691-3718, 2015.
- [105] M. J. Grotevent, C. U. Hail, S. Yakunin, D. N. Dirin, K. Thodkar, G. Borin Barin, *et al.*, "Nanoprinted Quantum Dot-Graphene Photodetectors," *Advanced Optical Materials*, vol. 7, p. 1900019, 2019.
- [106] D. Kufer, I. Nikitskiy, T. Lasanta, G. Navickaite, F. H. L. Koppens, and G. Konstantatos, "Hybrid 2D-0D MoS₂-PbS Quantum Dot Photodetectors," *Advanced Materials*, vol. 27, pp. 176-180, Jan 2015.
- [107] Y. Yu, Y. T. Zhang, X. X. Song, H. T. Zhang, M. X. Cao, Y. L. Che, *et al.*, "PbS-Decorated WS₂ Phototransistors with Fast Response," *Acs Photonics*, vol. 4, pp. 950-956, Apr 2017.
- [108] X. Zhou, X. Z. Hu, S. S. Zhou, H. Y. Song, Q. Zhang, L. J. Pi, *et al.*, "Tunneling Diode Based on WSe₂/SnS₂ Heterostructure Incorporating High Detectivity and Responsivity," *Advanced Materials*, vol. 30, Feb 15 2018.
- [109] K. Zhang, X. Fang, Y. L. Wang, Y. Wan, Q. J. Song, W. H. Zhai, *et al.*, "Ultrasensitive Near-Infrared Photodetectors Based on a Graphene-MoTe₂-Graphene Vertical van der Waals Heterostructure," *Acs Applied Materials & Interfaces*, vol. 9, pp. 5392-5398, Feb 15 2017.
- [110] O. Lopez-Sanchez, D. Lembke, M. Kayci, A. Radenovic, and A. Kis, "Ultrasensitive photodetectors based on monolayer MoS₂," *Nature Nanotechnology*, vol. 8, pp. 497-501, Jul 2013.
- [111] B. Rahmati, I. Hajzadeh, R. Karimzadeh, and S. M. Mohseni, "Facile, scalable and transfer free vertical-MoS₂ nanostructures grown on Au/SiO₂ patterned electrode for photodetector application," *Applied Surface Science*, vol. 455, pp. 876-882, Oct 15 2018.

- [112] T. R. Hellstern, J. D. Benck, J. Kibsgaard, C. Hahn, and T. F. Jaramillo, "Engineering Cobalt Phosphide (CoP) Thin Film Catalysts for Enhanced Hydrogen Evolution Activity on Silicon Photocathodes," *Advanced Energy Materials*, vol. 6, Feb 18 2016.
- [113] Gurudayal, P. S. Bassi, T. Sritharan, and L. H. Wong, "Recent progress in iron oxide based photoanodes for solar water splitting," *Journal of Physics D-Applied Physics*, vol. 51, Nov 28 2018.
- [114] X. Z. Xu, Z. H. Zhang, J. C. Dong, D. Yi, J. J. Niu, M. H. Wu, *et al.*, "Ultrafast epitaxial growth of metre-sized single-crystal graphene on industrial Cu foil," *Science Bulletin*, vol. 62, pp. 1074-1080, Aug 15 2017.
- [115] F. Mitsuhashi, M. Okada, Y. Tateno, T. Nakabayashi, M. Ueno, H. Nagasawa, *et al.*, "Extremely uniform epitaxial growth of graphene from sputtered SiC films on SiC substrates," *Mrs Advances*, vol. 2, pp. 51-56, 2017.
- [116] A. Chaturvedi, V. Aravindan, P. Hu, R. R. Prabhakar, L. H. Wong, C. Kloc, *et al.*, "Synthesis of SnS₂ single crystals and its Li-storage performance with LiMn₂O₄ cathode," *Applied Materials Today*, vol. 5, pp. 68-72, Dec 2016.
- [117] A. Jawaid, D. Nepal, K. Park, M. Jespersen, A. Qualley, P. Mirau, *et al.*, "Mechanism for Liquid Phase Exfoliation of MoS₂," *Chemistry of Materials*, vol. 28, pp. 337-348, Jan 12 2016.
- [118] B. Adilbekova, Y. Lin, E. Yengel, H. Faber, G. Harrison, Y. Firdaus, *et al.*, "Liquid phase exfoliation of MoS₂ and WS₂ in aqueous ammonia and their application in highly efficient organic solar cells," *Journal of Materials Chemistry C*, vol. 8, pp. 5259-5264, 2020.
- [119] K. Kang, S. E. Xie, L. J. Huang, Y. M. Han, P. Y. Huang, K. F. Mak, *et al.*, "High-mobility three-atom-thick semiconducting films with wafer-scale homogeneity," *Nature*, vol. 520, pp. 656-660, Apr 30 2015.
- [120] M. Mattinen, P. J. King, L. Khriachtchev, K. Meinander, J. T. Gibbon, V. R. Dhanak, *et al.*, "Low-Temperature Wafer-Scale Deposition of Continuous 2D SnS₂ Films," *Small*, vol. 14, May 24 2018.
- [121] K. Kang, K. H. Lee, Y. M. Han, H. Gao, S. E. Xie, D. A. Muller, *et al.*, "Layer-by-layer assembly of two-dimensional materials into wafer-scale heterostructures," *Nature*, vol. 550, pp. 229-233, Oct 12 2017.
- [122] G. R. Bhimanapati, Z. Lin, V. Meunier, Y. Jung, J. Cha, S. Das, *et al.*, "Recent Advances in Two-Dimensional Materials beyond Graphene," *Acs Nano*, vol. 9, pp. 11509-11539, Dec 2015.
- [123] D. Chu and E. K. Kim, "Recent Advances in Synthesis and Assembly of van der Waals Materials," *Journal of the Korean Physical Society*, vol. 73, pp. 805-816, Sep 2018.
- [124] L. A. Burton, D. Colombara, R. D. Abellon, F. C. Grozema, L. M. Peter, T. J. Savenije, *et al.*, "Synthesis, Characterization, and Electronic Structure of Single-Crystal SnS, Sn₂S₃, and SnS₂," *Chemistry of Materials*, vol. 25, pp. 4908-4916, Dec 24 2013.
- [125] M. Khadraoui, R. Miloua, N. Benramdane, A. Bouzidi, and K. Sahraoui, "Synthesis and characterization of (Sn₂S₃)_x(Bi₂S₃)_(1-x) composite thin films for solar cell applications," *Materials Chemistry and Physics*, vol. 169, pp. 40-46, Feb 1 2016.
- [126] R. Godoy-Rosas, S. Barraza-Felix, R. Ramirez-Bon, R. Ochoa-Landin, H. A. Pineda-Leon, M. Flores-Acosta, *et al.*, "SYNTHESIS AND CHARACTERIZATION OF Sn₂S₃ AS NANOPARTICLES, POWDERS AND THIN FILMS, USING SOFT CHEMISTRY REACTIONS," *Chalcogenide Letters*, vol. 14, pp. 365-371, Sep 2017.
- [127] M. Khadraoui, N. Benramdane, C. Mathieu, A. Bouzidi, R. Miloua, Z. Kebbab, *et al.*, "Optical and electrical properties of Sn₂S₃ thin films grown by spray pyrolysis," *Solid State Communications*, vol. 150, pp. 297-300, Jan 2010.
- [128] W. D. Shi, L. H. Huo, H. S. Wang, H. J. Zhang, J. H. Yang, and P. H. Wei, "Hydrothermal growth and gas sensing property of flower-shaped SnS₂ nanostructures," *Nanotechnology*, vol. 17, pp. 2918-2924, Jun 28 2006.
- [129] R. Etefagh, M. Alizade, R. Radfar, E. Azhir, N. Shahtahmasebi, and E. Tabasi, "Fabrication and characterization of SnO₂ and SnS₂ nanobiosensor in the Presence of Aspergillus Niger Fungi," *Nanomedicine Research Journal*, vol. 4, pp. 35-39, 2019.
- [130] A. Voznyi, V. Kosyak, A. Opanasyuk, N. Tirkusova, L. Grase, A. Medvids, *et al.*, "Structural and electrical properties of SnS₂ thin films," *Materials Chemistry and Physics*, vol. 173, pp. 52-61, Apr 15 2016.
- [131] Y. P. Gnatenko, P. M. Bukivskij, A. S. Opanasyuk, D. I. Kurbatov, M. M. Kolesnyk, V. V. Kosyak, *et al.*, "Low-temperature photoluminescence of II-VI films obtained by close-spaced vacuum sublimation," *Journal of Luminescence*, vol. 132, pp. 2885-2888, Nov 2012.
- [132] V. Kosyak, A. Opanasyuk, P. M. Bukivskij, and Y. P. Gnatenko, "Study of the structural and photoluminescence properties of CdTe polycrystalline films deposited by close-spaced vacuum sublimation," *Journal of Crystal Growth*, vol. 312, pp. 1726-1730, May 1 2010.

- [133] A. S. Opanasyuk, D. I. Kurbatov, V. V. Kosyak, S. I. Kshniakina, and S. N. Danilchenko, "Characteristics of structure formation in zinc and cadmium chalcogenide films deposited on nonorienting substrates," *Crystallography Reports*, vol. 57, pp. 927-933, Dec 2012.
- [134] M. Birkett, W. M. Linhart, J. Stoner, L. J. Phillips, K. Durose, J. Alaria, *et al.*, "Band gap temperature-dependence of close-space sublimation grown Sb₂Se₃ by photo-reflectance," *Apl Materials*, vol. 6, Aug 2018.
- [135] J. Britt and C. Ferekides, "Thin-Film Cds/Cdte Solar-Cell with 15.8-Percent Efficiency," *Applied Physics Letters*, vol. 62, pp. 2851-2852, May 31 1993.
- [136] J. D. Major and K. Durose, "Early stage growth mechanisms of CdTe thin films deposited by close space sublimation for solar cells," *Solar Energy Materials and Solar Cells*, vol. 95, pp. 3165-3170, Dec 2011.
- [137] O. Madelung, *Semiconductors: Data Handbook*, Third ed.: Springer Berlin Heidelberg, 2004.
- [138] J. Carper, "The CRC Handbook of Chemistry and Physics," *Library Journal*, vol. 124, pp. 192-+, Jun 1 1999.
- [139] C. R. Wang, K. B. Tang, Q. Yang, Y. T. Qian, and C. Y. Xu, "Hydrothermal synthesis and characterization of SnS₂ nanocrystals," *Chemistry Letters*, pp. 1294-1295, Dec 5 2001.
- [140] M. Li, E. Liu, H. Hu, S. Ouyang, H. Xu, and D. Wang, "Surfactant-Free Synthesis of Single Crystalline SnS₂ and Effect of Surface Atomic Structure on the Photocatalytic Property," *International Journal of Photoenergy*, vol. 2014, p. 394146, 2014/12/01 2014.
- [141] H. Li, H. Q. Wu, S. G. Yuan, and H. Qian, "Synthesis and characterization of vertically standing MoS₂ nanosheets," *Scientific Reports*, vol. 6, Feb 18 2016.
- [142] Y. Sun, H. Cheng, S. Gao, Z. Sun, Q. Liu, Q. Liu, *et al.*, "Innenteilbild: Freestanding Tin Disulfide Single-Layers Realizing Efficient Visible-Light Water Splitting (Angew. Chem. 35/2012)," *Angewandte Chemie*, vol. 124, pp. 8798-8798, 2012.
- [143] X. S. Jia, C. C. Tang, R. H. Pan, Y. Z. Long, C. Z. Gu, and J. J. Li, "Thickness-Dependently Enhanced Photodetection Performance of Vertically Grown SnS₂ Nanoflakes with Large Size and High Production," *Acs Applied Materials & Interfaces*, vol. 10, pp. 18073-18081, May 30 2018.
- [144] J. T. Li and N. Q. Wu, "Semiconductor-based photocatalysts and photoelectrochemical cells for solar fuel generation: a review," *Catalysis Science & Technology*, vol. 5, pp. 1360-1384, Mar 1 2015.
- [145] R. S. Mitchell, Y. Fujiki, and Y. Ishizawa, "Structural Polyttypism of Tin Disulfide - Its Relationship to Environments of Formation," *Journal of Crystal Growth*, vol. 57, pp. 273-279, 1982.
- [146] W. R. Gao, K. Zielinski, B. N. Drury, A. D. Carl, and R. L. Grimm, "Elucidation of Chemical Species and Reactivity at Methylammonium Lead Iodide and Cesium Tin Bromide Perovskite Surfaces via Orthogonal Reaction Chemistry," *Journal of Physical Chemistry C*, vol. 122, pp. 17882-17894, Aug 9 2018.
- [147] A. D. Carl, R. E. Kalan, J. D. Obayemi, M. G. Z. Kana, W. O. Soboyejo, and R. L. Grimm, "Synthesis and Characterization of Alkylamine-Functionalized Si(111) for Perovskite Adhesion With Minimal Interfacial Oxidation or Electronic Defects," *Acs Applied Materials & Interfaces*, vol. 9, pp. 34377-34388, Oct 4 2017.
- [148] K. Kushnir, K. F. Chen, L. T. Zhou, B. Giri, R. L. Grimm, P. M. Rao, *et al.*, "Dynamics of Photoexcited Carriers in Polycrystalline PbS and at PbS/ZnO Heterojunctions: Influence of Grain Boundaries and Interfaces," *Journal of Physical Chemistry C*, vol. 122, pp. 11682-11688, Jun 7 2018.
- [149] K. T. Butler, B. J. Dringoli, L. Zhou, P. M. Rao, A. Walsh, and L. V. Titov, "Ultrafast carrier dynamics in BiVO₄ thin film photoanode material: interplay between free carriers, trapped carriers and low-frequency lattice vibrations," *Journal of Materials Chemistry A*, vol. 4, pp. 18516-18523, Dec 21 2016.
- [150] D. D. Ebbing and S. D. Gammon, *General Chemistry*, 9th ed. New York, United States: Houghton Mifflin Company, 2009.
- [151] W. K. Burton and N. Cabrera, "Crystal growth and surface structure. Part I," *Discussions of the Faraday Society*, vol. 5, pp. 33-39, 1949.
- [152] N. Cabrera and W. K. Burton, "Crystal growth and surface structure. Part II," *Discussions of the Faraday Society*, vol. 5, pp. 40-48, 1949.
- [153] J. Lee, S. Pak, P. Giraud, Y. W. Lee, Y. Cho, J. Hong, *et al.*, "Thermodynamically Stable Synthesis of Large-Scale and Highly Crystalline Transition Metal Dichalcogenide Monolayers and their Unipolar n-n Heterojunction Devices," *Advanced Materials*, vol. 29, Sep 6 2017.
- [154] H. J. Xu, J. S. Mi, Y. Li, B. Zhang, R. D. Cong, G. S. Fu, *et al.*, "Nucleation mechanism and morphology evolution of MoS₂ flakes grown by chemical vapor deposition," *Chinese Physics B*, vol. 26, Dec 2017.
- [155] J. F. Xie, H. Zhang, S. Li, R. X. Wang, X. Sun, M. Zhou, *et al.*, "Defect-Rich MoS₂ Ultrathin Nanosheets with Additional Active Edge Sites for Enhanced Electrocatalytic Hydrogen Evolution," *Advanced Materials*, vol. 25, pp. 5807-+, Oct 2013.

- [156] A. J. Smith, P. E. Meek, and W. Y. Liang, "Raman-Scattering Studies of SnS₂ and SnSe₂," *Journal of Physics C-Solid State Physics*, vol. 10, pp. 1321-1333, 1977.
- [157] Y. B. Yang, J. K. Dash, A. J. Littlejohn, Y. Xiang, Y. Wang, J. Shi, *et al.*, "Large Single Crystal SnS₂ Flakes Synthesized from Coevaporation of Sn and S," *Crystal Growth & Design*, vol. 16, pp. 961-973, Feb 2016.
- [158] L. T. Zhou, C. Q. Zhao, B. Giri, P. Allen, X. W. Xu, H. Joshi, *et al.*, "High Light Absorption and Charge Separation Efficiency at Low Applied Voltage from Sb-Doped SnO₂/BiVO₄ Core/Shell Nanorod-Array Photoanodes," *Nano Letters*, vol. 16, pp. 3463-3474, Jun 2016.
- [159] P. U. Jepsen, D. G. Cooke, and M. Koch, "Terahertz spectroscopy and imaging—Modern techniques and applications," *Laser & Photonics Reviews*, vol. 5, pp. 124-166, 2011.
- [160] J. B. Baxter, C. Richter, and C. A. Schmuttenmaer, "Ultrafast Carrier Dynamics in Nanostructures for Solar Fuels," *Annual Review of Physical Chemistry*, Vol 65, vol. 65, pp. 423-447, 2014 2014.
- [161] K. P. Regan, C. Koenigsmann, S. W. Sheehan, S. J. Konezny, and C. A. Schmuttenmaer, "Size-Dependent Ultrafast Charge Carrier Dynamics of WO₃ for Photoelectrochemical Cells," *Journal of Physical Chemistry C*, vol. 120, pp. 14926-14933, Jul 14 2016.
- [162] K. T. Butler, B. J. Dringoli, L. Zhou, P. M. Rao, A. Walsh, and L. V. Titova, "Ultrafast carrier dynamics in BiVO₄ thin film photoanode material: interplay between free carriers, trapped carriers and low-frequency lattice vibrations," *Journal of Materials Chemistry A*, vol. 4, pp. 18516-18523, 2016.
- [163] K. Kushnir, K. Chen, L. Zhou, B. Giri, R. L. Grimm, P. M. Rao, *et al.*, "Dynamics of Photoexcited Carriers in Polycrystalline PbS and at PbS/ZnO Heterojunctions: Influence of Grain Boundaries and Interfaces," *The Journal of Physical Chemistry C*, vol. 122, pp. 11682-11688, 2018/06/07 2018.
- [164] L. V. Titova, T. L. Cocker, D. G. Cooke, X. Wang, A. Meldrum, and F. A. Hegmann, "Ultrafast percolative transport dynamics in silicon nanocrystal films (vol 83, 085403, 2011)," *Physical Review B*, vol. 83, Apr 15 2011.
- [165] J. B. Baxter and G. W. Guglietta, "Terahertz spectroscopy," *Anal Chem*, vol. 83, pp. 4342-68, Jun 15 2011.
- [166] J. B. Baxter and C. A. Schmuttenmaer, "Conductivity of ZnO nanowires, nanoparticles, and thin films using time-resolved terahertz spectroscopy," *Journal of Physical Chemistry B*, vol. 110, pp. 25229-25239, Dec 21 2006.
- [167] F. A. Hegmann, O. Ostroverkhova, and D. G. Cooke, "Probing Organic Semiconductors with Terahertz Pulses," in *Photophysics of Molecular Materials*, ed: Wiley-VCH Verlag GmbH & Co. KGaA, 2006, pp. 367-428.
- [168] N. Smith, "Classical generalization of the Drude formula for the optical conductivity," *Physical Review B*, vol. 64, 2001.
- [169] Z. Mics, A. D'Angio, S. A. Jensen, M. Bonn, and D. Turchinovich, "Density-dependent electron scattering in photoexcited GaAs in strongly diffusive regime," *Applied Physics Letters*, vol. 102, p. 231120, 2013.
- [170] C. A. Schmuttenmaer, "Exploring Dynamics in the Far-Infrared with Terahertz Spectroscopy," *Chemical Reviews*, vol. 104, pp. 1759-1780, 2004/04/01 2004.
- [171] J. R. Knab, X. Lu, F. A. Vallejo, G. Kumar, T. E. Murphy, and L. M. Hayden, "Ultrafast Carrier Dynamics and Optical Properties of Nanoporous Silicon at Terahertz Frequencies," *Optical Materials Express*, vol. 4, pp. 300-307, 2014/02/01 2014.
- [172] T. L. Cocker, D. Baillie, M. Buruma, L. V. Titova, R. D. Sydora, F. Marsiglio, *et al.*, "Microscopic origin of the Drude-Smith model," *Physical Review B*, vol. 96, p. 205439, 11/27/ 2017.
- [173] P. Parkinson, J. Lloyd-Hughes, Q. Gao, H. H. Tan, C. Jagadish, M. B. Johnston, *et al.*, "Transient Terahertz Conductivity of GaAs Nanowires," *Nano Letters*, vol. 7, pp. 2162-2165, 2007/07/01 2007.
- [174] D. G. Cooke, A. Meldrum, and P. Uhd Jepsen, "Ultrabroadband terahertz conductivity of Si nanocrystal films," *Applied Physics Letters*, vol. 101, p. 211107, 2012.
- [175] Q.-I. Zhou, Y. Shi, B. Jin, and C. Zhang, "Ultrafast Carrier Dynamics and Terahertz Conductivity of Photoexcited GaAs Under Electric Field," *Applied Physics Letters*, vol. 93, p. 102103, 2008.
- [176] B. G. Alberding, P. A. DeSario, C. R. So, A. D. Dunkelberger, D. R. Rolison, J. C. Owrutsky, *et al.*, "Static and Time-Resolved Terahertz Measurements of Photoconductivity in Solution-Deposited Ruthenium Dioxide Nanofilms," *Journal of Physical Chemistry C*, vol. 121, pp. 4037-4044, Feb 2017.
- [177] J. M. Gonzalez and I. I. Oleynik, "Layer-dependent properties of SnS₂ and SnSe₂ two-dimensional materials," *Physical Review B*, vol. 94, Sep 29 2016.
- [178] H. S. Song, S. L. Li, L. Gao, Y. Xu, K. Ueno, J. Tang, *et al.*, "High-performance top-gated monolayer SnS₂ field-effect transistors and their integrated logic circuits," *Nanoscale*, vol. 5, pp. 9666-9670, 2013.

- [179] J. Hu, B. L. Huang, C. X. Zhang, Z. L. Wang, Y. M. An, D. Zhou, *et al.*, "Engineering stepped edge surface structures of MoS₂ sheet stacks to accelerate the hydrogen evolution reaction," *Energy & Environmental Science*, vol. 10, pp. 593-603, Feb 1 2017.
- [180] R. G. Li, F. X. Zhang, D. G. Wang, J. X. Yang, M. R. Li, J. Zhu, *et al.*, "Spatial separation of photogenerated electrons and holes among {010} and {110} crystal facets of BiVO₄," *Nature Communications*, vol. 4, Feb 2013.
- [181] D. Voiry, M. Salehi, R. Silva, T. Fujita, M. W. Chen, T. Asefa, *et al.*, "Conducting MoS₂ Nanosheets as Catalysts for Hydrogen Evolution Reaction," *Nano Letters*, vol. 13, pp. 6222-6227, Dec 2013.
- [182] T. Homrarueng, Y. Sudswad, R. Sorod, N. Kayunkid, and W. Yindeesuk, "Study of Structural and Optical Properties of PbS Thin Films," *Third International Conference on Photonics Solutions (Icps2017)*, vol. 10714, 2018.
- [183] C. F. Ma, C. W. Shi, K. Lv, C. Ying, S. S. Fan, and Y. Yang, "Gradient-band-gap strategy for efficient solid-state PbS quantum-dot sensitized solar cells," *Nanoscale*, vol. 11, pp. 8402-8407, May 7 2019.
- [184] L. Hu, S. J. Huang, R. Patterson, and J. E. Halpert, "Enhanced mobility in PbS quantum dot films via PbSe quantum dot mixing for optoelectronic applications," *Journal of Materials Chemistry C*, vol. 7, pp. 4497-4502, Apr 21 2019.
- [185] G. H. Carey, A. L. Abdelhady, Z. J. Ning, S. M. Thon, O. M. Bakr, and E. H. Sargent, "Colloidal Quantum Dot Solar Cells," *Chemical Reviews*, vol. 115, pp. 12732-12763, Dec 9 2015.
- [186] M. H. Zarghami, Y. Liu, M. Gibbs, E. Gebremichael, C. Webster, and M. Law, "p-Type PbSe and PbS Quantum Dot Solids Prepared with Short-Chain Acids and Diacids," *Acs Nano*, vol. 4, pp. 2475-2485, Apr 2010.
- [187] G. Konstantatos, "Current status and technological prospect of photodetectors based on two-dimensional materials," *Nature Communications*, vol. 9, Dec 10 2018.
- [188] G. L. Ye, Y. J. Gong, S. D. Lei, Y. M. He, B. Li, X. Zhang, *et al.*, "Synthesis of large-scale atomic-layer SnS₂ through chemical vapor deposition," *Nano Research*, vol. 10, pp. 2386-2394, Jul 2017.
- [189] D. De, J. Manongdo, S. See, V. Zhang, A. Guloy, and H. B. Peng, "High on/off ratio field effect transistors based on exfoliated crystalline SnS₂ nano-membranes," *Nanotechnology*, vol. 24, Jan 18 2013.
- [190] G. Konstantatos, I. Howard, A. Fischer, S. Hoogland, J. Clifford, E. Klem, *et al.*, "Ultrasensitive solution-cast quantum dot photodetectors," *Nature*, vol. 442, pp. 180-183, Jul 13 2006.
- [191] V. Kochat, C. S. Tiwary, T. Biswas, G. Ramalingam, K. Hsieh, K. Chattopadhyay, *et al.*, "Magnitude and Origin of Electrical Noise at Individual Grain Boundaries in Graphene," *Nano Letters*, vol. 16, pp. 562-567, Jan 2016.
- [192] K. Hsieh, V. Kochat, X. Zhang, Y. J. Gong, C. S. Tiwary, P. M. Ajayan, *et al.*, "Effect of Carrier Localization on Electrical Transport and Noise at Individual Grain Boundaries in Monolayer MoS₂," *Nano Letters*, vol. 17, pp. 5452-5457, Sep 2017.
- [193] J. K. Kim, Y. Song, T. Y. Kim, K. Cho, J. Pak, B. Y. Choi, *et al.*, "Analysis of noise generation and electric conduction at grain boundaries in CVD-grown MoS₂ field effect transistors," *Nanotechnology*, vol. 28, Nov 24 2017.
- [194] H. Tian, C. Fan, G. Z. Liu, Y. H. Zhang, M. J. Wang, and E. P. Li, "Hydrothermal synthesis and fast photoresponsive characterization of SnS₂ hexagonal nanoflakes," *Journal of Materials Science*, vol. 54, pp. 2059-2065, Feb 2019.
- [195] C. Fan, Y. Li, F. Y. Lu, H. X. Deng, Z. M. Wei, and J. B. Li, "Wavelength dependent UV-Vis photodetectors from SnS₂ flakes," *Rsc Advances*, vol. 6, pp. 422-427, 2016.
- [196] D. Kufer and G. Konstantatos, "Highly Sensitive, Encapsulated MoS₂ Photodetector with Gate Controllable Gain and Speed," *Nano Letters*, vol. 15, pp. 7307-7313, Nov 2015.
- [197] P. Han, L. St Marie, Q. X. Wang, N. Quirk, A. El Fatimy, M. Ishigami, *et al.*, "Highly sensitive MoS₂ photodetectors with graphene contacts," *Nanotechnology*, vol. 29, May 18 2018.
- [198] S. A. McDonald, G. Konstantatos, S. G. Zhang, P. W. Cyr, E. J. D. Klem, L. Levina, *et al.*, "Solution-processed PbS quantum dot infrared photodetectors and photovoltaics," *Nature Materials*, vol. 4, pp. 138-142, Feb 2005.
- [199] N. C. Greenham, X. G. Peng, and A. P. Alivisatos, "Charge separation and transport in conjugated-polymer/semiconductor-nanocrystal composites studied by photoluminescence quenching and photoconductivity," *Physical Review B*, vol. 54, pp. 17628-17637, Dec 15 1996.
- [200] W. J. Zhang, J. K. Huang, C. H. Chen, Y. H. Chang, Y. J. Cheng, and L. J. Li, "High-Gain Phototransistors Based on a CVD MoS₂ Monolayer," *Advanced Materials*, vol. 25, pp. 3456-3461, Jul 5 2013.

- [201] Y. X. Han, X. Zheng, M. Q. Fu, D. Pan, X. Li, Y. Guo, *et al.*, "Negative photoconductivity of InAs nanowires," *Physical Chemistry Chemical Physics*, vol. 18, pp. 818-826, Jan 14 2016.
- [202] S. Song, W. K. Hong, S. S. Kwon, and T. Lee, "Passivation effects on ZnO nanowire field effect transistors under oxygen, ambient, and vacuum environments," *Applied Physics Letters*, vol. 92, Jun 30 2008.
- [203] C. Y. Chen, H. Qiao, S. H. Lin, C. M. Luk, Y. Liu, Z. Q. Xu, *et al.*, "Highly responsive MoS₂ photodetectors enhanced by graphene quantum dots," *Scientific Reports*, vol. 5, Jul 3 2015.
- [204] Z. Y. Yin, H. Li, H. Li, L. Jiang, Y. M. Shi, Y. H. Sun, *et al.*, "Single-Layer MoS₂ Phototransistors," *Acs Nano*, vol. 6, pp. 74-80, Jan 2012.
- [205] F. Ghasemi and S. Mohajerzadeh, "Sequential Solvent Exchange Method for Controlled Exfoliation of MoS₂ Suitable for Phototransistor Fabrication," *Acs Applied Materials & Interfaces*, vol. 8, pp. 31179-31191, Nov 16 2016.
- [206] Y. N. Hou, Z. X. Mei, and X. L. Du, "Semiconductor ultraviolet photodetectors based on ZnO and Mg_xZn_{1-x}O," *Journal of Physics D-Applied Physics*, vol. 47, Jul 16 2014.
- [207] K. Lee, J. M. Choi, D. K. Hwang, M. S. Oh, J. K. Kim, Y. Jung, *et al.*, "Top-gate ZnO thin-film transistors with a polymer dielectric designed for ultraviolet optical gating," *Sensors and Actuators a-Physical*, vol. 144, pp. 69-73, May 28 2008.
- [208] K. Thakar, B. Mukherjee, S. Grover, N. Kaushik, M. Deshmukh, and S. Lodha, "Multilayer ReS₂ Photodetectors with Gate Tunability for High Responsivity and High-Speed Applications," *Acs Applied Materials & Interfaces*, vol. 10, pp. 36512-36522, Oct 24 2018.
- [209] A. Rogalski, "Graphene-based materials in the infrared and terahertz detector families: a tutorial," *Advances in Optics and Photonics*, vol. 11, pp. 314-379, Jun 30 2019.
- [210] J. O. Island, S. I. Blanter, M. Buscema, H. S. J. van der Zant, and A. Castellanos-Gomez, "Gate Controlled Photocurrent Generation Mechanisms in High-Gain In₂Se₃ Phototransistors," *Nano Letters*, vol. 15, pp. 7853-7858, Dec 2015.
- [211] Y. T. Chen, I. Sarangadharan, R. Sukesan, C. Y. Hseih, G. Y. Lee, J. I. Chyi, *et al.*, "High-field modulated ion-selective field-effect-transistor (FET) sensors with sensitivity higher than the ideal Nernst sensitivity," *Sci Rep*, vol. 8, p. 8300, May 29 2018.
- [212] G. B. Liu, Z. H. Li, X. S. Chen, W. Zheng, W. Feng, M. J. Dai, *et al.*, "Non-planar vertical photodetectors based on free standing two-dimensional SnS₂ nanosheets," *Nanoscale*, vol. 9, pp. 9167-9174, Jul 14 2017.
- [213] G. X. Su, D. De, V. G. Hadjiev, and H. B. Peng, "Novel layered two-dimensional semiconductors as the building blocks for nano-electronic/photonic systems," *Micro- and Nanotechnology Sensors, Systems, and Applications Vi*, vol. 9083, 2014.
- [214] P. R. Brown, D. Kim, R. R. Lunt, N. Zhao, M. G. Bawendi, J. C. Grossman, *et al.*, "Energy Level Modification in Lead Sulfide Quantum Dot Thin Films through Ligand Exchange," *Acs Nano*, vol. 8, pp. 5863-5872, Jun 2014.